UNIVERSITY OF CALIFORNIA
RIVERSIDE

Pre-Lithiation of Silicon Anode via Oxygen and Sulfur Chemistry

A Dissertation submitted in partial satisfaction
of the requirements for the degree of

Doctor of Philosophy

in

Chemical and Environmental Engineering

by

Jiayan Shi

June 2022

Dissertation Committee:
Dr. Juchen Guo, Chairperson
Dr. Kandis Leslie Abdul-Aziz
Dr. Jinyong Liu
Dr. Chi-Cheung Su

The Dissertation of Jiayan Shi is approved:

_____

_____

_____

_____

Committee Chairperson

University of California, Riverside

ACKNOWLEDGEMENTS

Throughout my journey of study, I have received so much help from my family members, friends, teachers, and professors. I truly appreciate all the help and support. I know from deep in my heart that so many of them I have no way to pay back.

But the person I want to thank most is myself. This long learning trip has given me such a good lesson that, although so many people are able to and willing to offer help, all decisions, steps, and progress must be made by myself. Now I recognize my courage so much. I finally realize it is myself, not somebody else, who always leads me. I want to thank all people and things no matter if they had ever encouraged or discouraged me. I wish I always would remember the feeling of this moment and always keep this courage in my future life. To be strong and independent. To live on myself and live for myself.

ABSTRACT OF THE DISSERTATION

Pre-Lithiation of Silicon Anode via Oxygen and Sulfur Chemistry

by

Jiayan Shi

Doctor of Philosophy, Chemical and Environmental Engineering
University of California, Riverside, June 2022
Dr. Juchen Guo, Chairperson

Owing to its exceptionally high specific capacity, silicon anode is a promising up-and-coming candidate for the next generation of energy high-energy-density lithium-ion batteries (LIBs). One of the significant problems of silicon anode is its large first-cycle irreversibility, leading to a substantial loss of recyclable lithium originating from the metal oxide cathode materials in a full cell. Pre-lithiation is considered a highly appealing technique to compensate the active lithium losses and increase practical energy density. Various pre-lithiation techniques have been evaluated so far, including both cathode pre-lithiation and anode pre-lithiation. In most cases, pre-lithiation compensates for the 1st cycle of active lithium loss, attributed mainly to SEI formation. This technology increases the remaining amount of active/cyclable lithium inside the cell during continuous charge/discharge cycling. It also increases reversible capacity and energy density. This thesis will go over studies about the realization of lithium oxide, lithium peroxide (Li_2O/Li_2O_2), and pre-lithiatied sulfur (such as Li_2S) as low-cost and low-weight lithium sources. At the same time, issues and solutions for using those pre-lithiating reagents as

lithium sources were discussed. At the same time, other emerging battery technologies beyond Li-ion were discovered including lithium metal and multivalent-ion batteries.

TABLE OF CONTENTS

LIST OF FIGURES

LIST OF TABLES

Chapter 1: Introduction

1.1 Overview of Li-ion Battery Technologies

Lithium-ion (Li-ion) batteries have become the most predominant energy storage technology owing to their high capacity, low cost, and long cycle life. Due to their contribution to powering the world and shading light on the path to a carbon-neutral society, in 2019, three scientists, John B Goodenough, M Stanley Whittingham, and Akira Yoshino, were awarded the Nobel Prize in Chemistry. However, current Li-ion battery technologies cannot meet the increasingly more versatile requirements. Researchers are keeping looking for new combinations of cell components and battery chemistry for the next-generation battery technology.

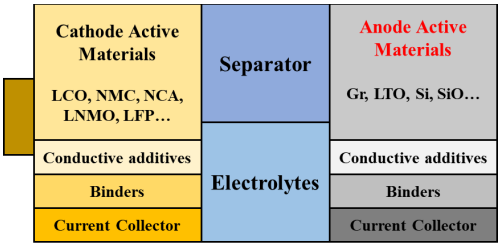

Figure 1. Main components in a Li-ion battery.

Current Li-ion batteries share similar cell components, including cathode (positive electrode), anode (negative electrode), electrolyte, and inert supporting materials. It is good to have a general understanding of each cell component and interface in a Li-ion battery. **Figure 1** shows the main components of a Li-ion battery.

1.1.1 Cathode Materials

Currently, there are mainly two types of cathode materials based on cathode reaction mechanisms: the intercalation type and the conversion type. For the intercalation type,

$LiCoO_2$ was the firstly used cathode material in commercialized Li-ion batteries and is still widely used. However, considering the safety and total inventory of cobalt in the world, the market has reduced the manufacturing of Li-ion batteries consisting of $LiCoO_2$ as cathode material. Lithium iron phosphate ($LiFePO_4$) has very good thermal stability and low cost. Therefore, the $LiFePO_4$ cathode is suitable for electric vehicles (EVs). The lithium nickel manganese cobalt oxide (NMC) could be the most promising cathode material for Li-ion batteries for EV application considering tthe good cycle life, safety, and high capacity. Although lithium manganese oxide could offer higher voltage and good thermal stability, the limited cycle life and high initial activation voltage limits its application. On the other hand, market still exists for conversion-type cathode materials such as chalcogens including sulfur. Sulfur is considered as a typical conversion-type material. Even though positive results have been reported in a few reports, how to complete sulfur and other conversion type chemistry into real application is still hard to answer.

1.1.2 Anode Materials

As for the anode materials for Li-ion batteries, graphite and silicon is the mostly used anode materials. Lithium titanate (LTO) anode materials have much better safety, due to its thermal stability and low temperature operation. The Li-ion batteries made by LTO anode offer ultra-long cycle life. However, the much lower energy density limits its application in Li-ion batteries because of the low cell voltage.

1.2 Capacity Fade of Li-ion Batteries[3]

Capacity fade is always observed in a lithium-ion battery during cycling. This capacity loss or fade occurs due to side reactions that occur in these batteries. The current understanding

of the mechanisms of capacity fade in lithium-ion batteries is shown in **Figure 2**. Processes that lead to capacity fade in lithium-ion cells are summarized which include lithium deposition (overcharge conditions), electrolyte decomposition, active material dissolution, phase changes in the insertion electrode materials, and passive film formation over the electrode and current collector surfaces. Understanding the mechanisms behind the capacity fading phenomenon is essential for battery modeling and for further improvement of current battery technology.

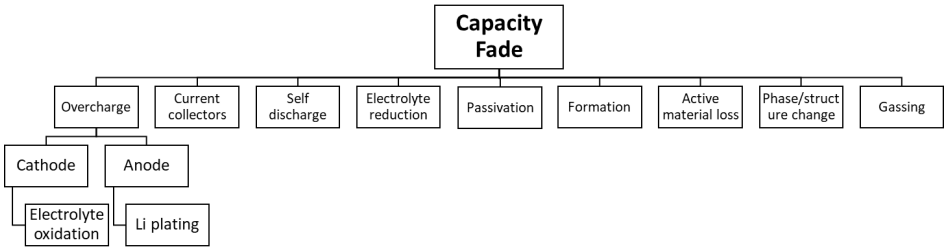

Figure 2. Current understanding of capacity fade mechanism of Li-ion batteries.

Capacity Balancing in lithium-ion cells is essential. A cell without a well-balanced electrode mass will lead to capacity fade, and the impact can be accumulative over cycles. Many situations change the balance of a cell, especially when new combinations of anode-cathode-electrolytes keep emerging. Any change in a battery system requires reconsideration of capacity balancing, which is usually neglected in the literature, and it is actually very important for any real-world battery studies focusing on capacity fade mechanisms.

Formation Cycles consume Li^+ but form a passivation layer on both electrodes. Pre-lithiation may need for compensating the Li^+ loss, especially for some high-energy-density anode materials. Though not mentioned in the review, Si and SiO are widely used in

commercial Li-ion batteries today. They require a better understanding of the mechanisms behind the formation cycles and pre-lithiation process. Degas may be needed because of the by-products of forming the passivation layer during formation. However, not all cell formats are capable of doing degassing. Therefore, a deeper understanding of gassing mechanisms and careful selection of cell components are necessary when doing related fundamental studies.

Overcharge Phenomena can be classified into three main types at present: (i) overcharge of negative electrodes, (ii) overcharge of positive electrodes, and (iii) overcharge/high-voltage electrolyte oxidation processes. For the overcharge of carbon-based anode materials, Li plating is a common issue. The formation of lithium metal is also a safety hazard due to its extreme reactivity toward liquid solvents. Lithium metal deposition may be more of a concern with graphite anode due to the low working potential vs. Li metal. The Si-related anode is not mentioned in the review. But overlithiation of Si-type material is also needed to be avoided due to its huge volume change. It is believed that material vendors will provide a safe utilization window for their new materials based on their own design mechanisms (working potential, mechanical integrity, etc.). Therefore, it is also important to understand the working and fading mechanisms of Si anode materials.

For of high-voltage positive electrodes, overcharging the positive electrodes in lithium-ion cells can lead to a wide variety of electrochemical side reactions. One of the biggest issues coming with overcharging cathode material is oxygen redox, which is also known as anion redox. The loss of oxygen from the sample during cycling is undesirable, not only because it could induce structural damage to the sample surface impacting the cycling ability, but

also because it tends to oxidize the electrolyte which also reduces the cell's life. It is surprising that nowadays research is still ongoing to understand the activity of oxygen in cathode materials. This becomes even more important for new high-voltage cathode materials with new compositions, coating, and doping. It could also be related to the surface activity of cathode materials charged to high voltage and their interaction with other cell components which requires further fundamental study.

Overcharge/High Voltage Electrolyte Oxidation Processes: High voltage positive electrodes used in lithium-ion batteries present a stringent requirement for electrolyte stability and purity. Nowadays EC is widely used compared to PC. People believe EC can be easily oxidized at a voltage around 4.0 V which requires improvements in understanding and designing electrolyte systems for the high-voltage cathode. Also, solvent oxidation products such as gases or other species will build up in the cell and cause a variety of problems. The rate of solvent oxidation depends on the surface area of the positive electrode material, current collectors, and the carbon black additive. In fact, the choice of carbon black and its surface area are critical variables because solvent oxidation may occur more on the carbon black than on the metal oxide electrode due to the higher surface area of the former. Actually, people have used isotope-labeled ^{13}C to do the MS test and realized that conductive carbon is not stable enough at high voltage. Therefore, similar research should be done to help people further understand the stability of not only cell components such as electrodes and electrolytes, but also other “inert” cell components.

Overcharge Protection can be realized by technologies such as chemical shuttles, separators with melting points of about 140°C, and additives such as Li_2CO_3, and biphenyl.

Nowadays, how safe these methods are is difficult to conclude. Systematic fundamental studies at the muti-cell level are difficult to conduct in academia. BMS is currently widely used to prevent overcharge. But mathematic models and a deeper understanding of the electrochemical process are necessary for the precise functioning of BMS.

Electrolyte Decomposition (Reduction) Processes: Electrolyte reduction can jeopardize the capacity and cycle life of the cell by consuming salt and solvent species and compromises the safety of the system by generating gaseous products which increase the internal pressure of the cell. There are two reaction pathways, which are the "one-electron transfer process" and "two-electron transfer process". A few people keep working in this direction nowadays, though new materials keep coming out and they may undergo different electrochemical processes. I believe the multi-electron transfer process that combines electrochemical and chemical reduction processes is more reliable based on some of my eQCM experiments. But electrode materials differ from each other which also needs further fundamental study.

Minimizing the electrolyte reduction reactions and the capacity losses is beneficial for enhancing cycle life and improving the high-temperature performance of lithium-ion batteries. This requires the further design of new electrolyte systems, such as electrolytes with special solvation structures that involves salt reduction.

However, It is not considered to be true that the electrolyte reduction reactions on carbon surfaces are similar to those on lithium metal because the difference in potential between the metallic lithium and fully lithiated carbon is very small. Different anode-electrolyte

interphase models co-exist, which requires further fundamental study. Their composition could be very similar, but the structure and formation process could be very different.

Self-discharge Processes: The extent of this self-discharge depends on factors such as cathode and cell preparation, nature and purity of the electrolyte, temperature, and time of storage. Though Li-ion batteries are supposed to have low self-discharge rate, it does change with temperature (breaking passivation surface) and potential side reactions (generating shutting reagents). Both require further fundamental studies in real cases. Better characterization method should be came up with in order to decrease the time for self-discharge measurement. Another reversible contribution to self-discharge in lithium-ion cells can be attributed to the leakage currents through the separator of the cell. Manufacturing defects are not always the primary. But when Li plating happens, it is.

Interfacial Film Formation: A passive film is formed at the negative electrode/electrolyte interface because of irreversible side reactions that occur between the solvent and electrode surface. The actual morphology of the SEI is very complex and changes with time and with electrolyte composition. The SEI model assumes that the passive layer formed over the surface prevents further reaction but still allows lithium ions to pass through. The rate-determining step for the deposition-dissolution process is often the migration of lithium cations through the passivating layer covering the lithium surface. It may not be true for all electrode materials or for all electrolyte compositions.

Polymer electrolyte interphase (PET) model to describe the behavior of the lithium metal electrode covered by a porous non-conducting polymeric film. The charge-transfer reaction is limited by the surface coverage of the lithium electrode by the PET and with the diffusion

of electrolyte through the porous structure of the interface. PET model is less mentioned nowadays. People still refer to the SEI model for the metal anode, but the corrosion process is taken into consideration for the metal anode. These should be further considered and studied if lithium and other metal anode will be used.

Current Collectors: issues related to current collectors are passive film formation, adhesion, and localized corrosion such as pitting, generally known as Al and Cu corrosion. It is unfortunate that academia still hasn't answered or fully addressed the issue of current collectors, though these problems are essential for high-temperature battery applications. I believe the corrosion process of the current collector is a dynamic process, which is reaction kinetics related. Some parameters such as electrolyte viscosity may influence the current collector corrosion. There are still relatively few studies of corrosion processes in lithium-ion cells, especially with new salts and electrolyte compositions that keep coming out.

Positive Electrode Dissolution: Positive electrode dissolution phenomena are both electrode and electrolyte specific. Now, increasingly more research start focusing on the positive electrode dissolution process. Generally, people believe high-voltage or acid-induced decomposition will lead to transition metal dissolution, including Ni, Co, and Mn. However, I believe it should not only be materials-related but also interface and electrolyte-related. These require a further understanding of the structure-activity relationship and solvating power of the electrolyte system.

Phase Changes in Insertion Electrodes: The understanding of the relationship between phase changes in insertion electrodes and capacity loss is weak even though this is widely

quoted as a mechanism of capacity loss. The basic mechanism stated is that phase changes or large changes in lattice parameters lead to fracture of particles and loss of contact from the electrode matrix. With the help of high-energy X-ray techniques, nowadays, scientists can *in-situ* study the normal operation, overcharge, and overdischarge of batteries for both cathode, anode, and other new materials. However, it must be mentioned here that, the failure of batteries is very complex. It is very necessary to do a systematic comparison among all properties of materials to avoid a rush conclusion by only looking at the phase change of materials. At the same time, new electrochemical models for these phase change materials should be developed. It is because, originally, the phase change was not considered in the classic model of materials.

Incorporation of capacity Fade Mechanisms into Battery Modeling: Advances in modeling lithium-ion cells must result from improvements in the fundamental understanding of these processes and the collection of relevant experimental data. Developing mathematical models containing these capacity fade processes not only provides a tool for battery design but also provides a means of understanding better how those processes occur. Quantifying the contribution of each capacity fade mechanism is important for battery modeling. Currently, models that combine kinetics and transport processes in batteries are still under development to predict cell performance during normal cycling and under abuse conditions. It could be ideal to develop suitable models for each capacity fade mechanism. But it is important for battery design, selection, and new product development.

1.3 Chemistry of Batteries Beyond Li-ion

Nowadays, energy storage technologies based on charging-discharging mechanisms are of great importance as tools for reducing environmental pollution problems and the use of fossil fuels. Lithium-ion batteries are charge-discharge devices that have been widely marketed and used in portable electronics and automotive applications since 1991, thanks to their operational reliability, high energy density, energy efficiency, long life (up to 1000 cycles), light weight, and ability to be charged in a short time (15 min).[4,5] Also, LIBs span a wide range of power/energy ratios and achieve a discharge voltage of 3.6 to 3.7 V.[6] Despite all the above-mentioned advantages, LIBs are relatively expensive because of the high cost of lithium and its expected scarcity in the coming decades.[7]

Due to the request for higher energy densiy of batteries for different applications, emerging new chemistries are involved in or trying to replace current lithium-ion battery technology. Lithium metal battery is one of them. The most apparent difference is the anode active material, as compared to a Li metal battery in **Figure 3**. Lithium will ignite and burn in oxygen when exposed to water or water vapor. More importantly, the melting point of lithium metal is as low as 180.50 °C. Molten lithium is significantly more reactive than its solid form. Most importantly, the packaging of the battery and even the pack can be easily destroyed by molten lithium. Due to the reactivity of lithium metal, the exothermal reaction is more intense. Therefore, the safe operation of lithium metal batteries is more difficult than a lithium-ion battery.

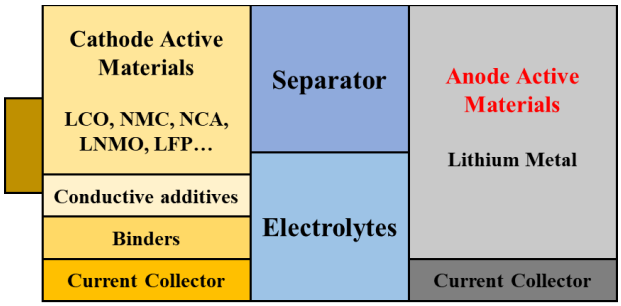

Figure 3. Main components in a Li metal battery.

It is worth mentioning here that though Li metal is not contained in the normal operation of Li-ion batteries, Li platting may happen under many conditions, such as low temperature or poor cathode/anode capacity matching. Therefore, strategies need to be embedded into batteries to enable the safe operation of current commercial batteries. Although Li metal batteries have been regarded as the most promising next-generation Li batteries, there are a lot of improvements need to be done (e.g. safety and cycle life) before its commercialization. Electrolyte formulation optimization is the most important direction for stabilize the electrolyte/electrodes interphases. One practice of designing new electrolytes for reactive lithium metal batteries is introduced in this thesis.

Apart from the single-electron transfer chemistry of lithium, multi-electron transfer chemistries are also considered for high-energy battery technologies. Sulfur is considered a conversion-type cathode material in the electrochemistry field based on simple redox reactions of sulfur. Sulfur has a high theoretical capacity around 1675 mAh g^{-1} which makes it a very attractive material to study. Sulfur-based cathode materials have been extensively investigated for Li-ion batteries.[8-10] Oxygen shares very similar reactions as sulfur because it sits in the same family of the periodic table. However, instead of the solid-

liquid-solid transfer process of sulfur chemistry, oxygen chemistry goes through an even more reactive pathway involving gas evolution. Gas evolution is a huge issue for most battery technologies as already mentioned. A practice of minimizing gas impact will also be introduced in the thesis.

Rechargeable multivalent metal anode batteries including magnesium (Mg) and aluminum (Al) are regarded as one of the candidates for next-generation energy storage technologies due to their abundance and high volumetric capacity. However, these battery technologies still lack state-of-the-art electrolytes for practical application. Further investigations will be performed to provide rigorous guidance on the design of electrodes and electrolytes for rechargeable multivalent batteries.

References

1 Ding, Yu, Pei Pan, Lihui Chen, Zhengbing Fu, Jun Du, Liangui Guo, and Feng Wang. LiFePO4 composites decorated with nitrogen-doped carbon as superior cathode materials for lithium-ion batteries. Ionics 23.12 (2017): 3295-3302.

2 Garche J, Brandt K, In: Li-Battery Safety. Elsevier; 2018 Chapter 3.3

3 Arora, Pankaj, Ralph E. White, and Marc Doyle. "Capacity fade mechanisms and side reactions in lithium-ion batteries." Journal of the Electrochemical Society 145, no. 10 (1998): 3647.

4 Andre, D., Kim, S.-J., Lamp, P., Lux, S. F., Maglia, F., Paschos, O., and Stiaszny, B. Future generations of cathode materials: an automotive industry perspective. Journal of Materials Chemistry A, 2015, 3, 13, 6709–6732.

5 Schmuch, R., Wagner, R., Hörpel, G., Placke, T., and Winter, M. Performance and cost of materials for lithium-based rechargeable automotive batteries. Nature Energy, 2018, 3, 4, 267–278.

6 Yang, Q., Zhang, Z., Sun, X.-G., Hu, Y.-S., Xing, H., and Dai, S. Ionic liquids and derived materials for lithium and sodium batteries. Chemical Society Reviews, 2018, 47, 6, 2020–2064.

7 Sawicki, M., and Shaw, L. L. Advances and challenges of sodium ion batteries as post lithium ion batteries. RSC Advances, 2015, 5, 65, 53129–53154.

8 Fang, R.; Zhao, S.; Sun, Z.; Sun, Z.; Wang, D.; Cheng, H.; Li, F. More Reliable Lithium-Sulfur Batteries: Status, Solutions and Prospects. *Adv. Mater.* **2017**, 29, 1606823. DOI: 10.1002/adma.201606823.

9 Peng, H.; Huang, J.; Cheng, X.; Zhang, Q. Review on High-Loading and High-Energy Lithium-Sulfur Batteries. *Adv. Energy Mater.* **2017**, 7, 1700260. DOI: 10.1002/aenm.201700260.

10 Wild, M.; O'Neill, L.; Zhang, T.; Purkayastha, R.; Minton, G.; Marinescu, M.; Offer, G. J. Lithium Sulfur Batteries, *A Mechanistic Review. Energy Environ. Sci.* **2015**, 8, 3477.

Chapter 2: Pre-lithiated Sulfur Batteries

2.1 Advantages and Disadvantages of Batteries Based on Sulfur Chemistry

Lithium-sulfur (Li-S) batteries are regarded as one of the most promising electrochemical energy storage technologies due to their low cost, environmental benignity, and outstanding theoretical capacity[1,2]. However, despite tremendous research and development efforts, there are still a number of challenges hindering their commercialization. Among these key challenges are the polysulfides shuttle effect and high electrolyte/sulfur ratio, which are significantly reinforced by the instability of the Li metal anode. [3-6] Therefore, high-capacity non-Li anodes, particularly those comprised of silicon-based materials, have been proposed as replacements for Li metal in Li-S batteries. [7] The use of silicon anode materials would require a pre-lithiated sulfur cathode, i.e. lithium sulfide (Li_2S). In recent years, various methods of Li_2S-carbon composite material synthesis have been reported, including mixing of Li_2S with carbon,[8] chemical lithiation of S-C composites, [9, 10] Li_2S-C composites synthesis via dissolving and precipitating Li_2S in ethanol,[11-15] embedding Li_2S in carbon matrix via Li-nitrogen interaction, [16] Li_2S-C composites synthesis via thermal reaction between Li metal with carbon disulfide,[17] and thermal reduction of Li_2SO_4 by carbon. [18-22]

2.2 Li_2CO_3, Li_2NO_3, CH_3COOLi as Precursor

We demonstrate a new synthetic technique to produce lithium sulfide-carbon composite (Li_2S-C) cathodes for lithium-sulfur batteries via aerosol spray pyrolysis (ASP) followed by sulfurization. Specifically, lithium carbonate-carbon (Li_2CO_3-C) composite nanoparticles are first synthesized via ASP from aqueous solutions of sucrose and lithium

salts including nitrate ($LiNO_3$), acetate (CH_3COOLi) and Li_2CO_3, respectively. The obtained Li_2CO_3-C composites are consequentially converted to Li_2S-C through sulfurization via reaction with H_2S. Electrochemical characterizations show excellent overall capacity and cycle stability of the Li_2S-C composites with relatively high areal loading of Li_2S and low electrolyte/Li_2S ratio. The Li_2S-C nanocomposites also demonstrate clear structure-property relationships.

Materials Synthesis: Three lithium salts including lithium nitrate ($LiNO_3$), lithium acetate (CH_3COOLi) and lithium carbonate (Li_2CO_3) were used as the precursors for Li_2S with sucrose as the precursor for carbon. Each Li salt was dissolved in deionized water with sucrose at different concentrations as listed in **Table 1**. The obtained solutions were used in the ASP process.

Table 1. Precursor combinations and concentrations.

Sample Denotation	Lithium Salt & Conc.	Sucrose Conc.
NitS	0.3 M $LiNO_3$	0.2 M
AceS	0.3 M CH_3COOLi	0.02 M
CarS	0.1 M Li_2CO_3	0.085 M

The ASP system in this study is illustrated in **Figure 4**. the commercial aerosol generator (TSI, Model 3076) consisting of a nebulizer and a solution reservoir is attached to a diffusion dryer followed by a tubular furnace and a filter collector. The diffusion dryer was composed by two concentric tubes: The outer tube is made of 3-inch inner diameter PVC tubing and the inner tube is made of 0.5-inch diameter steel mesh with the annual space filled with porous silica gel. The aerosol of the precursor solution was generated by the

nebulizer and carried through the diffusion dryer by argon gas to desiccate the water content. The resultant dry particles were continuously carried into the tube furnace heated at 850°C to produce the Li_2CO_3-C nanoparticles, which are collected with a stainless steel filter downstream outside the tube furnace.

The synthesized Li_2CO_3-C composite is placed in an alumina boat in a tubular furnace, followed by purging with argon for an hour. The furnace was then heated to 725°C and maintained at this temperature for 5 hours under a flow of 5 vol.% H_2S and 95 vol.% argon. After 5 hours the flow gas was switched to pure argon and the furnace was cooled naturally to room temperature. The product was collected in an argon-filled glovebox due to the sensitivity to moisture of Li_2S.

Materials Characterization: The nitrogen adsorption-desorption isotherms of the produced composite materials were obtained with a surface area and porosity analyzer (Micromeritics ASAP2020). The surface area was obtained with the Brunauer-Emmett-Teller (BET) method. The crystalline species in the composites were characterized by powder X-Ray diffraction (XRD, PANalytical). The morphology and microstructure of the composites were characterized by scanning electron microscopy (SEM) and transmission electron microscopy (TEM, Tecnai T12). Carbon content in the Li_2CO_3-C composites was measured via thermogravimetric analysis (TGA, TA Instruments). The TGA samples were held at 120°C for 30 minutes to remove the moisture absorbed from environment, followed by heating to 600°C at a rate of 10°C min^{-1} with an isothermal step in dry air. The carbon contents in Li_2CO_3-C_{NitS}, Li_2CO_3-C_{AceS} and Li_2CO_3-C_{CarS} (**Figure 5)** are very consistent at 20.7 wt.%, 22.8 wt.% and 21.2 wt.%, respectively.

Electrode Preparation, Cell Assembly and Testing: The electrode is composed of 80 wt.% of Li_2S-C composite, 10 wt.% of carbon black additive, and 10 wt.% of polystyrene as the binder. Polystyrene was selected as the binder to avid the use of polar solvents (both protic and aprotic), most of which dissolve Li_2S to some extent, for typical binders. Instead, mesitylene (Sigma Aldrich) was used as the solvent for polystyrene in the electrode slurry. The electrodes were coated on carbon-coated aluminum current collector (MTI Corporation) in the argon-filled glovebox, with the average loading of Li_2S-C composite at 2 mg cm^{-2}. The electrodes were dried overnight in argon glovebox at room temperature, followed by drying at 120°C for four hours in vacuum. The dried electrodes are assembled into 2032-type coin cells with lithium foil anode (99.9%, Alfa Aesar) and Celgard® 2500 separator. The electrolyte used in this study is 1M lithium bis(trifluoromethanesulfonyl)imide (LiTFSI) solution in mixture of 1,3-dioxolane (DOL), dimethoxyethane (DME) and 1-butyl-1-methylpyrrolidinium bis(trifluoromethanesulfonyl)imide (Pyr14TFSI) (1:1:2 by vol.) with 1.5 wt.% of $LiNO_3$. The electrolyte to Li_2S-C ratio (μL/mg) was kept at 7 in all coin cells testing. The first cycle is run at a rate of 50 mA/g (with respect to Li_2S-C) to a charge cutoff of 3.5 V and discharge cutoff of 1.8 V. Subsequent cycles are run at 100 mA/g between 2.6 V and 1.8 V.

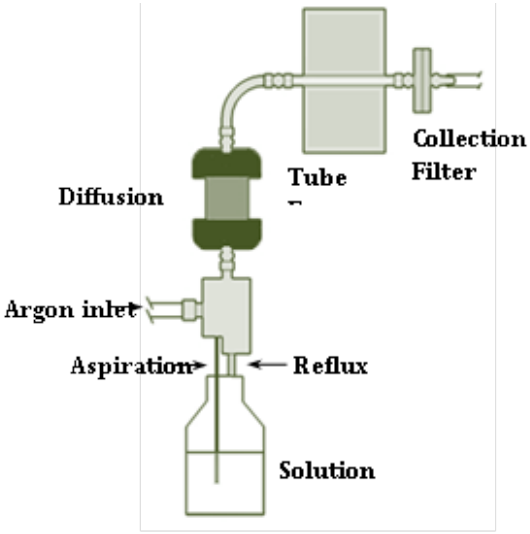

Figure 4. Schematic illustration of the aerosol spray pyrolysis system in this study.

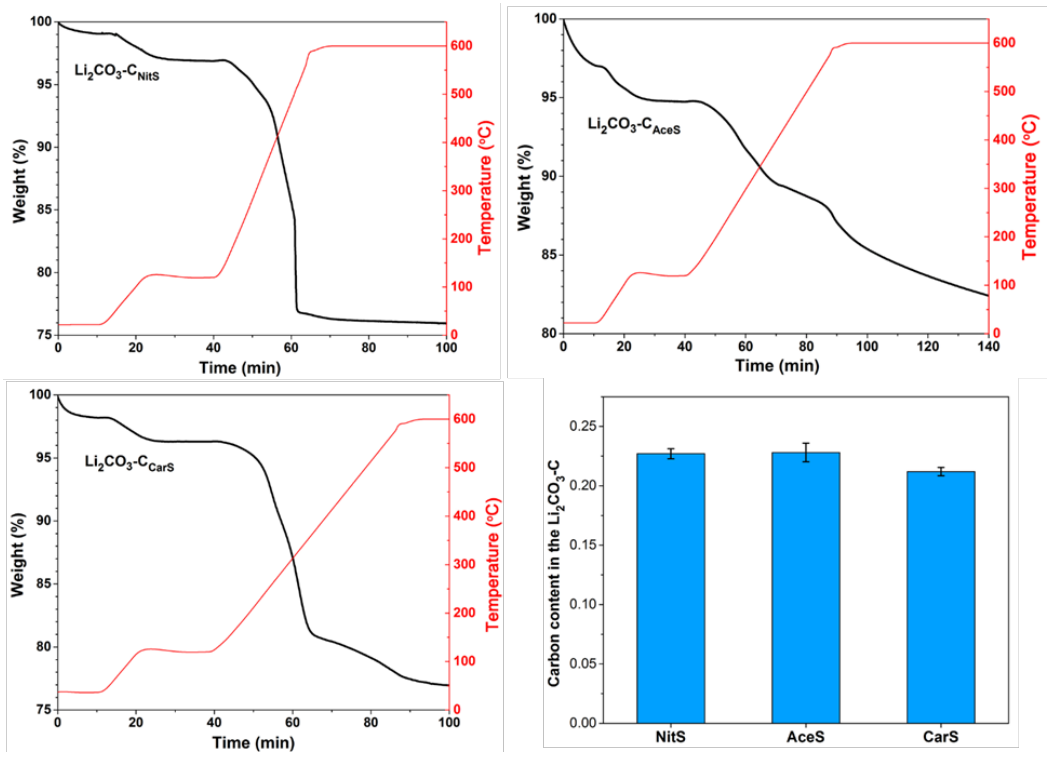

Figure 5. TGA of the Li2CO3-C nanocomposites.

In this work, we report a new scalable method for synthesizing Li_2S-C composites via

aerosol spray pyrolysis (ASP) followed by sulfurization (experimental details in the supplementary material). During ASP synthesis, three aqueous solutions containing sucrose (as carbon precursor) and either lithium nitrate ($LiNO_3$), lithium acetate (CH_3COOLi), or lithium carbonate (Li_2CO_3), denoted as NitS, AceS, and CarS, respectively, were atomized into aerosols with a pressure-enabled atomizer. The aerosols were sequentially carried by argon gas through a diffusion dryer and a tubular furnace for pyrolysis within an inert environment. The powder X-ray diffraction (XRD) patterns in **Figure 6a** clearly indicate that the obtained composites from all three lithium salts are Li_2CO_3-C composite with comparable carbon content (20.7 wt.% in Li_2CO_3-C_{NitS}, 22.8 wt.% in Li_2CO_3-C_{AceS} and 21.2 wt.% in Li_2CO_3-C_{CarS} via thermalgravimetric analysis). It is worth noting that sucrose solution without the lithium salts (i.e. precursors of Li_2CO_3) completely decomposes during the same ASP without any carbon formation. This observation reveals that Li_2CO_3 serves as the nucleation sites for carbonization of sucrose in ASP.[23] However, the formation mechanisms of Li_2CO_3 from these three Li salts are clearly different. For $LiNO_3$, its thermal decomposition is known to proceed according to **Reaction 1**:[24]

$$2LiNO_3 \rightarrow Li_2O + 2NO_x + (2.5 - x)O_2 \qquad (1)$$

Based on the XRD evidence of Li_2CO_3 with an absence of crystalline Li_2O, it can be speculated that carbon dioxide (CO_2) released from pyrolysis of sucrose further reacts with Li_2O to generate Li_2CO_3 according to **Reaction 2**:

$$Li_2O + CO_2 \rightarrow Li_2CO_3 \qquad (2)$$

CH_3COOLiundergoes thermal decomposition to generate Li_2CO_3 and acetone according to

Reaction 3:[25]

$$2CH_3COOLi \rightarrow Li_2CO_3 + C_3H_6O \qquad (3)$$

For the CarS precursor, Li_2CO_3 undergoes precipitation during ASP without decomposition, thus becoming directly embedded into the carbon matrix formed by the carbonization of sucrose.

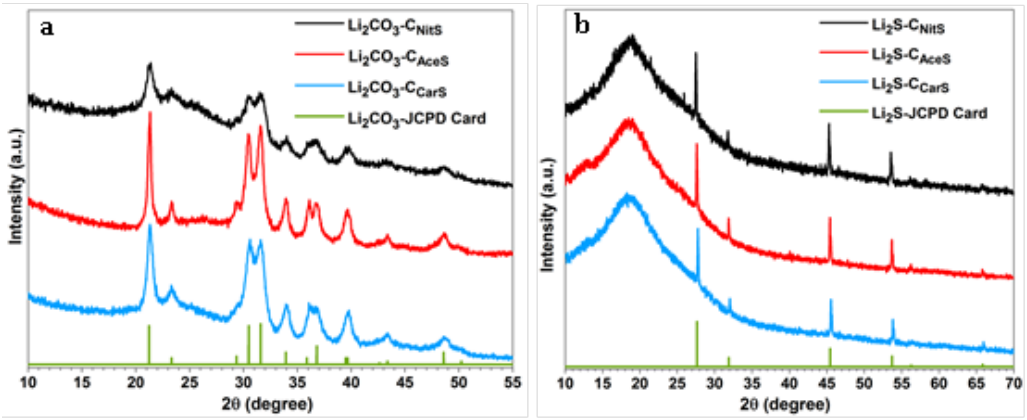

Figure 6. XRD patterns of (a) the Li2CO3-C composites obtained from ASP and (b) the Li2S-C composites after sulfurization.

Although the obtained Li_2CO_3-C composites have consistent composition and carbon content, they have distinctively different microstructures as displayed by the transmission electron microscopy (TEM) images in **Figures 7a-c**. The Li_2CO_3-C_{NitS} nanoparticles have a hollow-shell structure with irregular-shaped interior voids due to the release of NO_x and O_2 gases during pyrolysis. The high solubility of $LiNO_3$ in water also contributes to the formation of this hollow structure. When water evaporates during ASP, $LiNO_3$ precipitates at the outer surface of the aerosol droplets following the surface precipitation mechanism.[26] The microstructure of the Li_2CO_3-C_{NitS} nanoparticles is further revealed by the TEM image in **Figure 7d**, after the removal of Li_2CO_3 using diluted hydrochloric acid (HCl).

The carbon matrix of Li_2CO_3-C_{NitS} has a highly porous structure after Li_2CO_3 removal, indicating that Li_2CO_3 occupies the majority of the volume in the Li_2CO_3-C_{NitS} nanoparticles. The specific surface area of Li_2CO_3-C_{NitS} before and after Li_2CO_3 removal obtained from the nitrogen adsorption-desorption isotherms, displayed in **Figure 8**, is consistent with this observation: the specific surface area of Li_2CO_3-$C_{Nit\text{-}S}$ is significantly increased from 26.8 m^2 g^{-1} to 608.2 m^2 g^{-1} after Li_2CO_3 removal.

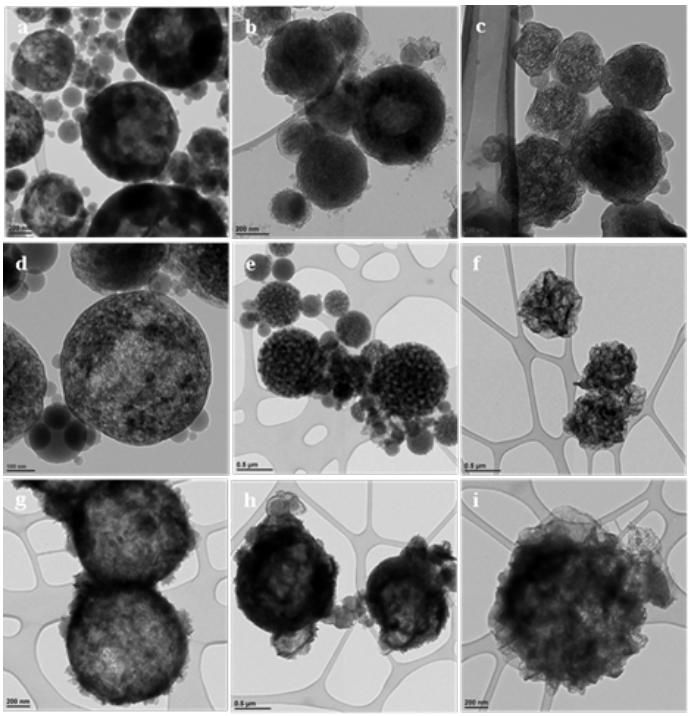

Figure 7. TEM images of (a) Li2CO3-CNitS, (b) Li2CO3-CAceS, (c) Li2CO3-CCarS; TEM images the carbon matrix of (d) Li2CO3-CNitS, (e) Li2CO3-CAceS, (f) Li2CO3-CCarS after Li2CO3 removed; and TEM images of (g) Li2S-CNitS, (h) Li2S-CAceS, (i) Li2S-CCarS.

On the other hand, Li_2CO_3-C_{AceS} nanoparticles show a denser spherical structure in **Figure 7b**. It is worth noting that the AceS precursor solution has a significantly lower sucrose/lithium salt molar ratio at 1:15 compared to 1:1.5 in NitS and 1:1.18 in CarS. Given the 22.8 wt.% carbon content in Li_2CO_3-C_{AceS}, it is believed the generated acetone during

the pyrolysis of CH_3COOLi must function as the major source for carbon formation. The TEM image of the carbon matrix after Li_2CO_3 removal in **Figure 8e** reveals the distribution of Li_2CO_3 in the Li_2CO_3-C_{AceS} nanoparticles is not as uniform as in Li_2CO_3-C_{NitS}. The carbon matrix has a golf ball-like structure with relatively large pores, previously occupied by Li_2CO_3, distributed within. The specific surface area of Li_2CO_3-$C_{Ace\text{-}S}$ is 76.3 m^2 g^{-1}, which increases to 184.9 m^2 g^{-1} after Li_2CO_3 removal (Figure 3). This modest increase of surface area also indicates the relatively larger size of Li_2CO_3 compared to that of Li_2CO_3-C_{NitS}.

As shown in **Figure 7c**, the Li_2CO_3-C_{CarS} nanoparticles clearly have a different structure resembling crumpled spheres, which is due to the much lower solubility of Li_2CO_3 in water than those of $LiNO_3$ and CH_3COOLi. The concentration of Li_2CO_3 in the CarS precursor solution is 0.1 M, which is close to saturation. [27] Therefore, Li_2CO_3 undergoes fast and uniform precipitation from the aerosol droplets' evaporation in ASP, following the volume precipitation mechanism. [26] In addition, the ASP of CarS precursor also releases fewer gaseous species without decomposition of Li_2CO_3. Both factors contribute to better confinement and more uniform distribution of Li_2CO_3. After Li_2CO_3 removal, the carbon matrix retains its original structure with apparently higher porosity as shown in **Figure 7f**. The specific surface area of Li_2CO_3-C_{CarS} nanoparticles is 43.7 m^2 g^{-1}, which increases to 443.6 m^2 g^{-1} after Li_2CO_3 removal (**Figure 6**).

The Li_2CO_3-C nanoparticles obtained via ASP were sequentially reacted with mixed hydrogen sulfide and argon gas (H_2S/Ar at 5/95 vol.%) at 725°C to yield the Li_2S-C composites according to **Reaction 4**, confirmed by the XRD patterns shown in **Figure 6b**.

$$Li_2CO_3 + H_2S \rightarrow Li_2S + H_2O + CO_2 \qquad (4)$$

The TEM images of the Li_2S-C composites in **Figures 7g-i** demonstrate that these nanoparticles sustain their original structures after the conversion to Li_2S from Li_2CO_3.

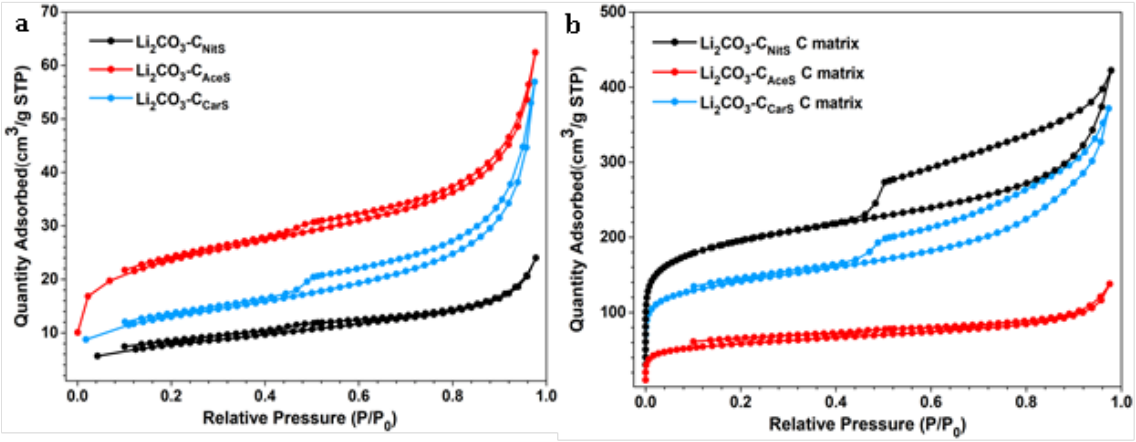

Figure 8. N2 adsorption-desorption isotherms of (a) Li2CO3-C nanoparticles and (b) the carbon matrix after Li2CO3 removal.

Figures 9a-c show the first three cyclic voltammetry (CV) cycles of the Li_2S-C versus Li counter/reference electrode in two-electrode cells. The cathodic peak in the first delithiation scan of Li_2S-C_{NitS} is centered at 3.5 V with a small shoulder at 3.4 V. The Li_2S-C_{AceS} composite demonstrates a broader delithiation peak at the same potential. In contrast, Li_2S-C_{CarS} shows two distinct cathodic peaks at 2.75 V and 3.4 V versus Li^+/Li. The lower cathodic peak of the Li_2S-C_{CarS} composite at 2.75 V indicates a lower energy barrier for the delithiation reaction. [28] The Li_2S-C_{CarS} composite also demonstrates the highest peak current in the consecutive lithiation-delithiation scans. The superior performance of Li_2S-C_{CarS} may be reflective of the intimate contact of Li_2S and the carbon matrix. Thus, it is consistent with Li_2S-C_{CarS} demonstrating the best cycling performance, as indicated by the average cycle stability (minimal three electrodes from each composite) displayed in **Figure**

9d. Using an electrolyte/Li_2S-C ratio of 7:1 (μL/mg), all Li_2S-C composites are first charged to 3.5 V versus Li^+/Li with 50 mA g^{-1}. After the first charge, reversible discharge capacities between 450 mAh g^{-1} and 500 mAh g^{-1} based on Li_2S-C composites are achieved under 100 mA g^{-1} cycling current. After 200 cycles, Li_2S-C_{CarS} can retain a capacity of 380 mAh g^{-1}, superior to 320 mAh g^{-1} of Li_2S-C_{NitS} and 270 mAh g^{-1} of Li_2S-C_{AceS}, indicating the effectiveness of the Li_2S-C_{CarS} composite architecture in sequestering polysulfides. The overall performance demonstrated by Li_2S-$C_{CarS,}$ in terms of areal loading, E/Li_2S ratio, capacity, and cycle stability, is on par with the best performance reported to date.

In summary, we examined a new synthetic route for the production of Li_2S-C composite materials for Li-S batteries. The combination of aerosol spray pyrolysis and sulfurization has been shown to be a robust method for the conversion of various lithium salts including nitrate, acetate, and carbonate to Li_2S-C nanocomposites using sucrose as the carbon precursor. Furthermore, the cycling performance of the Li_2S-C composite has been found to be closely correlated to its precursor-derived microstructure. The combination of Li_2CO_3 and sucrose results in the Li_2S-C composite with the best electrochemical performance, which has a non-hollow composite structure with Li_2S uniformly embedded in the carbon matrix. The detailed mechanism of aerosol spray pyrolysis and the optimization of the composite's structure and electrochemical performance will be further investigated.

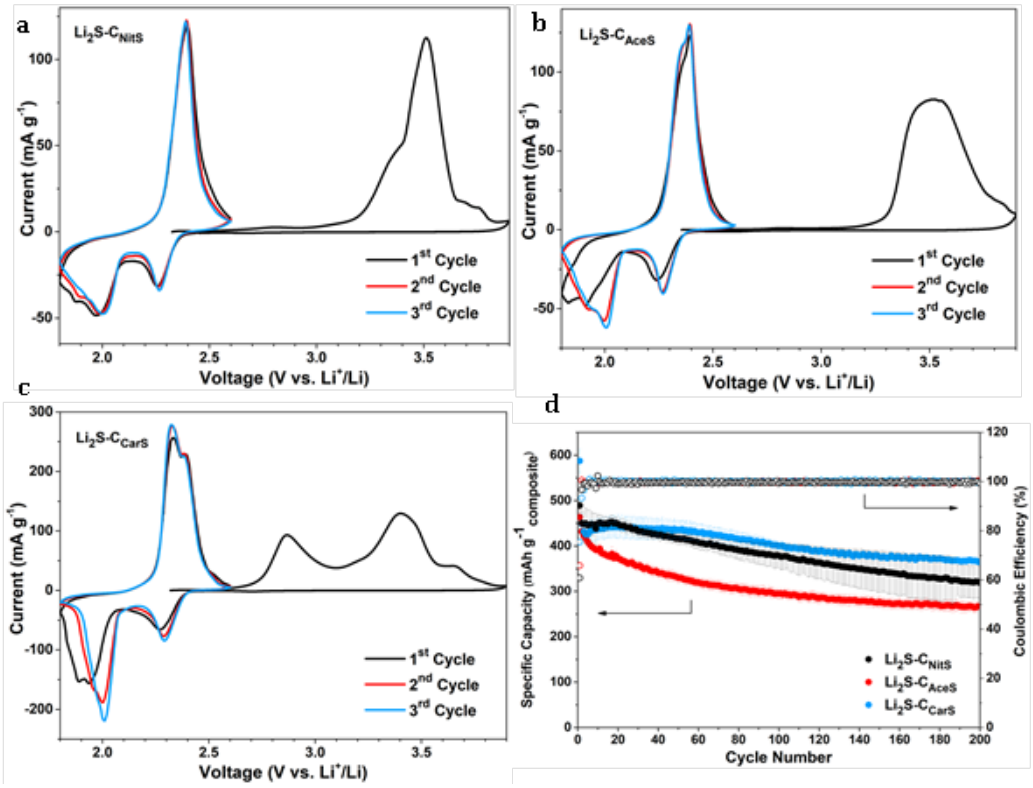

Figure 9. Figure 9. CV scans of (a) Li2S-CNit-S, (b) Li2S-CAce-S, (c) Li2S-CCar-S, and (d) the cycling stability of these composites at C/10.

Reference

1 Son, Y., Son, Y., Lee, J., Jang, J., Cho, J. Recent Advances in Lithium Sulfide Cathode Materials and Their Use in Lithium Sulfur Batteries. Adv. Energy Mat. 2015, DOI:10.1002/aenm.201500110.

2 Wang, D., Zeng, Q., Zhou, G., Yin, L., Li, F., Cheng, H., Gentle. I. R. Lu, Q.G. Carbon-Sulfur Composites for Li-S Batteries: Status and Prospects. J. Mat. Chem. A. 2013, 1, 9382-9394.

3 Wu S. D., Shi F., Zhou G., Zu C., Liu C., Liu K., Liu Y., Wang J., Peng Y., Cui Y.. Quantitative Investigation of Polysulfide Adsorption Capability of Candidate Materials for Li-S Batteries. Energy Storage Materials. 2018, 13, 241-246.

4 Chen S., Gao Y., Yu Z., Gordin L. M., Song J., Wang D.. High Capacity of Lithium-Sulfur Batteries at Low Electrolyte/Sulfur Ratio Enabled by an Organosulfide Containing Electrolyte. Nano Energy. 2017, 31, 418-423.

5 Pan H., Han S. K., Engelhard H. M., Cao R., Chen J., Zhang J., Mueller T. K., Shao Y., Liu J.. Addressing Passivation in Lithium–Sulfur Battery Under Lean Electrolyte Condition. Adv. Funct. Mater.. 2018, 1707234. DOI: 10.1002/adfm.201707234.

6 Chen J., Henderson A. W., Pan H., Perdue R B., Cao R., Hu J., Wan C., Han K., Mueller T. K., Zhang J., Shao Y., Liu J.. Improving Lithium−Sulfur Battery Performance under Lean Electrolyte Through Nanoscale Confinement in Soft Swellable Gels. Nano Lett. 2017, 17, 3061−3067.

7 Yang Y., McDowell T. M., Jackson A., Cha J. J., Hong S., Cui Y.. New Nanostructured Li2S/Silicon Rechargeable Battery with High Specific Energy. Nano Lett. 2010, 4, 1486-1491.

8 Jha, H., Buchberger I., Cui X., Meini S., Gasteiger H. A.. Li-S Batteries with Li2S Cathodes and Si/C Anodes. J. Electochem. Soc., 2015, 162, 9, 1829-1835.

9 Hwa, Y., Zhao, J., Cairns, E. J. Lithium Sulfide (Li2S)/Graphene Oxide Nanospheres with Conformal Carbon Coating as a High-Rate, Long-Life Cathode for Li/S Cells. Nano Lett., 2015, 15, 3479-3486.

10 Fu C., Li G., Zhang J., Cornejo B., Piao S. S., Bozhilov N. K., Haddon C. R., Guo J.. Electrochemical Lithiation of Covalently Bonded Sulfur in Vulcanized Polyisoprene. ACS Energy Lett. 2016, 1, 115−120. DOI: 10.1021/acsenergylett.6b00073.

11 Wu F., Lee J., Magasinski A., Kim H., Yushin G. Solution-Based Processing of Graphene-Li2S Composite Cathodes for Lithium-Ion and Lithium-Sulfur Batteries. Part. Part. Syst. Charact.. 2014, 31, 639–644. Doi: org/10.1002/ppsc.201300358.

12 Wu F., Magasinski A., Yushin G. Nanoporous Li2S and MWCNT-Linked Li2S Powder Cathodes for Lithium-Sulfur and Lithium-ion Battery Chemistries. J. Mater. Chem. A. 2014, 2, 6064–6070.

13 Wu F., Kim H., Magasinski A., Lee J., Lin H., Yushin G.. Harnessing Steric Separation of Freshly Nucleated Li2S Nanoparticles for Bottom-Up Assembly of High-Performance Cathodes for Lithium-Sulfur and Lithium-Ion Batteries. Adv. Energy Mater. 2014, 4, 1400196. Doi.org/10.1002/aenm.201400196.

14 Wu F., Lee J., Fan F., Nitta N., Kim H., Magasinski A., Zhu T., Yushin G.. A Hierarchical Particle‐Shell Architecture for Long‐Term Cycle Stability of Li2S Cathodes. Adv. Mater. 2015, 27, 5579‐5586. Doi.org/10.1002/adma.201502289.

15 Wu F., Lee J., Zhao E., Zhang B., Yushin G.. Graphene–Li2S–Carbon Nanocomposite for Lithium–Sulfur Batteries. ACS Nano. 2016, 10, 1333−1340.

16 Guo J., Yang Z., Yu Y., Abruna D. H., Archer A. L.. Lithium−Sulfur Battery Cathode Enabled by Lithium−Nitrile Interaction. J. Am. Chem. Soc. 2013, 135, 763−767.

17 Tan G., Xu R., Xing Z., Yuan Y., Lu J., Wen J., Liu C., Ma L., Zhan C., Liu Q., Wu T., Jian Z., Yassar R., Ren Y., Miller D. J., Curtiss L. A., Ji X., Amine K.. Burning lithium in CS2 for high-performing compact Li2 S–graphene nanocapsules for Li–S batteries. Nature Energy. 2017, 2, 17090

18 Li, Z., Zhang, S., Zhang, C., Ueno, K., Yasuda, T., Tatara, R., Dokko K., Watanabe, M.. One-Pot Pyrolysis of Lithium Sulfate and Graphene Nanoplatelet Aggregates: In Situ Formed Li2S/ Graphene Composite for Lithium–Sulfur Batteries. Nanoscale, 2015, 7, 14385-14392.

19 Yang Z., Guo J., Das K. S., Yu Y., Zhou Z., Abruna D. H., Archer A. L.. In Situ Synthesis of Lithium Sulfide–Carbon Composites as Cathode Materials for Rechargeable Lithium Batteries. J. Mater. Chem. A. 2013, 1, 1433.

20 Zhang J., Shi Y., Ding Y., Peng L., Zhang W., Yu G.. A Conductive Molecular Framework Derived Li2S/N,P-Codoped Carbon Cathode for Advanced Lithium − Sulfur Batteries. Adv. Energy Mater.. 2017, 7, 1602876. doi.org/10.1002/aenm.201602876.

21 Kohl M., Bruckner J., Bauer I., Althues H., Kaskel S.. Synthesis of Highly Electrochemically Active Li2S Nanoparticles for Lithium–Sulfur-Batteries. J. Mater. Chem. A, 2015, 3, 16307-16312.

22 Yu M., Wang Z., Wang Y., Dong Y., Qiu J.. Freestanding Flexible Li2S Paper Electrode with High Mass and Capacity Loading for High-Energy Li-S Batteries. Adv. Energy Mater. 2017, 7, 1700018. DOI: 10.1002/aenm.201700018.

23 Skrabalak, Sara E.; Suslick, Kenneth S. Porous Carbon Powders Prepared by Ultrasonic Spray Pyrolysis. J. Am. Chem. Soc. 2016, 128, 39, 12642-12643.

24 Stern, K. H., Weise, E. L.. High Temperature Properties and Decomposition of Inorganic Salts; Part 2. Carbonates. 1969, United States Dept of Commerce.

25 Roe A., Finlay J. B.. The Isotope Effect II, Pyrolysis of Lithium Acetate 1-C14. J. Am. Chem. Soc. 1952, 74, 9, 2442-2443.

26 Messing, G., Zhang, S. and Jayanthi, G.. Ceramic Powder Synthesis by Spray Pyrolysis. J. Am. Ceram. Soc. 1993, 76, 11, 2707-2726.

27 Zou H., Gratz E., Apelian D., Wang Y.. A Novel Method to Recycle Mixed Cathode Materials for Lithium Ion Batteries. Green Chem., 2013, 15, 1183.

28 Zhou G., Tian H., Jin Y., Tao X., Liu B., Zhang R., She Z., Zhou D., Liu Y., Sun J., Zhao J., Zu C., Wu D., Zhang Q., Cui Y.. Catalytic Oxidation of Li2S on the Surface of Metal Sulfides for Li−S Batteries. PNAS. 2017, 114(5) 840-845. https://doi.org/10.1073/pnas.1615837114

2.2 Li_2SO_4 as The Precursor

Pre-lithiated sulfur materials are promising cathode for lithium-sulfur batteries. The synthesis of lithium sulfide-carbon (Li_2S-C) composite by carbothermic reduction of lithium sulfate (Li_2SO_4) is investigated in this study. The relationship between reaction temperature and the consumption of carbon in the carbothermic reduction of Li_2SO_4 is first investigated to precisely control the carbon content in the resultant Li_2S-C composites. To understand the relationship between the material structure and the electrochemical properties, Li_2S-C composites with the same carbon content are subsequently synthesized by controlling the mass ratio of Li_2SO_4/carbon and the reaction temperature. Systematic electrochemical analyses and microscopic characterizations demonstrate that the size of the Li_2S particles dispersed in the carbon matrix is the key parameter determining electrochemical performance. A reversible capacity of 600 mAh g^{-1} is achieved under lean electrolyte conditions with high Li_2S areal loading.

Introduction: Lithium-sulfur (Li-S) batteries have received intensive investigations over the past decade due to their great potential as a high-capacity rechargeable battery technology.[1-7] To eliminate the potential safety hazard induced by the Li metal anode, high-capacity non-Li anodes, particularly silicon-based materials, have been sought as the

alternative.[8-12] Utilizing non-Li anodes requires lithium sulfide (Li_2S) cathode materials, which have been produced by a number of methods reported in the literature. The most common method is to physically mix Li_2S and carbon materials with high-energy ball milling.[13-18] Li_2S solution in ethanol was used to deposit Li_2S on various carbon structures.[19-26] Other solvent such as anhydrous methyl acetate was also used to disperse Li_2S in carbon.[27] A number of chemical methods were also reported: Li_2S-C composite could be produced from sulfurization of lithium carbonate with H_2S.[28,29] Li_2S-C composite was also synthesized via the reaction between lithium polysulfides and the nitrile group in polyacrylonitrile.[30] A recently reported novel method utilized the thermal reaction between metallic Li and gaseous carbon disulfide (CS_2) to form carbon coated Li_2S in one step.[31] Another chemical method to produce Li_2S-C composites is to convert lithium sulfate (Li_2SO_4) to Li_2S via carbothermic reduction.[32-39] Comparing to all other methods mentioned above, carbothermic reduction of Li_2SO_4 involves neither hazardous gas such as gaseous CS_2 or H_2S nor air sensitive reactants such as Li_2S or Li metal. Furthermore, Li_2S-C composites can be produced in one-step reaction in carbothermic reduction of Li_2SO_4. In this study, we focus on understanding the effect of reaction temperature on stoichiometric ratio of C/Li_2SO_4 in the carbothermic reduction and the structure-property relationship of the obtained Li_2S-C composites as the cathode materials for Li-S batteries.

Temperature Effect on C/Li2SO4 Stoichiometric Ratio: All reagents were used after purchase without further purification unless otherwise noted. Ketjen black EC-600JD (KJB, purchased from AkzoNobel) was used as the carbon source in this study. To minimize the effect of the impurity in KJB (mainly oxygen) on the carbothermic reduction

of Li_2SO_4, KJB was treated by hydrogen reduction: In a typical experiment, approximately 400 mg KJB was heated under hydrogen/argon (5%/95%) environment at 1000°C for 3 hours. Elemental contents of KJB before and after the hydrogen treatment were analyzed as shown in **Table 2**.

Table 2. Elemental analysis of KJB before and after the hydrogen reduction treatment.

Elements	C (wt.%)	H (wt.%)	N (wt.%)	O (wt.%)
Before	97.72	0.48	0.29	1.51
After	98.87	0.22	0.17	0.74

Li_2SO_4 and KJB was thoroughly mixed by mechanical ball milling with different weight ratios including 2.0:1, 2.3:1, 2.5:1 and 2.9:1. The mixture was heated in a tube furnace under flowing argon (Ar) environment to form Li_2S-C composite. The temperature of the tube furnace was first raised to 200°C from room temperature at 5°C min^{-1}. The temperature was held at 200°C for 2 hrs, followed by further increasing to neither 700°C or 750°C at 5°C min^{-1}. The temperature was kept at 700°C or 750°C for 6 hrs to complete the carbothermic reduction of Li_2SO_4. Ethanol was used to leach out the Li_2S in the resultant Li_2S-C composite to measure the conversion of Li_2SO_4 and carbon content, from which the C/Li_2SO_4 stoichiometric ratio in the carbothermic reduction can be calculated.

Li_2S-C Composite Synthesis and Characterization: To improve the areal loading the Li_2S-C composite at the cathode, micro-sized carbon particles were first synthesized with KJB as the precursor following the method reported by Lv and coworkers.[40] In a typical synthesis of Li_2S-C composite, the micro-sized carbon particles were mixed into 5 mL

aqueous solution of Li_2SO_4 with specific Li_2SO_4/C ratio, followed by dispersion by sonication for 5 mins and thorough stir for additional 24 hrs. 100 mL ethanol was then added into the mixture and stirred for 10 min. The Li_2SO_4-C dispersion in the water/ethanol mixture was dried with rotary evaporator at 90°C. The obtained Li_2SO_4-C mixture was further dried at 80°C under vacuum overnight. To produce the Li_2S-C composite, 0.5 g of Li_2SO_4-C mixture was heated under flowing Ar environment in a tube furnace using the same process as aforementioned.

The Li_2S-C composite was characterized by powder X-Ray diffraction (XRD, PANalytical). Kapton tape was used to seal the XRD sample to prevent Li_2S from reacting with moisture in the ambient environment. Nitrogen adsorption-desorption isotherms of the Li_2S-C composites were measured with a surface area and porosity analyzer (Micromeritics ASAP2020). The surface area was obtained with the Brunauer-Emmett-Teller (BET) method. To avoid Li_2S reacting with environmental moisture, all Li_2S-C composites were transferred into the BET sample tube in the glovebox and sealed with Teflon tape. The microstructure of the Li_2S-C composites was characterized with scanning electron microscopy (SEM) and elemental mapping was obtained by energy-dispersive X-ray spectroscopy (EDX). To perform the SEM characterization, the samples were carefully sealed into a stainless-steel vacuum tube in an Ar-filled glovebox. The sample tube was transferred into the SEM chamber under flowing argon protection using a glove-bag.

Electrode Fabrication, Cell Assembly and Testing: To prepare the electrode, Li_2S-C composite was mixed with carbon black and polyvinylidene difluoride with a weight ratio of 85:5:10 in N-methyl-2-pyrrolidone. The obtained slurry was uniformly pasted on a

carbon coated aluminum foil current collector and dried in the Ar-filled glovebox at 135°C for at least 15 hours. The dried electrodes were assembled into 2032-type coin cells with Li foil anode (99.9%, Alfa Aesar) and Celgard® 2500 separator. The electrolyte used in this study was 1M lithium bis(trifluoromethanesulfonyl)imide solution in a mixture of 1,3-dioxolane, dimethoxyethane and 1-butyl-1-methylpyrrolidinium bis(trifluoromethanesulfonyl)imide (1:1:2 by vol.) with 1.5 wt.% of $LiNO_3$. The electrolyte to Li_2S ratio (μL/mg) was kept at 7 in all coin cells testing. The average areal loading of Li_2S on the electrode is 2 mg cm^{-2}. The first charge (activation) was performed at a rate of C/50 (24 mA g^{-1}) to a charge cutoff of 3.8 V vs. Li^+/Li. The subsequent cycles were performed at C/10, C/5, C/2, and 1C between 2.8 V and 1.7 V.

Results and Discussion: Despite the previous reports on synthesizing Li_2S-C composites via carbothermic reduction of Li_2SO_4, the influence of reaction temperature on the stoichiometric ratio between carbon and Li_2SO_4 has not been investigated. As shown in **Reaction 1**, carbothermic reduction of Li_2SO_4 generally produces both carbon dioxide (CO_2) and carbon monoxide (CO).[41,42] However, the ratio between CO_2 and CO changes with temperature due to their different stability as the function of temperature. Therefore, the carbothermic reduction of Li_2SO_4 can be expressed as **Reaction 2**, in which the stoichiometric ratio of C/Li_2SO_4, $\boldsymbol{x}$, is a function of temperature. To synthesize Li_2S-C composite in one-step carbothermic reduction with precise carbon content, it is critical to learn the value of $\boldsymbol{x}$ at different temperatures.

$$\boldsymbol{Li_2SO_4 + xC \rightarrow Li_2S + yCO_2 + zCO} \qquad \textbf{[1]}$$

$$\boldsymbol{Li_2SO_4 + xC \rightarrow Li_2S + xCO_{4/x}} \qquad \textbf{[2]}$$

With certain Li_2SO_4/C mass ratio (carbon in excess) and assumption of 100% conversion of Li_2SO_4 to Li_2S, the Li_2S content in the Li_2S-C composite from the carbothermic reduction can be calculated as the function of the stoichiometric ratio of C/Li_2SO_4 as shown in **Figure 10**. The four solid lines represent four different Li_2SO_4/C mass ratio, 2.0:1, 2.3:1, 2.5:1 and 2.9:1, which all have excess of carbon. Carbothermic experiments were first performed with Li_2SO_4/C mass ratio of 2.0:1, 2.3:1 and 2.5:1 at 700 and 750°C. The reaction at each condition (temperature and Li_2SO_4/C mass ratio) was repeated at least three times to minimize experimental errors. The content of Li_2S in the resultant Li_2S-C composite was measured and the results demonstrated full conversion of Li_2SO_4 to Li_2S in all experiments. Therefore, the stoichiometric ratio of C/Li_2SO_4, ***x***, was calculated at all experimental conditions and the average values were marked on the theoretic curves in **Figure 10**. It is clear that the stoichiometric ratio of C/Li_2SO_4 is lower at 700°C, indicating less carbon is consumed at lower temperature with higher CO_2 content in the gaseous products. The experimental results can also be linearly fitted to obtain an empirical relationship between Li_2S content in Li_2S-C and the stoichiometric C/Li_2SO_4 ratio at different temperature. The empirical relationship at 700°C is $\boldsymbol{Li_2S\ wt.\% = 175.3 - 54.9x}$ (red dotted line) and the one at 750°C is $\boldsymbol{Li_2S\ wt.\% = 212.0 - 58.6x}$ (blue dotted line).

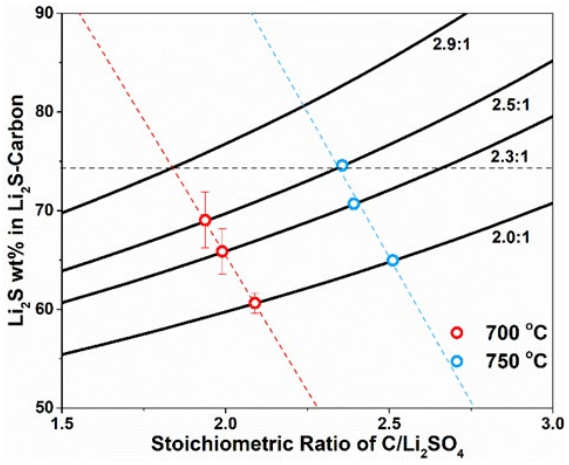

Figure 10. Mass ratio of Li2S in the Li2S-C composite as the function of stoichiometry ratio of C/Li2SO4 with different Li2SO4/C mass ratio at 2.0:1, 2.3:1, 2.5:1 and 2.9:1 at 700 and 750 °C.

To study the structure-property relationship of the Li_2S-C composites, we need to select a composite from each reaction temperature with same Li_2S content. One selected Li_2S-C composite is produced at 750°C with Li_2SO_4/C mass ratio of 2.5:1, which contains 72 wt.% of Li_2S. The same Li_2S content was projected on the empirical linear fitting of Li_2S content vs. stoichiometric C/Li_2SO_4 ratio at 700°C, from which the required Li_2SO_4/C mass ratio was calculated to be 2.9:1. The carbothermic reduction of Li_2SO_4 at 700°C with Li_2SO_4/C mass ratio of 2.9:1 yielded Li_2S-C with 71 wt.% Li_2S content, which agreed very well with the prediction.

The two Li_2S-C composites with the same Li_2S content are denoted as Li_2S-C_{700} and Li_2S-C_{750} according to the reaction temperature. The XRD patterns of these two composites in **Figure 11a** indicate well crystallized Li_2S formed from the carbothermic reduction of Li_2SO_4. The broad peak around 20° is due to the Kapton tape protecting Li_2S from reacting to the ambient moisture. Based on the full-width at half-maximum of the XRD peaks, Li_2S-

C_{750} has smaller crystal grain size than that of Li_2S-C_{700}. The BET surface areas of these two Li_2S-C composites from the N_2 adsorption-desorption isotherms (**Figure 11b**) are very close: 350.8 m^2 g^{-1} for Li_2S-C_{750} and 326.8 m^2 g^{-1} for Li_2S-C_{700}. We believe the higher carbon content in the Li_2SO_4-C mixture at the 750°C reaction alleviated the particle aggregation thus leading to smaller Li_2S particles.

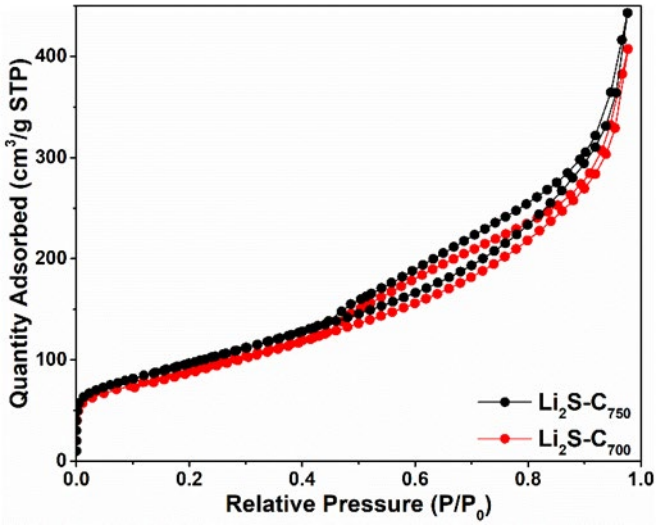

Figure 11. (a) XRD patterns and (b) N2 adsorption-desorption isotherms of the Li2S-C composites at different temperature.

SEM was used to characterize the microstructure of the Li_2S-C composites. **Figure 12a** shows the structure of the Li_2SO_4/C mixture before carbothermic reduction for Li_2S-C_{750}. Li_2SO_4 exhibited typical monoclinic crystal structure as hexagonal plate with crystal size around 10 μm. Interestingly, the carbothermic reduction of Li_2SO_4 yielded spherical Li_2S particles dispersed in carbon matrix as displayed in the SEM image in **Figure 12b** and the EDX elemental mapping in **Figures 12c** and **12d**. The SEM characterization of the Li_2S-C_{700} demonstrated very similar microstructure with Li_2S-C_{750}. The particle size of Li_2S was measured by ImageJ software and the average particle size was analysed by Gaussian

distribution over 600 particles. As the particle size distribution shown in **Figures 12e** and **12j**, the Li_2S particle size in Li_2S-C_{750} was smaller than that in Li_2S-C_{700} consistent with the SEM result: The average Li_2S particle size was 4.4 μm in Li_2S-C_{750} and 6.4 μm in Li_2S-C_{700}.

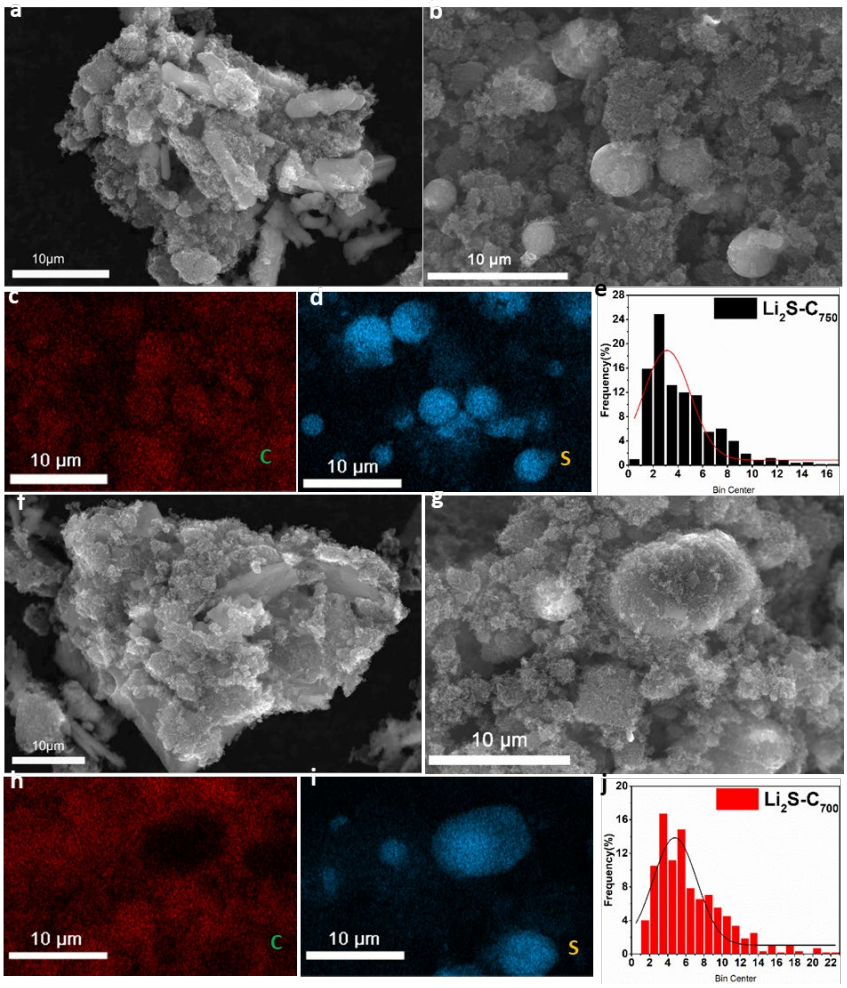

Figure 12. (a) SEM image of Li2SO4-C mixture with Li2SO4/C mass ratio of 2.5:1, (b) SEM image, (c, d) EDX elemental mapping and (e) Li2S size distribution of Li2S-C750; (f) SEM image of Li2SO4-C mixture with Li2SO4/C mass ratio of 2.9:1, (g) SEM image, (h, i) EDX

Figures 13a and **13b** show the CV cycles of Li_2S-C_{750} and Li_2S-C_{700} electrodes. The Li_2S-C_{750} electrode demonstrated slightly lower delithiation potential than Li_2S-C_{700} in the first

cycle (3.5 V vs. 3.6 V for the cathodic peak, respectively). This observation is consistent with the first galvanostatic delithiation curves of these two composites shown in **Figures 13c** and **13d**. We speculate that the lower delithiation overpotential of Li_2S-C_{750} is attributed to its structural advantage, mainly smaller Li_2S particle size. Previous reports also confirmed that the first delithiation potential had connection with Li_2S size which could arise from carbothermic reduction temperature and carbon precursors.[43,44] Apart from particle size, the differences of activation behaviour shown in the first charge of **Figures 13c** and **13d** might be caused from carbon host material, PVdF binder, and presence of insulating oxidized products such as Li_2SO_4, Li_2CO_3, and Li_2O. The better microstructure of Li_2S-C_{750} is also evidenced by the lower charge-discharge potential hysteresis (**Figures 13c** and **13d**), better cycle stability and improved rate capability shown in **Figures 13e** and **13f**. Produced polysulfide from first few cycles might cause the activation behaviour shown in the first ten cycles of Li_2S-C_{700} at C/10 in **Figure 13f** which can also be seen in previous reports. The average initial discharge capacity of Li_2S-C_{750} is 600 mAh g^{-1} (average of 3 electrodes), and 400 mAh g^{-1} capacity was retained after 200 cycles at C/5. In **Figures 13e**, when cycled at C/2, smaller size Li_2S-C_{750} retained 350 mAh g^{-1} capacity which was almost three times of Li_2S-C_{700}. It is clear that particle size of Li_2S is a critical parameter for rate performance of Li_2S batteries as shown**.**

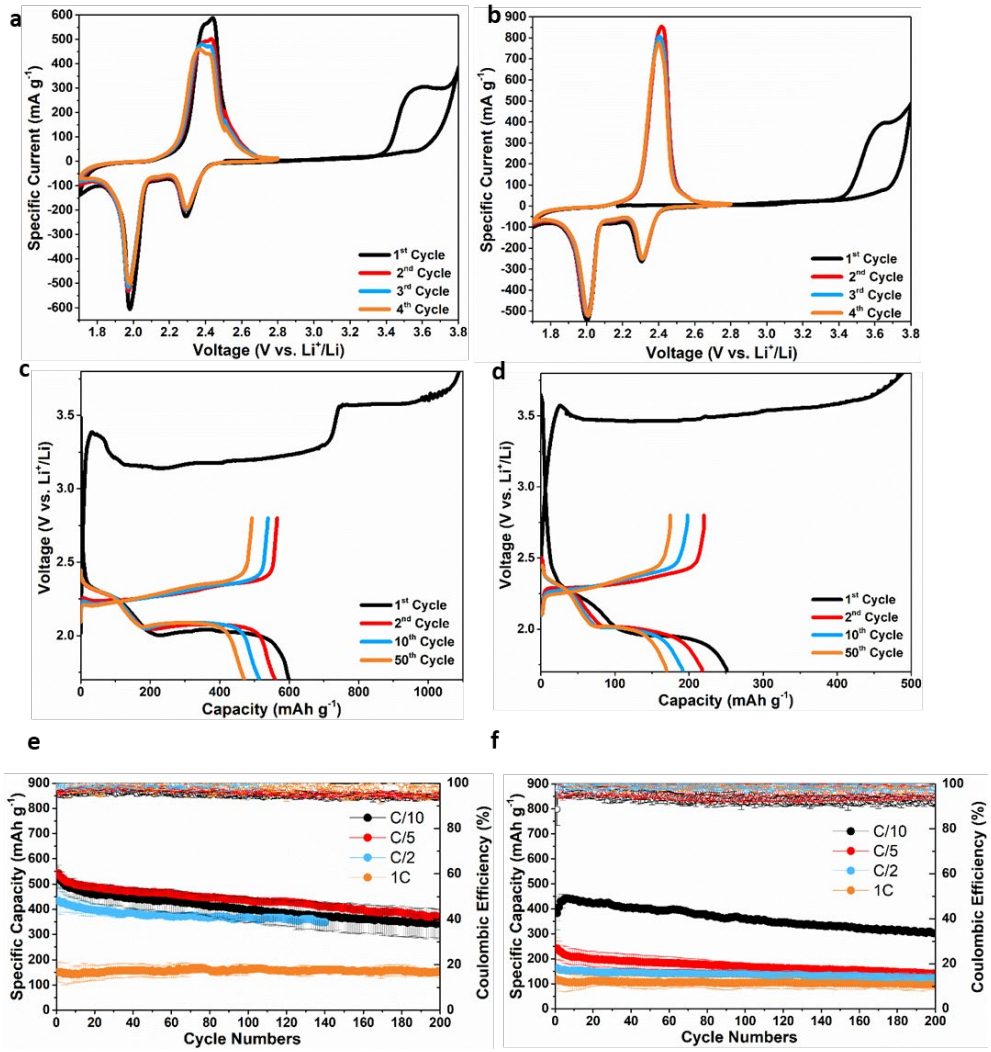

Figure 13. CV curves of (a) Li2S-C750 and (b) Li2S-C700; the 1st, 2nd, 10th, and 50th cycles of charge-discharge of (c) Li2S-C750 and (d) Li2S-C700 at C/5; the cycle stability at C/10, C/5, C/2 and 1C of (e) Li2S-C750 and (f) Li2S-C700.

Conclusion: In summary, the synthetic route of Li_2S-C from carbothermic reduction of Li_2SO_4 was investigated in this study. Particularly the relationship between reaction temperature and stoichiometric ratio of C/Li_2SO_4 in the carbothermic reduction was obtained for the first time. Through investigations on microstructures and electrochemical properties, we speculated that smaller Li_2S particle size dispersed in carbon matrix is the

key parameter to improve the electrochemical performance. Methods to further reduce particle size of Li_2S via carbothermic reduction of Li_2SO_4 will be investigated in future studies.

Reference

1 Ma, L.; Hendrickson, K. E.; Wei, S.; Archer, L. A. (2015). Nanomaterials: Science and Applications in the Lithium-Sulfur Battery. Nano Today, 10, 315-338.

2 Fang, R.; Zhao, S.; Sun, Z.; Sun, Z.; Wang, D.; Cheng, H.; Li, F. (2017). More Reliable Lithium-Sulfur Batteries: Status, Solutions and Prospects. Adv. Mater. 29, 1606823. DOI: 10.1002/adma.201606823.

3 Peng, H.; Huang, J.; Cheng, X.; Zhang, Q. (2017). Review on High-Loading and High-Energy Lithium-Sulfur Batteries. Adv. Energy Mater. 7, 1700260. DOI: 10.1002/aenm.201700260.

4 Wild, M.; O'Neill, L.; Zhang, T.; Purkayastha, R.; Minton, G.; Marinescu, M.; Offer, G. J. (2015). Lithium Sulfur Batteries, A Mechanistic Review. Energy Environ. Sci., 8, 3477.

5 Zheng, S.; Li, X.; Yan, B.; Hu, Q.; Xu, Y.; Xiao, X.; Xue, H.; Pang, H. (2017). Transition-Metal (Fe, Co, Ni) Based Metal-Organic Frameworks for Electrochemical Energy Storage. Adv. Energy Mater. 7, 1602733. DOI: 10.1002/aenm.201602733.

6 Manthiram, A.; Chung, S.; Zu, C. (2015). Lithium-Sulfur Batteries: Progress and Prospects. Adv. Mater. 27, 1980-2006. DOI: 10.1002/adma.201405115.

7 Chen, L.; Guo, X.; Lu, W.; Chen, M.; Li, Q.; Xue, H.; Pang, H. (2018). Manganese Monoxide-based Materials for Advanced Batteries. Coordination Chemistry Reviews. 368, 13-34.

8 Agostini, M.; Hassoun, J.; Liu, J.; Jeong, M.; Nara, H.; Momma, T.; Osaka, T.; Sun, Y.; Scrosati, B. (2014). A Lithium-Ion Sulfur Battery Based on A Carbon-Coated Lithium-Sulfide Cathode and An Electrodeposited Silicon-Based Anode. Acs Appl. Mater. Interfaces. 6, 10924-10928.

9 Yang, Y.; McDowell, M. T.; Jackson, A.; Cha, J. J.; Hong, S. S.; Cui, Y. (2010). New Nanostructured Li_2S/Silicon Rechargeable Battery with High specific Energy. Nano Lett., 10 (4), 1486-1491. DOI: 10.1021/nl100504q.

10 Guo, X.; Zheng, S.; Zhang, G.; Xiao, X.; Li, X.; Xu, Y.; Xue, H.; Pang, H. (2017). Nanostructured Graphene-based Materials for Flexible Energy Storage. Energy Storage Materials. 9, 150-169.

11 Jha, H.; Buchberger, I.; Cui, X.; Meini, S.; Gasteiger, H. A. (2015). Li-S Batteries with Li_2S Cathodes and Si/C Anodes. Journal of The Electrochemical Society, 162 (9), A1829-A1835.

12 Cao, R.; Xu, W.; Lv, D.; Xiao, J.; Zhang, J. (2015). Anodes for Rechargeable Lithium-Sulfur Batteries. Adv. Energy Mater. 5, 1402273. DOI: 10.1002/aenm.201402273.

13 Liang, S.; Liang, C.; Xia, Y.; Xu, H.; Huang, H.; Tao, X.; Gan, Y.; Zhang, W. (2016). Facile Synthesis of Porous Li_2S@C Composites as Cathode Materials for Lithium-Sulfur Batteries. Journal of Power Sources. 306, 200-207.

14 Liu, J.; Nara, H.; Yokoshima, T.; Momma T.; Osaka, T. (2015). Li_2S Cathode Modified with Polyvinylpyrrolidone and Mechanical Milling with Carbon. Journal of Power Sources. 273, 1136-1141.

15 Lee, S.; Lee, Y. J., Sun, Y. (2016). Nanostructured Lithium Sulfide Materials for lithium-Sulfur Batteries. Journal of Power Sources. 323, 174-188.

16 Jeong, S.; Bresser, D.; Buchholz, D.; Winter, M.; Passerini, S. (2013). Carbon Coated Lithium Sulfide Particles for Lithium Battery Cathodes. Journal of Power Sources, 235, 220-225.

17 Chen, L.; Liu, Y.; Ashuri, M.; Liu, C.; Shaw, L. L. (2014). Li_2S Encapsulated by Nitrogen-Doped Carbon for Lithium Sulfur Batteries. J. Mater. Chem. A, 2, 18026. DOI: 10.1039/c4ta04103h.

18 Cai, K.; Song, M.; Cairns, E.; Zhang, Y. (2012). Nanostructured Li_2S-C Composites as Cathode Material for High-Energy Lithium/Sulfur Batteries. Nano Lett. 2012, 12, 6474-6479.

19 Zhou, G.; Paek, E.; Hwang, G. S.; Manthiram, A. (2016). High-Performance Lithium-Sulfur Batteries with a Self-Supported, 3D Li_2S-Doped Graphene Aerogel Cathodes. Adv. Energy Mater. 2016, 6, 1501355. DOI: 10.1002/aenm.201501355.

20 Wang, C.; Wang, X.; Yang, Y.; Kushima, A.; Chen, J.; Huang, Y.; Li, J. (2015). Slurryless Li_2S/Reduced Graphene Oxide Cathode Paper for High-Performance Lithium Sulfur Battery. Nano Lett. 15, 1796-1802. DOI: 10.1021/acs.nanolett.5b00112.

21 Wu, F.; Lee, J.; Magasinski, A.; Kim, H.; Yushin, G. (2014). Solution-Based Processing of Graphene-Li_2S Composite Cathodes for Lithium-Ion and Lithium-Sulfur Batteries. Part. Part. Syst. Charact. 31, 639–644. DOI: org/10.1002/ppsc.201300358.

22 Wu, F.; Magasinski, A.; Yushin, G. (2014). Nanoporous Li_2S and MWCNT-Linked Li_2S Powder Cathodes for Lithium-Sulfur and Lithium-ion Battery Chemistries. J. Mater. Chem. A. 2, 6064–6070.

23 Wu, F.; Kim, H.; Magasinski, A.; Lee, J.; Lin, H.; Yushin, G. (2014). Harnessing Steric Separation of Freshly Nucleated Li_2S Nanoparticles for Bottom-Up Assembly of High-Performance Cathodes for Lithium-Sulfur and Lithium-Ion Batteries. Adv. Energy Mater. 4, 1400196. DOI: org/10.1002/aenm.201400196.

24 Wu, F.; Lee, J.; Fan, F.; Nitta, N.; Kim, H.; Magasinski, A.; Zhu, T.; Yushin, G. (2015). A Hierarchical Particle-Shell Architecture for Long-Term Cycle Stability of Li_2S Cathodes. Adv. Mater. 27, 5579–5586. DOI: org/10.1002/adma.201502289.

25 Wu, F.; Lee, J.; Zhao, E.; Zhang, B.; Yushin, G. (2016). Graphene-Li_2S-Carbon Nanocomposite for Lithium-Sulfur Batteries. ACS Nano. 10, 1333−1340.

26 Han, F.; Yue, J.; Fan, X.; Gao, T.; Luo, C.; Ma, Z.; Suo, L.; Wang, C. (2016). High-Performance All-Solid-State Lithium-Sulfur Battery Enabled by a Mixed-Conductive Li_2S Nanocomposite. Nano Lett. 16, 4521-4527.

27 Seh, Z. W.; Wang, H.; Hsu, P.; Zhang, Q.; Li, W.; Zheng, G.; Yao, H.; Cui, Y. (2014). Facile Synthesis of Li_2S-polypyrrole Composite Structures for High-performance Li_2S cathodes. Energy Environ. Sci., 7, 672-676.

28 Dressel, B. C.; Jha, H.; Eberle, A.; Gasteiger, A. H.; Fassler, F. T. (2016). Electrochemical Performance of Lithium-Sulfur Batteries Based on A Sulfur Cathode Obtained by H_2S Gas Treatment of a Lithium Salt. Journal of Power Sources. 307, 844-848.

29 Hart, N.; Shi, J.; Zhang, J; Fu, C.; Guo, J. (2018). Lithium Sulfide-Carbon Composites via Aerosol Spray Pyrolysis as Cathode Materials for Lithium-Sulfur Batteries. Front. Chem. 6, 674. DOI: 10.3389/fchem.2018.00476.

30 Guo, J.; Yang, Z.; Yu, Y.; Abruna, H. D.; Archer, L. A. (2013). Lithium-Sulfur Battery Cathode Enabled by Lithium-Nitrile Interaction. J. Am. Chem. Soc. 135, 763-767.

31 Tan, G.; Xu, R.; Xing, Z.; Yuan, Y.; Lu, J.; Wen, J.; Liu, C.; Ma, L.; Zhan, C.; Liu, Q.; Wu, T.; Jian, Z.; Yassar, R.; Ren, Y.; Miller, D. J.; Curtiss, L. A.; Ji, X.; Amine, K. (2017). Burning lithium in CS_2 for high-performing compact Li_2S-graphene nanocapsules for Li-S batteries. Nature Energy. 2, 17090.

32 Li, Z.; Zhang, S.; Zhang, C.; Ueno, K.; Yasuda, T.; Tatara, R.; Dokko, K.; Watanabe, M. (2015). One-Pot Pyrolysis of Lithium Sulfate and Graphene Nanoplatelet Aggregates: In Situ Formed Li_2S/ Graphene Composite for Lithium-Sulfur Batteries. Nanoscale. 7, 14385-14392.

33 Yang, Z.;Guo, J.; Das, K. S.; Yu, Y.; Zhou, Z.; Abruna, D. H.; Archer, A. L. (2013). In Situ Synthesis of Lithium Sulfide-Carbon Composites as Cathode Materials for Rechargeable Lithium Batteries. J. Mater. Chem. A. 1, 1433-1440.

34 Zhang, J.; Shi, Y.; Ding, Y.; Peng, L.; Zhang, W.; Yu, G. (2017). A Conductive Molecular Framework Derived Li_2S/N, P-Codoped Carbon Cathode for Advanced Lithium-Sulfur Batteries. Adv. Energy Mater. 7, 1602876. DOI: org/10.1002/aenm.201602876.

35 Kohl, M.; Bruckner, J.; Bauer, I.; Althues, H.; Kaskel, S. (2015). Synthesis of Highly Electrochemically Active Li_2S Nanoparticles for Lithium–Sulfur-Batteries. J. Mater. Chem. A. 3, 16307-16312.

36 Yu, M.; Wang, Z.; Wang, Y.; Dong, Y.; Qiu, J. (2017). Freestanding Flexible Li2S Paper Electrode with High Mass and Capacity Loading for High-Energy Li-S Batteries. Adv. Energy Mater. 7, 1700018. DOI: 10.1002/aenm.201700018.

37 Ye, F.; Noh, H.; Lee, J.; Lee, H.; Kim, H. (2018). Li_2S/Carbon Nanocomposite Strips from A Low-temperature Conversion of Li_2SO_4 as High-performance Lithium-Sulfur Cathodes. J. Mater. Chem. A. 6, 6617-6624.

38 Wang, D.; Xie, D.; Yang, T.; Zhang, Y.; Wang, X.; Xia, X.; Gu, C.; Tu, J. (2016). Conversion from Li_2SO_4 to Li_2S@C on Carbon Paper Matrix: A Novel Integrated Cathode for Lithium-sulfur Batteries. Journal of Power Sources. 331, 475-480.

39 Liu, J.; Nara, H.; Yokoshima, T.; Momma, T.; Osaka, T. (2015). Micro-scale Li_2S-C composite preparation from Li_2SO_4 for Cathode of Lithium Ion Battery. Electrochimica Acta. 183, 70-77.

40 Lv, D.; Zheng, J.; Li, Q.; Xie, X.; Ferrara, S.; Nie, Z.; Mehdi, L. B.; Browning, N. D.; Zhang, J.; Graff, G. L.; Liu, J.; Xiao, J. (2015). High Energy Density Lithium–Sulfur Batteries: Challenges of Thick Sulfur Cathodes. Adv. Energy Mater. 5, 1402290. DOI: 10.1002/aenm.201402290.

41 Yang, Y.; Zheng, G.; Misra, S.; Nelson, J.; Toney, M. F.; Cui, Y. (2012). High-Capacity Micrometer-Sized Li_2S Particles as Cathode Materials for Advanced Rechargeable Lithium-Ion Batteries. J. Am. Chem. Soc. 134, 15387-15394.

42 Vizintin, A.; Chabanne, L.; Tchernychova, E.; Arcon, I.; Stievano, L.; Aquilanti, G.; Antonietti, M.; Fellinger, T.; Dominko, R. (2017). The Mechanism of Li_2S Activation in Lithium-Sulfur Batteries: Can we avoid the polysulfide formation? Journal of Power Sources, 344, 208-217.

43 Jung, Y.; Kang, B. (2016). Understanding Abnormal Potential Behaviors at the 1st Charge in Li_2S Cathode Material for Rechargeable Li-S Batteries. Phys. Chem. Chem. Phys., 18, 21500.

44 Su, H.; Fu, C.; Zhao, Y.; Long, D.; Ling, L.; Wong, M. B.; Lu, J.; Guo, J. (2017). Polycation Binders: An Effective Approach toward Lithium Polysulfide Sequestration in Li-S Batteries. ACS Energy Lett. 2, 2591-2597.

Chapter 3: Pre-lithiation of Lithium-ion Batteries

3.1 Concept and Motivation of Pre-lithiation Technology for Lithium Batteries

To meet the power and energy requirements for plug-in hybrid vehicles with 40-mile range (PHEVs-40) and all-electric vehicles (EVs), there is a need for high energy density chemistry offering more than 200 Wh/kg at the pack level, corresponding to 300 - 350wh/kg at the cell level. [1-3] The state-of-the-art battery technology cannot meet the energy density required for the electric vehicle market.

Owing to its exceptionally high specific capacity, silicon anode is a promising up-and-coming candidate for the next generation of energy high-energy-density lithium-ion batteries (LIBs). [4-6] Although tremendous efforts were devoted to developing Si (silicon) anode, the practical application of the silicon anode is still hindered mainly by numerous issues such as fast capacity fading and significant volumetric expansion. [7-8]

One of the significant problems of silicon anode is its large first-cycle irreversibility, leading to a substantial loss of recyclable lithium originating from the metal oxide cathode materials in a full cell.[9-10] Silicon (Si) suffers from high 1st cycle active lithium losses caused by solid electrolyte interphase (SEI) formation, which in turn hinder their broad commercial use so far. In general, the loss of active lithium permanently decreases the available energy by consuming cyclable lithium from the positive electrode material.

Pre-lithiation is considered a highly appealing technique to compensate for active lithium losses and increase practical energy density. Various pre-lithiation techniques have been evaluated so far. In most cases, pre-lithiation compensates for the 1st cycle active lithium loss, attributed mainly to SEI formation. This increases the remaining amount of

active/cyclable lithium inside the cell during continuous charge/discharge cycling, increasing reversible capacity and increasing energy density.

Furthermore, it is believed that pre-lithiation of Si-based anodes can lead to a pre-volume expansion, which decreases the relative volume change of Si during cycling, causing a reduced cracking and pulverization of Si and may enhance the mechanical electrode stability. In addition, pre-lithiation of Si causes a decrease in the elastic and shear moduli and an increase in the diffusion coefficient of lithium, reducing the stress in comparison to pristine Si and leading to an improved cycle performance. [11]

An in-depth study will be conducted about the realization of lithium oxide and lithium peroxide (Li_2O/Li_2O_2) as low-cost and low-weight lithium sources. Researchers had demonstrated that lithium oxide could be electrochemically activated in LIBs when lithium oxide was mixed with a high voltage metal oxide material such as Li_2MnO_3-$LiMO_2$ (M=Mn, Ni, Co) to form a composite cathode. The activated lithium oxide worked as a lithium source to compensate for the first-cycle irreversibility. [12-13] Yet, using Li_2O/Li_2O_2 as lithium sources still encounters several technical problems, such as the stability of Li_2O and the low activation rate of commercial Li_2O powder. Therefore, a comprehensive investigation of the activation mechanism of Li_2O/Li_2O_2 and NMC composite cathode has been carried out.

Reference

1 Kempton, W., Electric vehicles: Driving range. *Nature Energy* **2016**, *1*, 16131.

2 Nitta, N.; Wu, F.; Lee, J. T.; Yushin, G. Li-Ion Battery Materials: Present and Future. *Mater. Today* **2015**, *18* (5), 252.

3 Thackeray, M. M.; Wolverton, C.; Isaacs, E. D. Electrical Energy Storage for Transportation—Approaching the Limits of, and Going Beyond, Lithium-Ion Batteries. *Ener. Environ. Sci.* **2012**, 5 (7), 7854.

4 Feng, K.; Li, M.; Liu, W.; Kashkooli, A. G.; Xiao, X.; Cai, M.; Chen, Z., Silicon-Based Anodes for Lithium-Ion Batteries: From Fundamentals to Practical Applications. *Small* **2018**, *14*, 1702737.

5 Jin, Y.; Kneusels, N. H.; Marbella, L. E.; Castillo-Martinez, E.; Magusin, P.; Weatherup, R. S.; Jonsson, E.; Liu, T.; Paul, S.; Grey, C. P., Understanding Fluoroethylene Carbonate and Vinylene Carbonate Based Electrolytes for Si Anodes in Lithium Ion Batteries with NMR Spectroscopy. *Journal of the American Chemical Society* **2018**, *140*, 9854.

6 Liu, Z.; Yu, Q.; Zhao, Y.; He, R.; Xu, M.; Feng, S.; Li, S.; Zhou, L.; Mai, L., Silicon oxides: a promising family of anode materials for lithium-ion batteries. *Chemical Society reviews* **2019**, *48*, 285.

7 Xu, Z.; Yang, J.; Li, H.; Nuli, Y.; Wang, J., Electrolytes for advanced lithium ion batteries using silicon-based anodes. *Journal of Materials Chemistry A* **2019**, *7*, 9432.

8 Schiele, A.; Breitung, B.; Hatsukade, T.; Berkes, B. B.; Hartmann, P.; Janek, J.; Brezesinski, T., The Critical Role of Fluoroethylene Carbonate in the Gassing of Silicon Anodes for Lithium-Ion Batteries. *ACS Energy Letters* **2017**, *2*, 2228.

9 Zuo, X.; Zhu, J.; Müller-Buschbaum, P.; Cheng, Y.-J., Silicon based lithium-ion battery anodes: A chronicle perspective review. *Nano Energy* **2017**, *31*, 113.

10 Franco Gonzalez, A.; Yang, N.-H.; Liu, R.-S., Silicon Anode Design for Lithium-Ion Batteries: Progress and Perspectives. *The Journal of Physical Chemistry C* **2017**, *121*, 27775.

11 Holtstiege, F., Bärmann, P., Nölle, R., Winter, M. and Placke, T., 2018. Pre-lithiation strategies for rechargeable energy storage technologies: Concepts, promises and challenges. *Batteries*, 4(1), p.4.

12 Abouimrane, A.; Cui, Y.; Chen, Z.; Belharouak, I.; Yahia, H. B.; Wu, H.; Assary, R.; Curtiss, L. A.; Amine, K., Enabling high energy density Li-ion batteries through Li_2O activation. *Nano Energy* **2016**, *27*, 196.

13 Sun, Y.; Lee, H.-W.; Seh, Z. W.; Liu, N.; Sun, J.; Li, Y.; Cui, Y., High-capacity battery cathode prelithiation to offset initial lithium loss. *Nature Energy* **2016**, *1*, 15008.

14 Amanchukwu, Chibueze V., Jonathon R. Harding, Yang Shao-Horn, and Paula T. Hammond. "Understanding the chemical stability of polymers for lithium–air batteries." *Chemistry of Materials* 27, no. 2, **2015**: 550-561.

3.2 Pre-lithiation Based on Oxygen Chemistry

The primary approach is to design a suitable Li-ion battery system by exploring the different combination of cell components to enable Li_2O/Li_2O_2 pre-lithiation of Li-ion batteries. Essential cell components are summarized as the cathode (NMC622, FCG775), cathode additives (Li_2O and Li_2O_2), electrolyte (GENII, 1.2 M $LiPF_6$ in EC/EMC), and electrolyte additives (FEC). Detailed cell components are summarized in the following materials list.

Table 3. Materials list.

Component	Supplier	Type/Grade
Anode 1: High Si-content anode, ~ 2 mg Si/cm2	Wacker	CLM 00001, 70 wt% Si, 20 wt% C45, 2 wt% C45 in NaCMC, 8 wt% Li-PAA
Anode 2: LTO, 1.96 mAh/cm2	Argonne National Laboratory, Cell Analysis, Modeling, and Prototyping (CAMP) Facility	A-A014, Samsung Fine Chemicals, 87 wt% LTO, 5 wt% C45, 8 wt% kureha 9300
Anode 3: Graphite, 1.87 mAh/cm2	CAMP	A-A015, Superior Graphite SLC1506T, 91.85 wt% graphite, 2 wt% C45, 6 wt% kureha 9300, 0.17 wt% oxalic Acid
Conductive carbon black	TIMCAL	Super C65
PAA-Binder, powder	Polysciences, Inc.	MW ~450, 000
NaCMC, powder	Sigma Aldrich	Sodium carboxymethyl cellulose, average Mw ~250,000, degree of substitution 1.2
LiOH	Sigma Aldrich	Lithium hydroxide
Cathode 1: FCG775, ~2.3 mAh/cm2	Argonne National Laboratory (ANL)	The full concentration-gradient layered oxide cathode active material, LiNi0.775Co0.125Mn0.1O2
Cathode 2: NMC622, 1.53 mAh/cm2	CAMP	A-C023, Targray, Prod: SNMC03006, Lot#: LT-170861432, 90 wt% NMC622, 5 wt% C45, 5 wt% Solvey® 5130
PVDF binder	SOLVAY	Solvey® 5130, 8 wt% in NMP
Copper foil	CAMP	10 μm
Aluminum foil	CAMP	20 μm
Electrolyte: GENII	Tomiyama Pure Chemical Industries, LTD	LIPASTE, 1.2 M LiPF6; EC:EMC 3:7 (w:w)
Electrolyte additive: FEC	ANL	Distilled
Li_2O_2	Acros	Particle size < 1 μm
Li_2O	Sigma Aldrich	Particle size < 3 μm after 20 mins ball-milling

Slurry preparation: To avoid material agglomeration and aggregation caused by heat generation during mixing, small amount of materials (with total weight 3 to 5 grams) were mixed in each batch with THINKY non-vacuum mixer ARE-310. Pure NMC cathode laminate comprises 90 wt% FCG775, 5 wt% C65 conductive carbon, and 5 wt% PVDF (which is composed of 8 wt% PVDF in NMP). A typical batch of cathode slurry consisting of 1.8 g FCG775, 0.1 g C65, 1.25 g PVDF (8 wt% in NMP), and 1.5 g NMP. The total solid content of the final slurry amounts is 43% (determined by calculation).

For anode slurry preparation, pure silicon-based anode laminate comprises 70 wt% Wacker silicon, 20 wt% C65, and 10 wt% polymer binder. pH values above pH = 7.0 was avoided. In addition, the temperature was controlled under 45° C during slurry preparation. First, NaCMC-C65 conductive additive dispersion was prepared by mixing 20.0 g of aqueous NaCMC (0.87 wt.%) and 1.75 g of conductive additive C65 for 45 min using an ultrasonic probe with an ice bath. 13.97g of aqueous Li-PAA binder solution (20 wt.%) was further neutralized with LiOH to pH 7.0 for future use. The resulting Li-PAA was 12 wt%. 2.30 g of 8.7 wt% conductive additive dispersion and 1.4 g of Wacker silicon are pre-mixed in a centrifugal mixer. Subsequently, 0.2 g of C65 and Li-PAA binder were added and mixed, and degassed for 20 min in total in a centrifugal mixer. The total solid content of the final slurry amounts to 40%.

The cathode and anode slurry was coated on aluminum and copper foil respectively at room temperature using a film applicator for film casting and electrode drying. Subsequently, the film was pre-dried on the applicator plate at room temperature. The electrode coating is further dried for at least 10 hrs at 100° C in a vacuum oven.

Spread coating: The spread coating was carried out in an Ar-filled glovebox. 0.1 g Li_2O_2 was first dispersed in 9.9 g anhydrous dimethyl carbonate (DMC). The specific amount of suspension was dropped on the FCG775/NMC622 laminate and put on the hotplate to evaporate DMC at 80 ° C for 5 min.

Coating weight: The area loading of NMC is controlled to 6-15 mg cm^{-2} (~1 to 2.5 mAh cm^{-2}). The target value for the coating weight amounts of the anode is 2.8 mg/cm^2 (~2.3 mAh cm^{-2}). The target value of Li_2O_2 is determined by measuring the weight of the electrode before and after coating.

Electrochemical characterization: The cell format included 1.54 (cathode) to1.767 (anode) cm^2 coin cell and 3 cm * 4.5 cm single-layer pouch-cell. Celgard® 2325 was used as the separator. Different cells containing different cell components formed and cycled at different windows, which will be mentioned in the main content.

Other characterization methods: Differential electrochemical mass spectrometry (DEMS) is a technique that can be used to study the chemical reactions that occur at the electrodes mechanistically. Using DEMS, volatile chemical species generated at the electrodes can be detected with minimal time delay. The target gas of this project is O_2 at this moment. UV-Vis is used to test the compatibility of Li_2O_2 and PVDF/NMP solutions.

Compatibility: The compatibility of Li_2O_2/Li_2O has been thoroughly investigated and discussed in previous years. Apart from the compatibility between Li_2O_2/Li_2O and the electrolyte, their relativities towards cathode slurry solution are also worth investigating. Though Li_2O_2 and Li_2O are good candidates for pre-lithiation because of their high

volumetric and gravimetric capabilities, they are inherently incompatible with the laminate-making process due to the reaction with NMP (N-methyl-2-pyrrolidone) or water in NMP. Essentially, the amount of Li_2O_2/Li_2O in the cathode need to be quantified, and the loss of Li_2O_2/Li_2O should be minimized during the cathode laminate preparation process. In particular, Li2O and Li2O2 behave differently in preparing the electrode slurry for lamination. Owing to the high basicity and hygroscopic nature of Li2O, it can react with water very quickly to form a significant amount of lithium hydroxide, initiating the gelation of the slurry during mixing. Since bench-top NMP usually has high water content, the gelation process is highly common for Li2O added slurry. Meanwhile, the reactivity of Li2O2 towards cathode slurry solution is even more complicated because it may not be stable with neither NMP nor PVDF

Therefore, this year we further designed experiments to understand the compatibility between pre-lithiation materials and the standard cathode slurry components, including PVDF (polyvinylidene fluoride) and slurry solvents.

Evaluate the stability of Li_2O_2 in the cathode slurry solution: The chemical stability of polymers for batteries containing Li_2O_2 has been studied in the topic of Li-Air batteries.[14] **Figure 14** shows the chemical stability of Li_2O_2 in cathode slurry solutions. **Figure 14 (a)** is the chemical stability of Li_2O_2 towards different polymers for cathode slurry solutions. **Figure 14 (b)** is UV-Vis results of Li_2O_2 and PVDF in dimethylacetamide over time, and **Figure 14 (c)** is the FTIR result of PVDF in dimethylacetamide with and without Li_2O_2. Li_2O_2 towards PVDF/dimethylacetamide slurry solution is not stable.

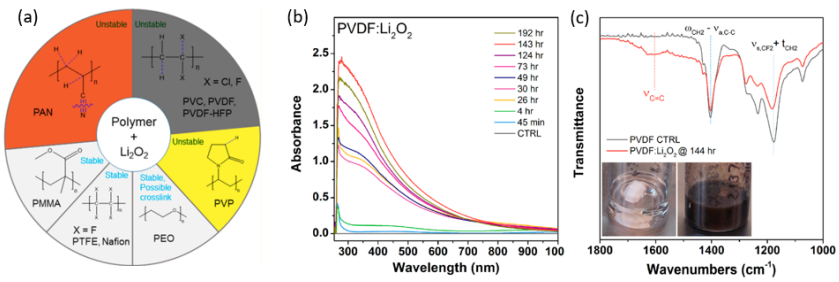

Figure 14. Chemical stability of Li2O2 in cathode slurry solutions: (a) chemical stability of Li2O2 towards different polymers for cathode slurry solutions, (b) UV-Vis results of Li2O2 and PVDF in dimethylacetamide over time, and (c) FTIR result of PVDF in dimethylacetamide with and without Li_2O_2.

However, we re-exam the chemical stability of Li_2O_2 in cathode laminate because its stability in PVDF/NMP binder solution, especially its stability towards NMP, is unknown. More importantly, essential data, including NMR was missing in reference.

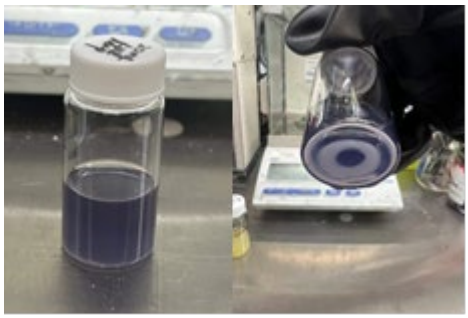

Figure 15. Optical images of 20 mg Li2O2 in 10 mg NMP solvent, which represent the chemical stability of Li2O2 in cathode slurry solvent.

Figure 15 is the optical images of 20 mg Li_2O_2 in 10 mg NMP solvent, which represent the chemical stability of Li_2O_2 in cathode slurry solvent. By observing the color change of NMP, we can conclude that NMP is not chemically compatible with Li_2O_2.

The chemical compatibility of PVDF and Li_2O_2 in NMP is further examined by characterizing the supernatant of Li_2O_2 reacting with PVDF/NMP solutions. **Figure 16 (a)** is the optical images of 50 mg Li_2O_2 and 100 mg PVDF Solve® 5130 dissolved in 10 ml

NMP solvent, which shows dark brown color after the reaction. **Figure 16 (b)** is the UV-Vis result of PVDF in NMP, Li_2O_2 in NMP, and Li_2O_2 in PVDF/NMP.

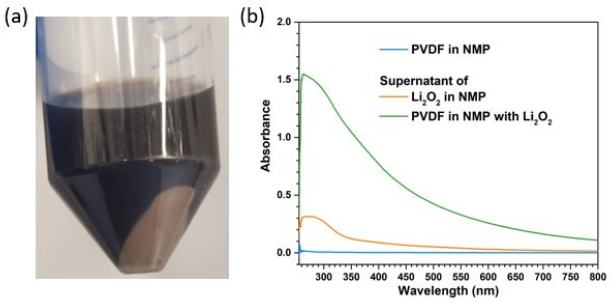

Figure 16. (a) Optical images of 50 mg Li2O2 and 100 mg PVDF Solve® 5130 dissolved in 10 ml NMP solvent, (b) UV-Vis result of PVDF in NMP, Li2O2 in NMP, and Li2O2 in PVDF/NMP, which represent the chemical stability of Li2O2 in cathode binder solution.

UV−vis spectroscopy was used to track changes in color and formation of possible π-conjugated species. Baseline is pure NMP, and it is clear that both NMP and PVDF does react with Li_2O_2.

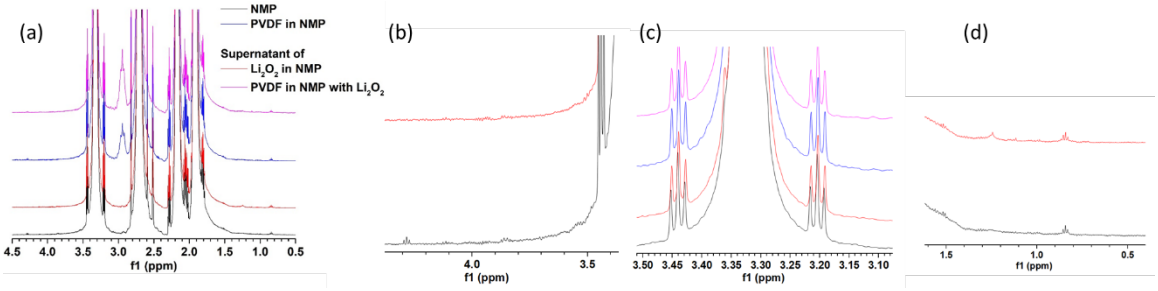

Figure 17. 1H-NMR spectra of NMP, PVDF in NMP, Li2O2 in NMP, and Li2O2 in PVDF/NMP.

^{1}H-NMR is used to further verify the compatibility of Li_2O_2 in PVDF/NMP, shown as **Figure 17**. Pure NMP and PVDF in NMP are controls, and clear changes are detected after adding Li_2O_2. Therefore, Li_2O_2 is considered unstable towards PVDF/NMP.

However, Li_2O_2 may still be able to serve as a cathode additive, if the only small amount was reacted during the cathode laminate make process. Therefore, we further quantify the reaction amount by using the $TiOSO_4$ UV-Vis titration method. The mechanism is shown in **Figure 18**.

Titanium(IV) oxysulfate ($TiOSO_4$) is known to form a yellow complex upon reaction with hydrogen peroxide (H_2O_2), which facilitates the determination of Li_2O_2. Cathode laminate made from directly mixing Li_2O_2 into slurry was titrated to determine the amount of Li_2O_2.

$$Li_2O + H_2O \rightarrow 2LiOH$$

$$* \quad Li_2O_2 + 2H_2O \rightarrow 2LiOH + H_2O_2$$

$$4LiO_2 + 2H_2O \rightarrow 4LiOH + 3O_2$$

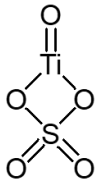

Figure 18. Possible reactions of lithium peroxide in the TiOSO4 titration experiment.

Figure 19 is the change of color in $TiOSO_4$ solution. They are pure $TiOSO_4$ solution, $TiOSO_4$ reacts with Li_2O_2, $TiOSO_4$ reacts with Li_2O_2 and Al current collector, and $TiOSO_4$ react with Li_2O_2 and FCG775 cathode laminate. Though color degradation exists because of Al and NMC cathode, the whole process is very slow, and takes up to an hour, comparing to the reaction of Li_2O_2 with $TiOSO_4$. The further quantification process was conduct by testing samples immediately after adding $TiOSO_4$ to avoid the influence from Al current collector and NMC cathode material.

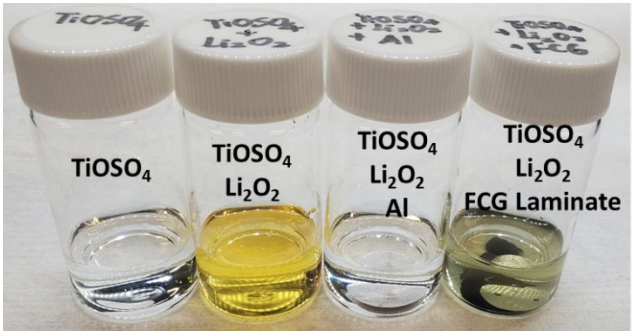

Figure 19. Optical images of TiOSO4 solution, TiOSO4 react with Li2O2, TiOSO4 react with Li2O2 and Al current collector, and TiOSO4 react with Li2O2 and FCG775 cathode laminate.

Figure 20 is the UV-Vis absorbance spectra of Li_2O_2 reacting with $TiOSO_4$ and the standard curve of Li_2O_2 reacting with $TiOSO_4$ to quantify the Li_2O_2 amount. The amount of Li_2O_2 left after the laminate-making process is summarized in **Table 4**.

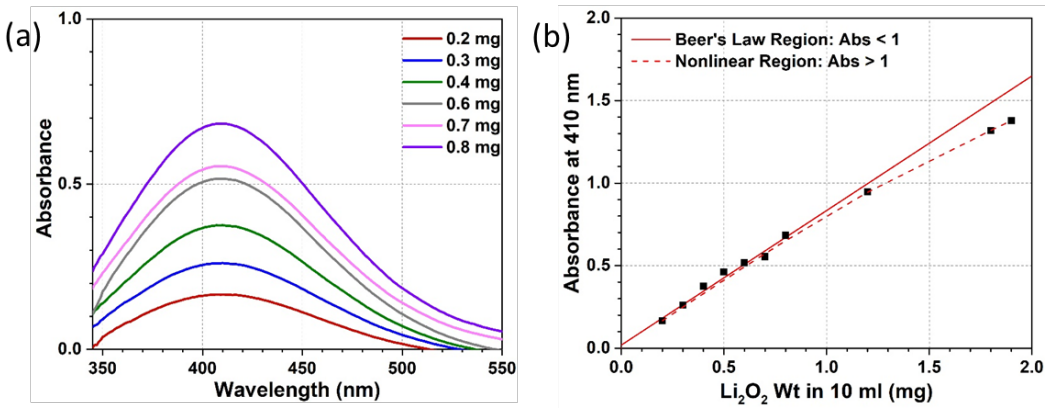

Figure 20. (a) UV-Vis absorbance spectra of Li2O2 reacting with TiOSO4; (b) the fitted standard curve to quantify the Li2O2 amount.

The Li_2O_2 was directly mixed into cathode slurry and made into cathode laminate. As summarized in **Table 4**, nearly half of the Li_2O_2 was reacted if it was directly mixed into cathode slurry. It also tells $TiOSO_4$ titration is a very precise method to determine the amount of Li_2O_2 which can be used in future study.

Table 4. TiOSO4 titration result of FCG775 laminate containing Li2O2.

Sample	Abs	Li_2O_2 Added mg	Li_2O_2 Non-reacted mg	Li_2O_2 reacted during making slurry
FCG775	0	-	-	-
FCG775 + 5% Li_2O_2	0.2742	0.54	0.313	42%
FCG775 + 7.5% Li_2O_2	0.5853	1.133	0.695	39%
FCG775 + 15% Li_2O_2	0.8292	1.875	0.995	47%

To minimize the loss of Li_2O_2 during slurry making process, it is necessary to find other solvents or cathode laminate making process for Li_2O_2.

Examine the reactivity of Li_2O_2 in commonly used organic solvents for cathode slurry: DMC, DMSO, TEP, TMP, Cyrene: It is believed that, once PVDF is dissolved, reactions between Li_2O_2 and PVDF start. Since the laminate needs to go through heating and drying for hours, these reactions are inevitable. But we can minimize the reaction by using non-PVDF dissolving or less-PVDF dissolving solvents, other than NMP, to spread coat Li_2O_2 on cathode laminate. These solvents include DMC, DMSO, TEP, Cyrene, and TMP. Lab-scale spread coating was first introduced by using DMC, which does not dissolve PVDF.

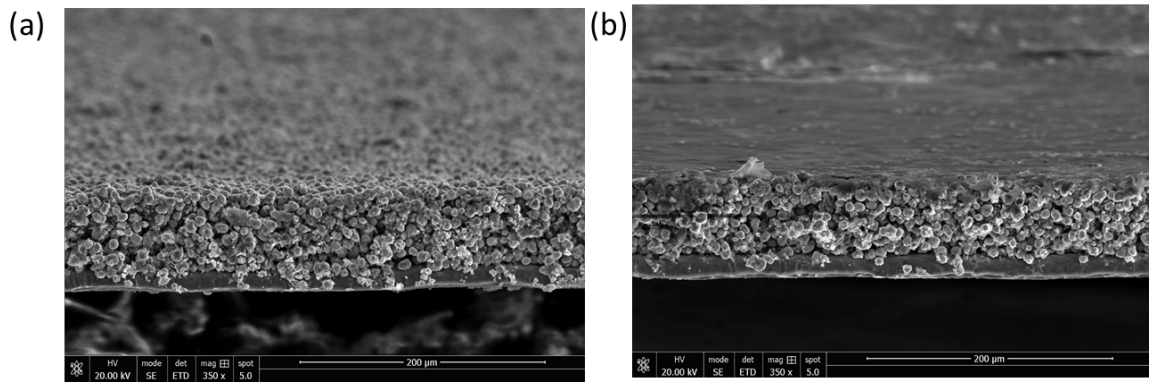

Figure 21. Cross-sectional SEM images of (a) FCG775 cathode laminate, and (b) 0.25 mg cm-2 Li2O2 mixed with carbon coated on cathode laminate.

As depicted in **Figure 21**, a uniform and dense coating layer could be achieved by mixing C65 and Li_2O_2 with in DMC and then coated on FCG775 cathode.

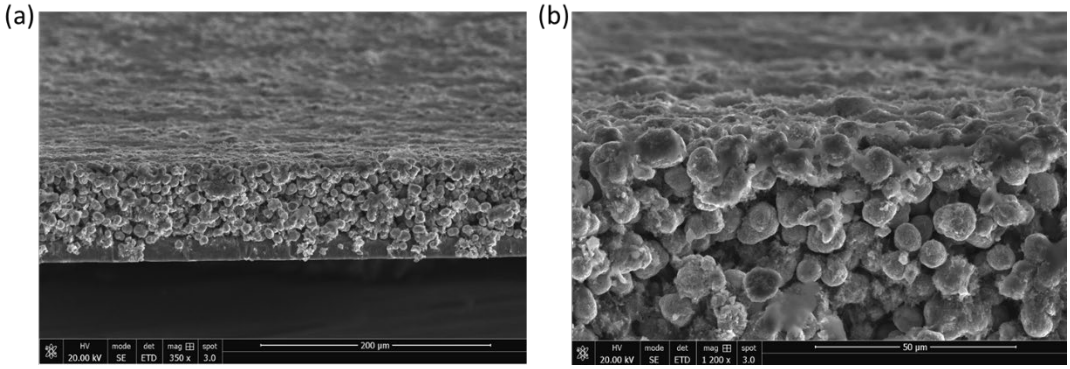

Figure 22. Cross-sectional SEM images of (a) pure 0.25 mg cm-2 Li2O2 coating on cathode laminate and (b) the zoom-in image of cathode laminate surface.

As shown in **Figure 22**, pure Li_2O_2 coating layer is thinner but sparse. Both laminate with and without carbon were later served as cathode to study the activation of Li_2O_2. However, considering we need to further quantify the activation amount of Li_2O_2 by other characterization methods such as ICP-OES, therefore, the cathode laminate coating layer needs to be sticky to the cathode laminate. Therefore, other solvents with slight PVDF solubility were screened for making Li_2O_2 coating layer.

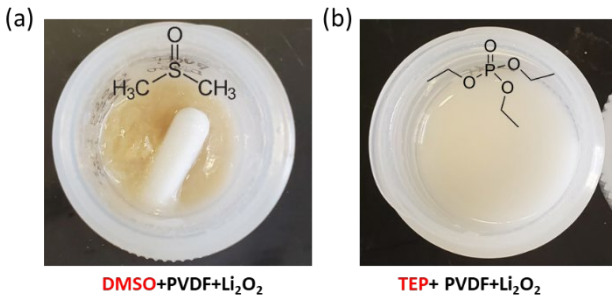

Figure 23. Compatibility of Lithium Peroxide (Li2O2) and Binder Solution.

Li_2O_2 is known to be reactive towards binder solvent, NMP. Therefore, other solvents are evaluated. Gelation is observed when mixing Li_2O_2 with DMSO. TEP is a solvent suitable for both Li_2O_2 and PVDF. But TEP has very high evaporation temperatures thus pre-longed the drying process.

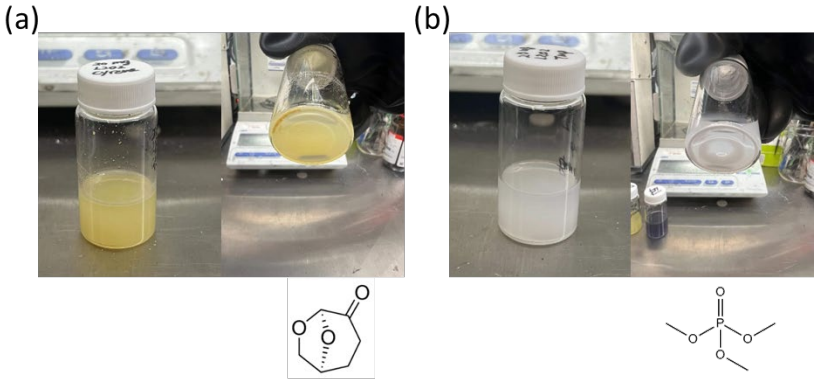

Figure 24. Future direction of compatibility of lithium peroxide and binder solvent (a) Cyrene and (b) TMP.

Cyrene and TMP are potentially suitable solvents for both Li_2O_2 and PVDF, which are currently under investigation.

Activation: Yet, the low activation rate of commercial Li_2O/Li_2O_2 still hinders their application. Therefore, Argonne has been carrying out a comprehensive investigation about the activation mechanism of Li_2O_2/Li_2O and NMC composite cathode. Moreover, Argonne

has also been optimizing the condition for the activation reaction of Li_2O_2/Li_2O in order to deliver a prototype cell with enhanced energy density.

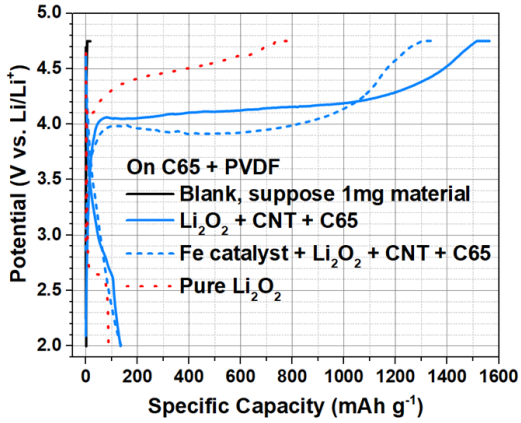

Figure 25. Activation of lithium peroxide with different carbon and catalyst additives by spread coating on blank cathode (containing C65 and PVDF).

Explore potential catalyst and carbonaceous material additives to reduce the onset voltage for Li_2O/Li_2O_2 activation: Figure 25 is the activation curve of lithium peroxide with different carbon and catalyst additives by spread coating on blank cathode (containing C65 and PVDF). Each electrode contains around 0.2-0.3 mg Li2O2 cm-2, and the cells are activated with current of 0.02 mA cm^{-2} at 25 °C. It is clear that, SWNT and Fe nanoparticles lower the overpotential required to electrochemically decompose Li_2O_2, and Li_2O_2 is only activated at the first cycle.

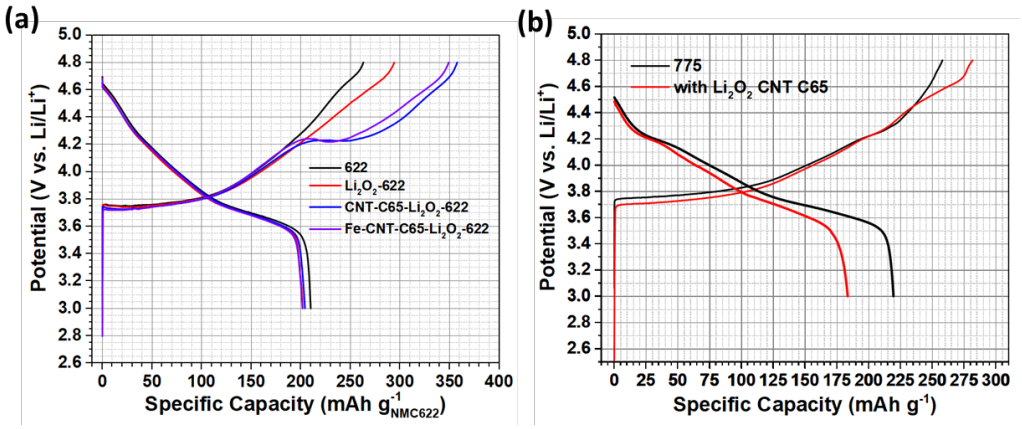

Figure 26. Charge profiles of (a) Li/NMC622-Li2O2 with different additives (b) Li/FCG775-Li2O2 with carbon additives.

Investigate the effect of NMC materials on the activation of Li_2O/Li_2O_2: Apparently, the type of NMC material impact the activation of Li_2O_2. **Figure 26** is the activation curve of **(a)** Li/NMC622-Li_2O_2 with different additives. **Figure 26 (b)** is Li/FCG775-Li_2O_2 with carbon additives. Activation of Li_2O_2 peaked at 4.25 V vs. Li for NMC622. The difference of activation rate is most likely arising from the type of NMC cathode, which is summarized in **Table 5**.

Table 5. TiOSO4 titration result of FCG775 laminate containing Li2O2.

	Activation based on increased charge capacity	Activation rate
622-Li2O2	(294-263)*14.6754/0.35/1168	111.3%
622-CNT-Li2O2	(357-263)*15.4044/1.3704/1168	90.5%
622-Fe-CNT-Li2O2	(349-263)*15.2964/1.235/1168	91.2%
FCG775-CNT-Li2O2	(281-257)*8.1864/0.31/1168	54.3%

As shown in **Table 5**, CNT improved battery performance. Adding Fe nanoparticles did not show distinct difference. Activation of Li_2O_2 has less interference with NMC622 comparing to FCG775. We believe it is because of the gassing of NMC cathode itself, which needs to be further verified with other characterizations shown in the gassing section.

Gassing: Gassing is commonly known as an issue for Li-ion batteries that utilize Si as anode, but the causes are still debatable in academia. Adding Li_2O/Li_2O_2 into a battery further complicates the system, because, apart from common cell components, Li_2O/Li_2O_2 also generate extra gases (and O_2 should be dominate). Therefore, study the impact of gases (O_2) evolution on battery cell performance is another key of this project.

Electrolyte components: Firstly, we will discuss cell components that generate gases. FEC, which is a common electrolyte additive for Li-ion batteries using Si anode, actually generates gases.

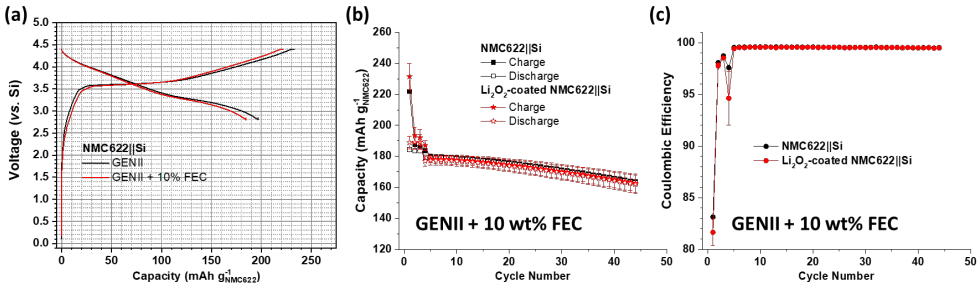

Figure 27. Charge-discharge profiles of (a) Si/NMC622 using electrolyte with and without FEC additive; (b) cycling performance and (c) columbic efficiency comparison of Si/NMC622 and Si/NMC622-Li2O2 using electrolyte containing FEC.

Figure 27 is the charge-discharge profiles of (a) Si/NMC622 using electrolyte with and without FEC additive. Adding FEC does not help to improve the Coulombic efficiency. Moreover, it actually worsens the charge-discharge capacity. On one hand, it is because

FEC is believed to passivate the Si anode, improving the capacity retention in long term cycling. On the other hand, FEC is speculated to generate gases, which are harmful to the cell. As a result, in **Figure 27 (b),** the cycling performance and **(c)** Columbic efficiency, of the cell adding Li_2O_2 do not show any improvement.

To further verify this, FEC is removed from electrolyte. **Figure 28 (a)** is the cycling performance and **(b)** is the Columbic efficiency comparison of Si/NMC622 and Si/NMC622-Li_2O_2 using GENII electrolyte. Adding Li_2O_2 successfully improved cyclable lithium, capacity retention, and columbic efficiency.

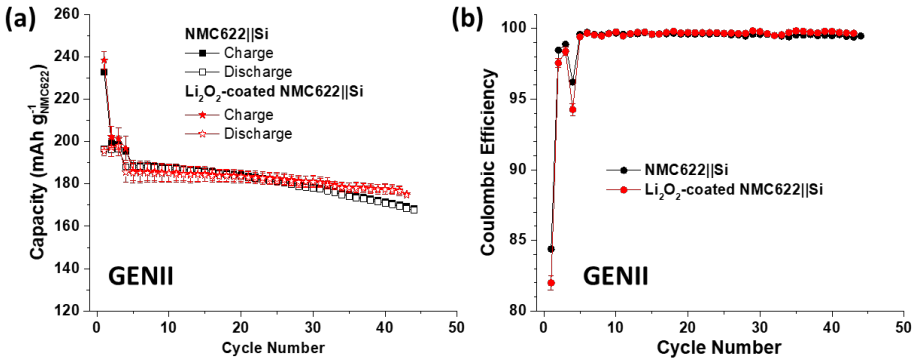

Figure 28. (a) cycling performance and (b) columbic efficiency comparison of Si/NMC622 and Si/NMC622-Li2O2 using GENII electrolyte.

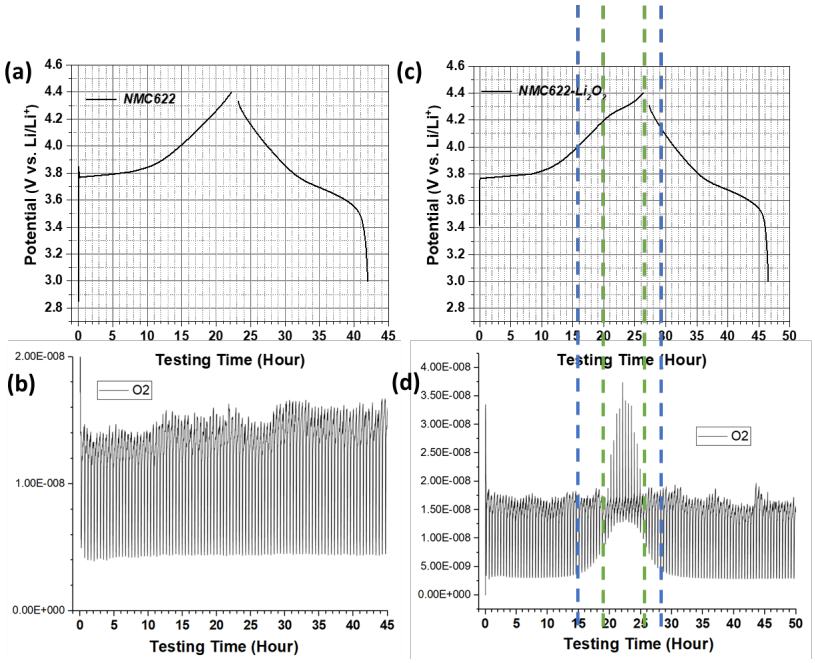

Figure 29. DEMS result of NMC622 electrode (a) and (b) without Li2O2, and (c) and (d) with Li2O2.

NMC cathode materials with high Ni content and Li_2O_2: Apart from the electrolyte decomposition, cathode materials also generate gases. DEMS was used to verify the gas evolution potential of NMC622, FCG775, and Li_2O_2. Each DEMS cell contains 100 µl electrolyte (GENII with 10wt% FEC), and the cycling rate is C/20. Every 0.5 hour, MS samples a point to record the gas evaluated in the past 0.5 hours. It is clear that for NMC622 cathode, no O_2 was evolved under 4.4V vs. Li. After adding Li_2O_2, O_2 evolution started at 4.0V and peaked at 4.3V, as shown in **Figure 29**.

In **Figure 30**, we learnt that FCG775 actually generated gases earlier than NMC622, and this could delay the activation of Li_2O_2 either by increasing the intrinsic resistance in the cell, or by introducing O anion redox, which will be investigated in the future.

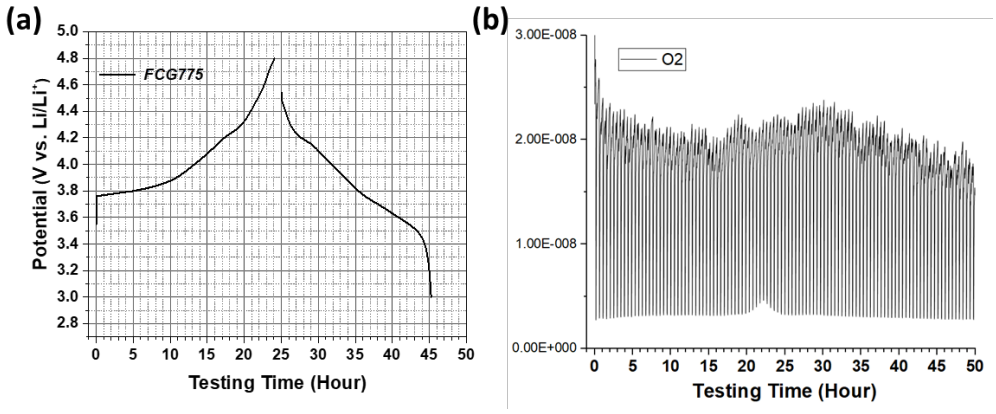

Figure 30. DEMS result of FCG775 electrode.

Cell-to-cell variation: However, many issues also come with cell gassing. We will discuss them one-by-one. The first problem is cell-to-cell variation and cell inconsistency.

Figure 31. Optical images of a NMC622||LTO pouch cell.

To maximize the impact of gasses, pouch cell was assembled with gassing electrolyte, GENII with 10 wt% FEC. The anode is LTO (CAMP AA014) and cathode is NMC622 (CAMP AC023). All cells are tested with the following procedure: charge at 0.05 C, then do CV charge until 0.01C, followed by 0.05 C discharge, and rest for 10 seconds. Cathode loading is 1.53 mAh/cm^2 NMC622 and is 1.56-1.63 mAh/cm^2 if the cathode contains Li_2O_2. Anode loading is 1.96 mAh/cm^2 LTO. The cut-off voltage window is 1.5 – 2.9 V.

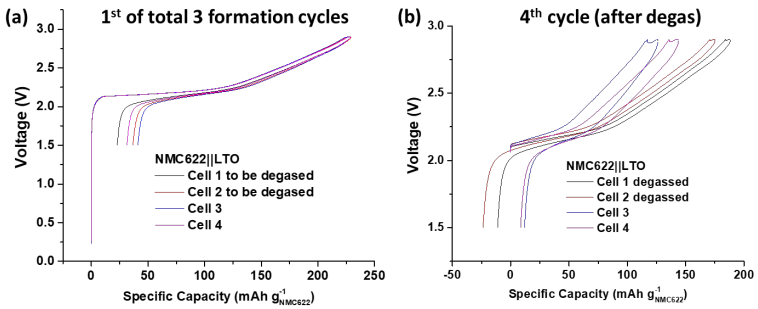

Figure 32. The charge-discharge profile of NMC622||LTO cells with and without degas. Cells 1 and 2 are degassed at the 4th cycle, but Cells 3 and 4 are not. Polarization is observed for Cells without degas.

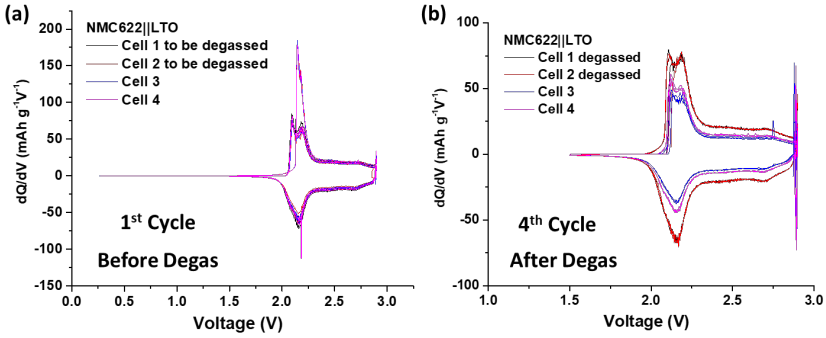

Figure 33. The dQ/dV profile of NMC622||LTO cells with and without degas.

In **Figure 33**, it is also clear that polarization also impact the capacity of cells without degas.

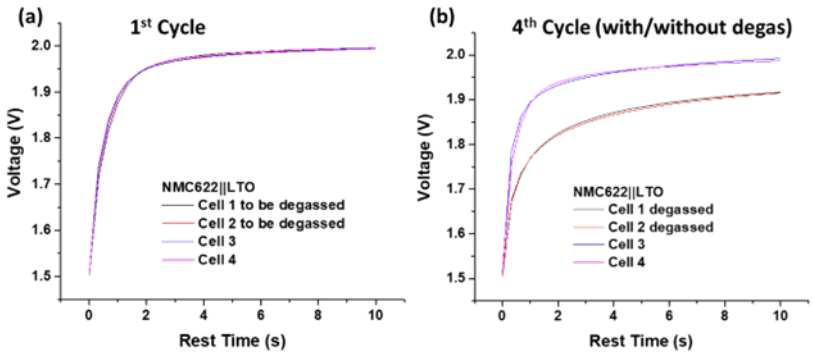

Figure 34. OCV rest after discharge of NMC622||LTO cells with and without degas.

To future enlarge intrinsic resistance difference between cells with and without degas, the IR drop after discharge are plotted. In **Figure 34**, it is clear the polarization could be as large as 200 mV in the cells without degas.

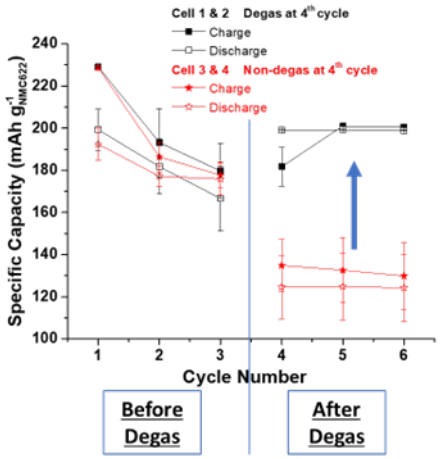

Figure 35. Specific capacity comparison among cells with and without degas.

Figure 35 summarized the specific capacity among cells with and without degas. It is clear that non-degassed cells have lower specific capacity and larger cell-to-cell variations.

Cathode-anode crosstalk: The cathode-anode crosstalk by dioxygen also impacts the full-cell performance. We image potential impacts by switching essential cell components. The comparison is between (NMC622+Li_2O_2+CNT+C65+Fe)||anode and NMC622||anode.

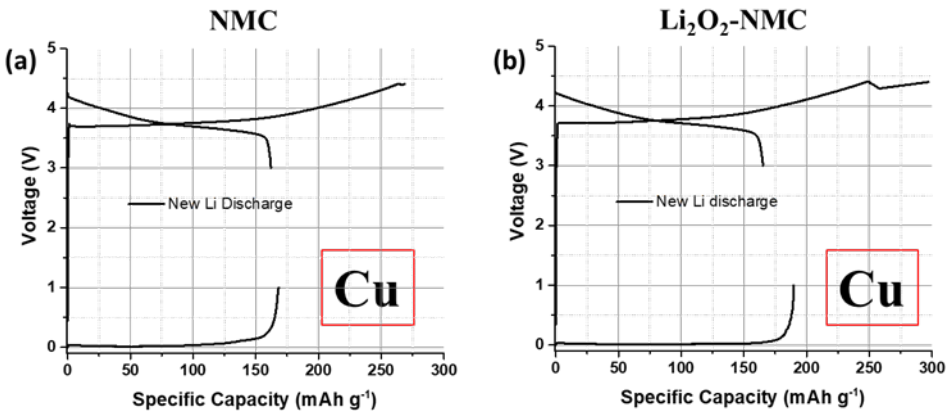

Figure 36. Activation and recover cyclable Li+ comparison between cells with and without Li2O2.

Table 6. Detailed activation rate and recovered cyclable Li+ based on capacity.

	Calculation	Activation rate
Activation based on recovered Li^+	(190-165)*13.599/0.48/1168	14%
Activation based on charge capacity	(297-268)*13.599/0.48/1168	70%

Both the charge capacity and the recovered cyclable Li^+ were increased by adding Li_2O_2. However, the activation rate calculated based on charge capacity is larger than recovered Li+. It is believed to be the oxygen attack on anode, which is also known as cathode-anode cross-talk.

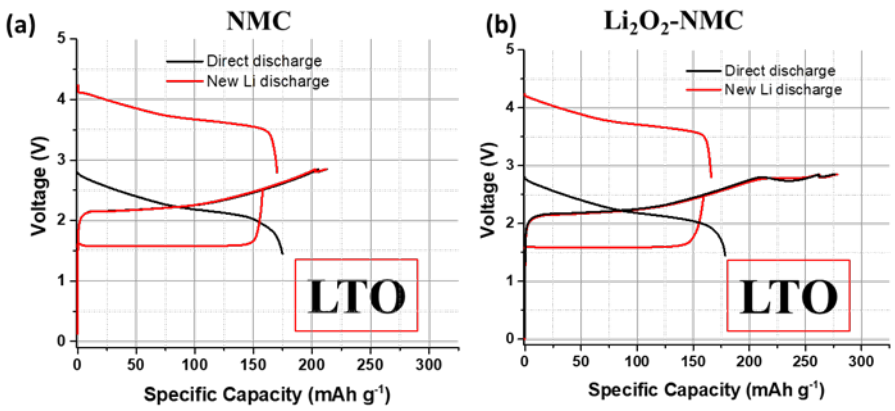

Figure 37. Activation and recover cyclable Li+ comparison between cells with and without Li2O2.

Shown in **Figure 37**, comparison was further done between (NMC622+Li_2O_2+CNT+C65+Fe)||LTO and NMC622||LTO. **Table 7** is the activation rate calculated based on charge capacity and recovered Li^+. It worth noting that LTO anode recovered less Li^+ than Cu, which is speculated to be LTO lacks SEI protection from oxygen attack.

Table 7. Detailed activation rate and recovered cyclable Li+ based on capacity.

	Calculation	Activation rate
Activation based on recovered Li^+	(160-158)*8.361/0.435/1168	4%
Activation based on charge capacity	(279-212)*8.361/0.435/1168	110%

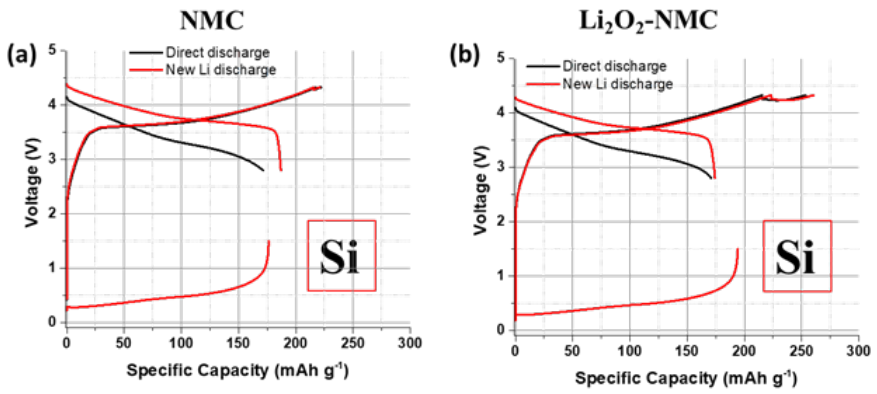

Figure 38. Activation and recover cyclable Li+ comparison between cells with and without Li2O2.

Shown in **Figure 38**, comparison was further done between (NMC622+Li2O2+CNT+C65+Fe)||Si and NMC622||Si. **Table 8** is the activation rate calculated based on charge capacity and recovered Li^+. It worth noting that Si anode recovered the most Li^+ in all anodes, which is speculated to be O_2 gas forms extra SiO_x protection on Si anode by reacting with oxygen gas.

Table 8. Detailed activation rate and recovered cyclable Li+ based on capacity.

	Calculation	Activation rate
Activation based on recovered Li^+	(194-176)*12.68/0.52/1168	38%
Activation based on charge capacity	(265-225)*12.68/0.52/1168	90%

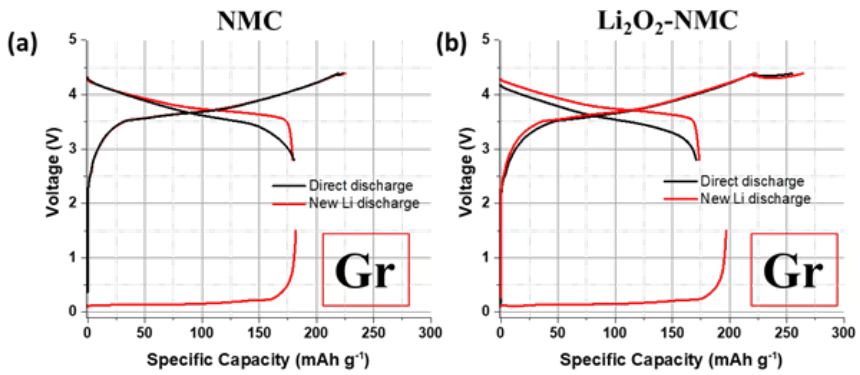

Figure 39. Activation and recover cyclable Li+ comparison between cells with and without Li2O2.

Figure 39 and **Table 9** summarized the comparison between (NMC622+Li2O2+CNT+C65+Fe)||Gr and NMC622||Gr. Similar results were observed as Si anode. It is believed to be the SEI formed on Gr anode.

Table 9. Detailed activation rate and recovered cyclable Li+ based on capacity.

	Calculation	Activation rate
Activation based on recovered Li^+	(197-183)*11.034/0.4/1168	33%
Activation based on charge capacity	(265-225)*11.034/0.4/1168	95%

Lithium plating: The lithium plating phenomenon was also observed in NMC||Si pouch cell, which is an even more severe and unexpected problem that needs to be addressed for real application.

Figure 40. An optical image of lithium plating in NMC||Si pouch cell.

Figure 40 is an optical image of lithium plating in NMC||Si pouch cell. All Li plating spots correspond to the gassing spots on the cathode side in the pouch cell. It is believed that gassing introduced IR change and made Li+ met the Li-platting overpotential, thus Li was plated on Si anode.

3.3 Current and Future of Pre-lithiation Technology

Lastly, we will discuss our potential future directions including deploy diagnostic tools to understand gassing and activation mechanism of Li_2O/Li_2O_2. More importantly, we will assemble cells comprising Li_2O/Li_2O_2–NMC composite cathode and silicon anode to demonstrate the feasibility of the pre-lithiation.

Future research will be focusing on revealing the structural change of NMC materials during the Li2O/Li2O2 activation if any (for NMC622 and FCG775). Moreover, Li_2O will be studied more intensively as the lithium source because it has a significantly higher theoretical capacity. Prototyped full cell with silicon anode and NMC-Li_2O/Li_2O_2 composite cathode using the most stable electrolyte will also be fabricated and studied.

However, it is very important to note that the degree of pre-lithiation has to be adjusted with a high accuracy. Otherwise, an over-lithiation could lead to an excess of lithium, thus lithium metal plating on top of the negative electrodes surface, resulting in safety hazards during operation. Therefore, N/P ratio will be investigated.

Another important issue is the amount of inactive material, which has to be added in order to perform pre-lithiation. In the worst-case scenario, this inactive mass and volume leads to decreased energy densities, which offset the energy density gain attributed to pre-lithiation. In the optimal case, just lithium ions (and electrons) are added during pre-lithiation and other inert weight will be released by gassing. Moreover, in view of maximizing the energy density of LIBs, the maximum positive electrode capacity is limited by the electrode coating thickness and porosity due to kinetic factors, which means the coating thickness will be controlled.

Chapter 4: Lithium Metal and Multivalent Metal Anode Batteries

4.1 Lithium metal batteries

Despite being an excellent candidate for lithium metal batteries due to its stability towards lithium metal, ethereal solvent suffers from relatively low anodic stability, rendering it incompatible with high voltage cathode. Although the anodic stability of ethereal solvent can be enhanced by fluorination, the lithium solvating ability of fluorinated ethers is largely reduced. As a result, common hydrofluoroethers, such as 1,1,2,2-tetrafluoroethyl-2,2,3,3-tetrafluoropropylether (TTE) and bis(2,2,2-trifluoroethyl) ether (BTFE) are not able to dissolve any lithium salt, albeit enhanced oxidation potential. Therefore, new fluorinated glycol ethers were synthesized in this research. The diglyme analogue, which was terminally fluorinated, demonstrated high anodic stability and excellent capability to facilitate lithium plating/stripping. Unlike its non-fluorinated counterpart, the fluorinated diglyme analogue displayed outstanding compatibility with lithium hexafluorophosphate, which is an essential salt in lithium-ion batteries. It was shown that the electrolyte based on fluorinated diglyme analogue with fluoroethylene carbonate as co-solvent enabled highly stable cycling of Li-metal batteries pairing with lithium cobalt oxide cathode.

INTRODUCTION: The key to enabling long-term cycling of lithium (Li) metal batteries is the development of electrolytes that are stable towards both Li anodes and high-voltage cathode materials. Although ethereal solvents with good compatibility towards lithium metal were intensively studied using Li||Li symmetrical cells,[1-3] they were excluded from high-voltage lithium metal batteries due to their limited anodic stability. Also, common ethereal solvents are incompatible with lithium hexafluorophosphate ($LiPF_6$), which is an

essential lithium salt in lithium-ion batteries, due to the acidity of $LiPF_6$ catalyzing polymerization reactions of the ethereal solvents.[4,5] Therefore, sulfonylimide salts such as lithium bis(fluorosulfonyl)imide (LiFSI) or lithium bis(trifluoromethanesulfonyl)imide (LiTFSI) [6] was required to substitute $LiPF_6$ in ethereal electrolytes. However, when sulfonylimide salts are used, aluminum corrosion at a high voltage arises which further narrows the electrochemical window of the electrolytes. [7,8]

To enhance the anodic stability of ethereal solvents, researchers often adjusted the solvation structures of the lithium complexes. For example, high concentration electrolytes are pursued to improve the electro-oxidative stability of ether-based electrolytes by increasing the ratio of the lithium-coordinating solvents, which are more resistive to oxidation due to the positively charged lithium cation. [9,10] Unfortunately, high concentration electrolytes experience many issues such as high viscosity, high cost, low ionic conductivities, and poor reaction kinetics. [11,12] Therefore, localized high concentration electrolyte was introduced by adding diluting solvents, such as 1,1,2,2-tetrafluoroethyl-2,2,3,3-tetrafluoropropylether (TTE) or bis(2,2,2-trifluoroethyl) ether (BTFE), into the high concentration electrolyte.[13-15] These dilutants function as non-solvating co-solvents thinning the electrolytes while maintaining a reasonable anodic stability of the ethereal solvents. At the same time, the diluting solvents can also reduce viscosity and improve wettability towards different cell components, and thus improving the overall kinetics of electrochemical reactions. However, only short-chain ethereal solvents such as dimethoxyethane and diethoxyethane were used in these studies.[16-19] These short-chain ethereal solvents are highly flammable even at a relatively high salt

concentration, imposing severe safety issues on lithium metal batteries.[20] Moreover, the use of solely lithium sulfonylimide salts induces corrosion on the aluminum current collector. Therefore, it is essential to extend the current library of ethereal solvents, which clearly cannot satisfy all the requirements of high ionic conductivities, excellent oxidative stability, and good compatibility with lithium salts for practical high-voltage Li-metal batteries.

In an attempt to extend the current library of ethereal solvents, we pursued a chemistry approach to design and synthesize several fluorinated ethereal solvents with enhanced anodic stability.[21-23] Newly synthesized fluorinated glycol ether (FGE) based electrolytes in this research exhibit outstanding electrochemical performance for Li-metal batteries. By changing the length of ethylene glycol units and fluorinating the terminal groups, the structure-property relationship was revealed. It was observed that the cycling stability and the polarization of Li-metal batteries using FGE based electrolytes exhibited significant improvement over not only the cells employing conventional regular carbonate electrolyte, but also the cells using other regular glycol ether based electrolytes. As demonstrated in this paper, fluorinated diethylene glycol ether (FDG, 1,1,1-trifluoro-2-(2-(2-(2,2,2-trifluoroethoxy)ethoxy)ethoxy)ethane) successfully enabled the stable cycling of Li-metal batteries pairing lithium cobalt oxide (LCO, $LiCoO_2$) cathode with lithium metal anode. This is attributed to the terminal fluorinated alkyl groups, which improve the anodic stability of the molecule, and the optimum glycol ether unit in FDG, which allows the terminal fluorinated alkyl groups to exhibit a significant inductive effect on the whole molecule, while rendering the FDG molecule ability to solvate lithium cations and dissolve

lithium salts.

Materials: *Synthesis of 1,1,1-trifluoro-2-(2-(2-(2,2,2-trifluoroethoxy)ethoxy)ethoxy)-ethane (FDG)*: 2,2,2-trifluoroethanol (10.0 g , 2.4 equiv.) was added dropwise to a mixture of sodium hydride (60 % in mineral oil , 6.7 g , 4 equiv.) and tetrahydrofuran (THF, 200 mL) at 0 °C via syringe pump under nitrogen atmosphere . The resulting mixture was allowed to stir for 2h at room temperature. After that, oxybis(ethane-2,1-diyl) bis(4-methylbenzenesulfonate) (17.2g, 1 equiv.) dissolved in 100 mL THF was added dropwise to the resulting fluoroalkoxide solution at 0°C . The resulting solution was refluxed for 8h and then quenched with water. The reaction mixture was then extracted by 80 mL ethyl acetate for three times and the combined organic phase was washed with brine and dried over anhydrous sodium sulfate. After the removal of solvent by a rotary evaporator, the crude product was dried over 4 Å molecular sieves and then purified by vacuum distillation. The final product (b. p.: 67° C at 8 mmHg) is a colorless liquid (5.24 g, 47% yield). ^{1}H-NMR ($CDC1_3$, 300 MHz): δ 3.88 (q, 4H, 8.7Hz), 3.71 (m, 8H); ^{13}C-NMR ($CDC1_3$, 75 MHz): δ 129.5, 125.8, 122.1, 118.4 (q, 278 Hz), 78.9, 70.7, 69.4, 68.9, 68.5, 68.0 (q, 34 Hz).

Synthesis of 1,1,1,14,14,14-hexafluoro-3,6,9,12-tetraoxatetradecane (FTrG): 2,2,2-trifluoroethanol (10.0 g, 2.4 equiv.) was added dropwise to a mixture of sodium hydride (60 % in mineral oil, 6.6 g, 4 equiv.) and 200 mL THF at 0 °C via syringe pump under nitrogen atmosphere. The resulting mixture was allowed to stir for 2h at room temperature. After that, (ethane-1,2-diylbis(oxy))bis(ethane-2,1-diyl)bis(4-methyl-benzenesulfonate) (19.1 g , 1 equiv.) dissolved in 100 mL THF was then added dropwise to the resulting

fluoroalkoxide solution at 0° C. The resulting solution was then refluxed for 8 h before quenching by adding water. The reaction mixture was extracted by 80 mL ethyl acetate for three times and the combined organic phase was washed with brine and dried over anhydrous sodium sulfate. After the removal of solvent by a rotary evaporator, the crude product was dried over 4Å molecular sieves and then purified by vacuum distillation. The final product (b.p.: 96° C at 8 mmHg) is a colorless liquid (7.36g, 56% yield). ^{1}H-NMR ($CDC1_3$, 300 MHz): δ 3.89 (q, 4H, 8.9 Hz), 3.71 (m, 12H); ^{13}C-NMR ($CDC1_3$, 75 MHz): δ 129.5, 125.8, 122.1, 118.4 (q, 278 Hz), 71.8, 70.6, 70.6, 69.3, 68.9, 68.4, 68.0 (q, 34 Hz). *Synthesis of 1,1,1,17,17,17-hexafluoro-3,6,9,12,15-pentaoxaheptadecane (FTeG)*: 2,2,2-trifluoroethanol (10.0 g, 2.4 equiv.) was added dropwise to a mixture of sodium hydride (60 % in mineral oil, 6.7 g, 4 equiv.) and 200 mL THF at 0° C via syringe pump under nitrogen atmosphere. The resulting mixture was allowed to stir for 2h at room temperature. After that, ((oxybis(ethane-2,1-diyl))bis(oxy))bis(ethane-2,1-diyl) bis(4-methylbenzenesulfonate) (21 g, 1 equiv.) dissolved in 100 mL THF was then added dropwise to the resulting fluoroalkoxide solution at 0° C . The resulting solution was refluxed for 8 h and then quenched by adding water. The reaction mixture was extracted by 80 mL ethyl acetate for three times and the combined organic phase was washed with brine and dried over anhydrous sodium sulfate. After the removal of solvent by a rotary evaporator, the crude product was dried over 4Å molecular sieves and then purified by vacuum distillation. The final product (b.p.: 129° C at 8 mmHg) is a colorless liquid (6.79 g, 45% yield). ^{1}H-NMR ($CDC1_3$, 300 MHz): δ 3.89 (q, 4H, 8.8 Hz), 3.76 (m, 4H), 3.65 (m,

12H); ^{13}C-NMR ($CDC1_3$, 75 MHz): δ 129.5, 125.8, 122.1, 118.4 (q, 278 Hz), 71.8, 70.6, 70.5, 70.5, 69.3, 68.8, 68.4, 67.9 (q, 34 Hz).

The fluorinated glyme analogues were characterized by NMR spectroscopy to identify the chemical structure and purity. All NMR spectra were acquired on a 300 MHz Bruker spectrometer. ^{1}H chemical shifts were referenced to chloroform-*d* ($CDCl_3$) at 7.27 ppm and ^{13}C chemical shifts were referenced to 77.0 ppm.

The electrolyte salts $LiPF_6$ (BASF, battery grade) was used as received and LiTFSI (Sigma-Aldrich, 99.95%) was dried in a vacuum oven overnight at 80 ºC before use. The solvents 1NM3 (MERF facility, Argonne National Laboratory), DG, TrG and TeG were first dehydrated by adding 4 Å molecular sieves and then purified by vacuum distillation before use. Karl-Fischer titration indicated the water content of all solvents was less than 20 ppm. Deuterated chloroform was used as received. All samples were prepared in an argon atmosphere glovebox (< 1 ppm of O_2 and H_2O) by mixing the selected molar or volume ratio of each solvent, or by adding an appropriate molar or volume ratio of each solvent to the $LiPF_6$ salt or LiTFSI salt in a vial with stirring until a homogeneous solution was obtained. Cathode LCO ($LiCoO_2$) consisted of 94 wt% LCO (BTR New Energy), 2 wt% carbon black and 4 wt% Solvey 5130 PVDF binder coated on aluminum foil was supplied by the Cell Analysis, Modeling, and Prototyping (CAMP) Facility at Argonne National Laboratory. Celgard 2325 was used as the separator. The effective diameters of the cathode, lithium anode, and separator were 14, 16, and 17 mm, respectively. The electrode laminates were dried at 100 °C under vacuum overnight.

Electrochemical testing: Galvanostatic charge/discharge cycling was performed using

2032 coin cells at a C/2 rate with a cutoff voltage between 4.1 V and 3.0 V following three formation cycles at a C/10 rate. Cell voltage profiles and capacity were recorded using a MACCOR Electrochemical Analyzer. The Li||LCO cell used in this work has an LCO positive electrode (1.43 mAh cm^{-2} areal capacity), a foil of Li metal anode, one piece of separator (Celgard 2325), and the prepared electrolyte (30 µL in each cell). Both Li||LCO and Li||Li coin cells were prepared in an argon atmosphere glovebox (<1 ppm of O_2 and H_2O). Linear sweep voltammetry was performed using a Bio-Logic VMP3 station in a three-electrode configuration with Pt electrode (8 mm in diameter) as a working electrode and lithium metal as counter and reference electrodes; the scan rate was 5 mV/s. The cycle life of symmetrical lithium metal cells was tested with a depth of cycling of 4mAh cm^{-2} under the current density of 2 mA cm^{-2}.

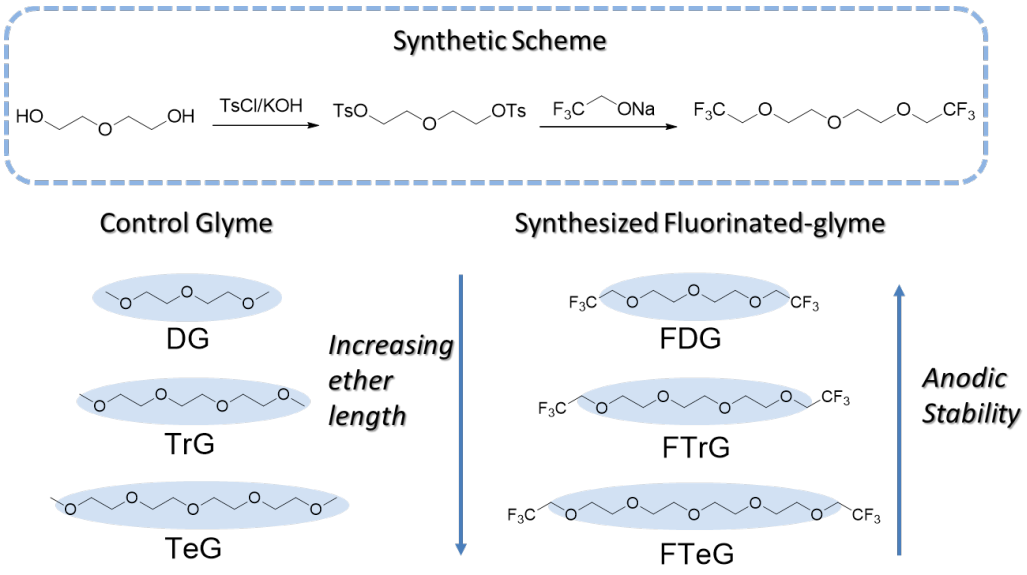

Figure 41. Motivation and synthetic scheme of fluorinated glycol ethers.

Rationale for molecular design and synthesis. In this work, the terminal methyl groups of

the glyme molecules were replaced by fluoroalkyl groups. As a result, the electron density of the lone pairs on the terminal oxygen atoms are heavily withdrawn by the fluorinated groups; hence, the fluorinated glycol ethers (FGEs) possess significantly higher oxidative stability compared to their non-fluorinated counterparts, rendering some FGEs high compatibility towards layered oxide cathodes with a relatively high charge cutoff voltage. Unlike fluorinated mono-glycol ether such as 1,2-(1,1,2,2-Tetrafluoroethoxy)ethane, which cannot dissolve any lithium salt, the non-fluorinated ethereal oxygen(s) inside the FGEs endue the solvents with high salt solubility and ionic conductivity. More importantly, compared to regular glyme solvents, FGEs suppress ether cleavage in Lewis acidity condition due to the strong electron-withdrawing effect of fluorinated groups, making the formation of the carbocation intermediates unlikely.[24] Thus, the as-designed FGEs demonstrate outstanding compatibility with most common lithium salts, including $LiPF_6$, which can easily induce ether cleavage in regular glyme solvents.

Figure 41 presents our motivation and synthetic route for the FGEs. The FGEs were synthesized from the corresponding glycols. The terminal hydroxyls of the glycols were first modified to sylate through the nucleophilic substitution reaction of 4-toluenesulfonyl chloride and deprotonated glycols, turning the terminal hydroxyls into excellent leaving groups. The ditosylates were then reacted with trifluoroethoxide to form the resulting fluorinated glyme analogues. The ethylene glycol segments were varied from DG (diglyme) to TrG (triglyme) to TeG (tetraglyme). By elongating the length of the ethylene glycol segments, the electronic inductive effect induced by the fluorinated terminally alkyl groups to the center of the molecule was significantly decreased, leading to reduced electro-

oxidative stability for FGEs with a longer chain. The beneficial effect of fluorination can be further demonstrated by switching the terminal group from alkyl group (DG) to fluoroalkyl group (FDG) to silyl group (1NM3, 2,2-dimethyl-3,6,9,12-tetraoxa-2-silatridecane). Taken together, the short-chain terminally fluorinated glyme analogs not only provide better lithium stabilization capability; but also significantly enhanced anodic stability compared to their regular or silyl-substituted counterparts.

To study the fluorination effect and the effect of glycol ether chain, we synthesized 1,1,1-trifluoro-2-(2-(2-(2,2,2-trifluoroethoxy)ethoxy)ethoxy)ethane (FDG), 1,1,1,14,14,14-hexafluoro-3,6,9,12-tetraoxatetradecane (FTrG) and 1,1,1,17,17,17-hexafluoro-3,6,9,12,15-pentaoxaheptadecane (FTeG), which are respectively the analogues of DG, TrG and TeG. Nuclear magnetic resonance (NMR) spectroscopy was used to confirm the synthesis of the products and the efficacy of purification. **Figures 42a**, 42**b** and **42c** display respectively the ^{1}H-NMR, ^{13}C-NMR and ^{19}F-NMR spectra of FDG. The chemical shifts and integrations of the peaks matched the structures of the as-designed molecules without any observable impurities. The NMR spectra of FTrG and FTeG were exhibited in **Figures 43** and **44** respectively. These results clearly validate our synthesis of the as-designed fluorinated glyme analogues.

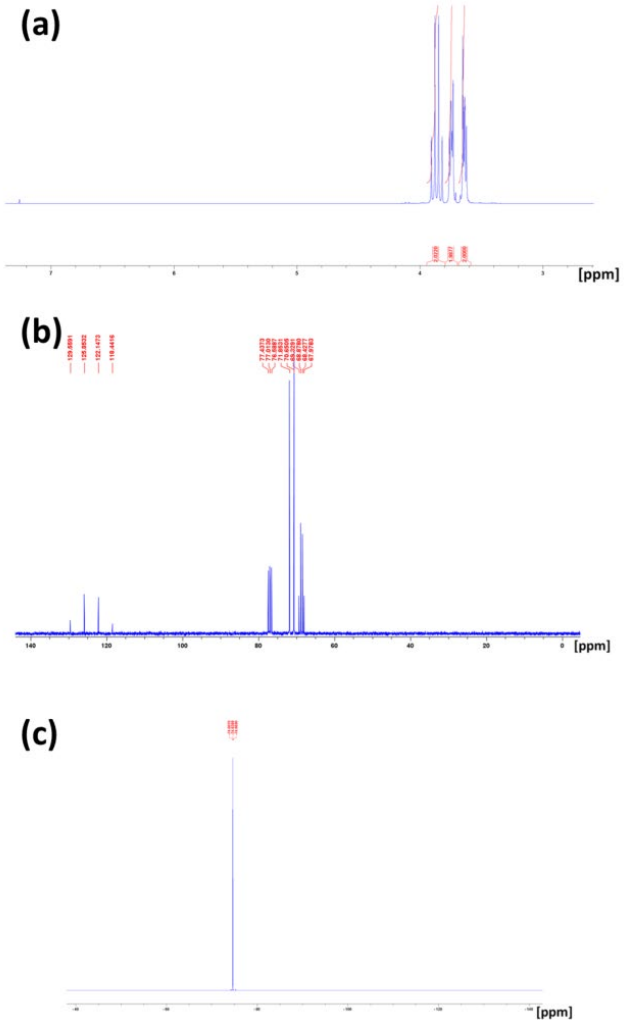

Figure 42. (a) 1H-NMR, (b) 13C-NMR, and (c) 19F-NMR spectra of the as-synthesized FDG.

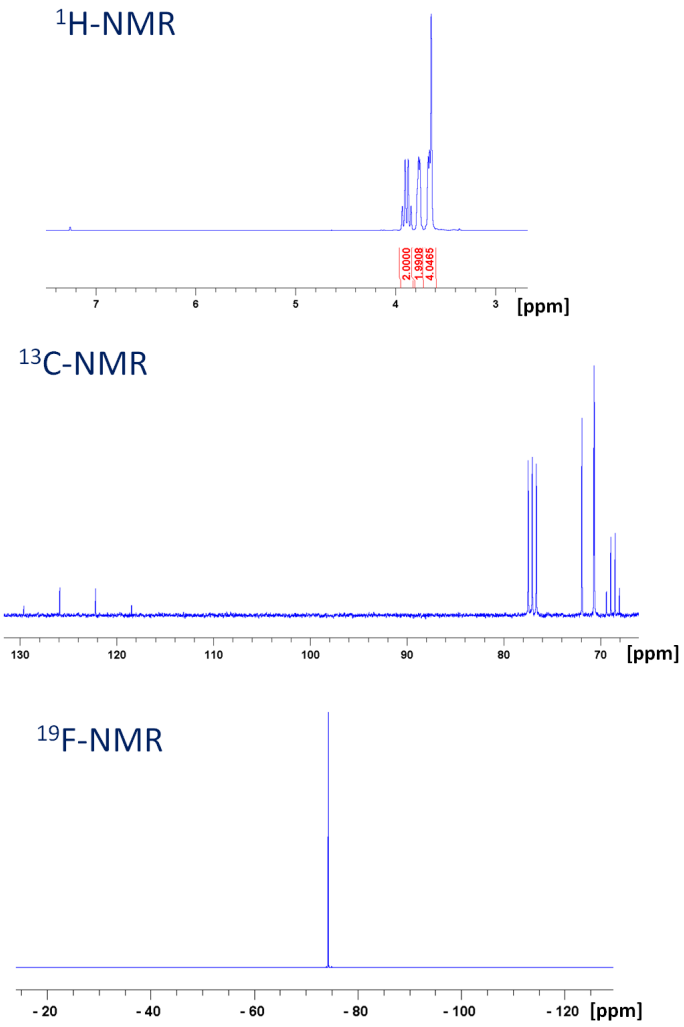

Figure 43. NMR spectra of the as-synthesized FTrG.

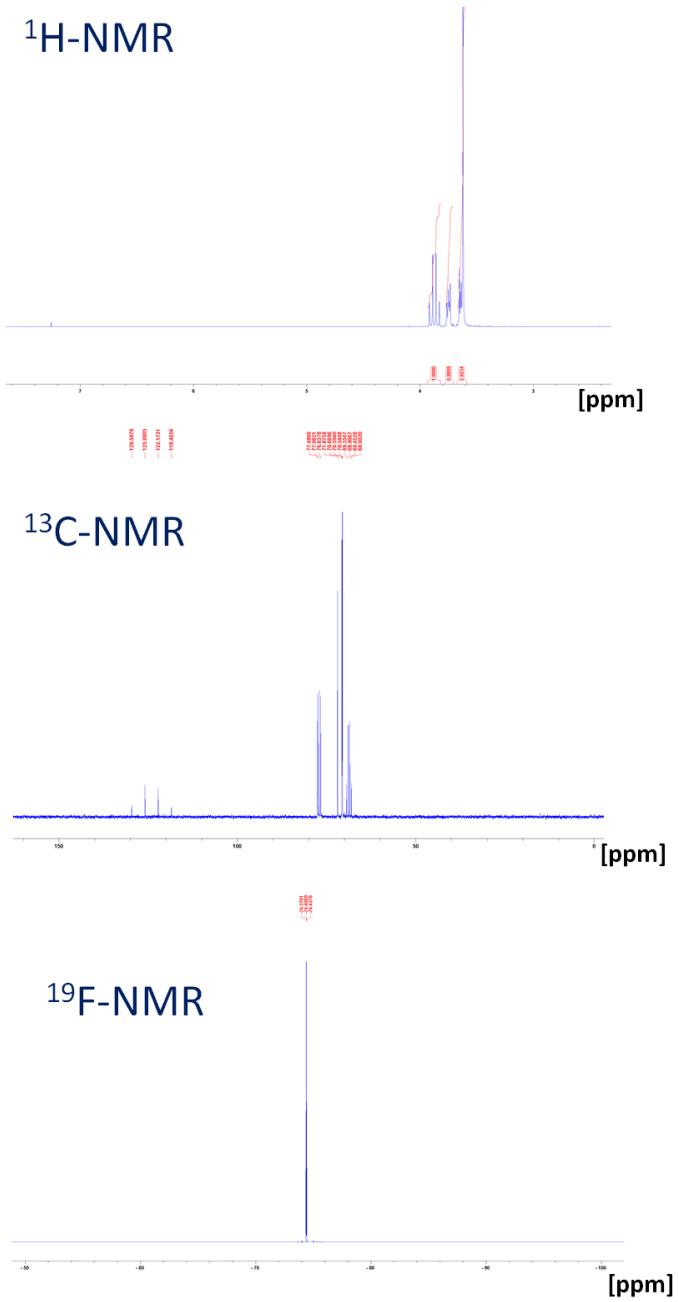

Figure 44. NMR spectra of the as-synthesized FTeG.

***Electrochemical properties*. Figure 45** shows the chemical structures of the solvents and salts used in this research and their purposes. A commercial lithium-ion battery electrolyte normally contains $LiPF_6$ dissolved in a cyclic carbonate (EC, ethylene carbonate), and

linear carbonates (such as EMC, ethyl methyl carbonate). Linear carbonates functioning as a thinning solvent in the electrolyte not only significantly reduce the viscosity of the electrolyte but also increases the wettability towards other cell components. Meanwhile. the cyclic carbonate acts as a solid-electrolyte interphase (SEI) enabler. Although EC is widely adopted as the SEI enabler for the graphite anode, it does not form a stable SEI on lithium metal anode.[25-30] In this study, we first assessed the capability in stabilizing lithium metal anode for individual glyme and FGE solvents. It was discovered that the capability of FGEs in facilitating lithium plating/stripping is significantly better than that of glymes or silyl glycol ether (1NM3). Although FGEs are not able to initiate highly stable SEI on lithium metal surface, with the use of fluorinated cyclic carbonates such as fluoroethylene carbonate (FEC), an extraordinarily benign and robust SEI can be effectively formed.[31] Therefore, FEC was chosen as the co-solvent of the electrolyte system for cycling of the lithium metal cells with layered oxide cathode. At the same time, a systematic comparison was conducted among all the glycol ether solvents to understand how the terminal group and the length of glycol ether unit impact the electrolyte properties.

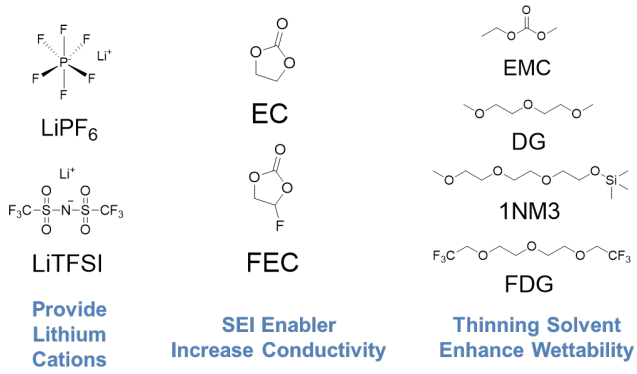

Figure 45. Chemical structures of solvents and salts used in this study and their purposes.

To evaluate the anodic stability of various glycol ether solvents, we carried out linear sweep

voltammetry (LSV) study using a three-electrode cell setup with lithium as reference and counter electrodes, and platinum working electrode. As expected, FDG possesses exceptional high anodic stability compared to its non-fluorinated and silyl analogues, *i.e.* DG and 1NM3. As depicted in **Figure 46**, the onset oxidation voltages of 1 M LiTFSI in FDG was around 4.8 V, which was significantly higher than that of 1 M LiTFSI in DG (3.8 V) and in 1NM3 (4.3 V). Therefore, electrolyte using FDG are expected to be highly stable towards the layered oxide LCO cathode.

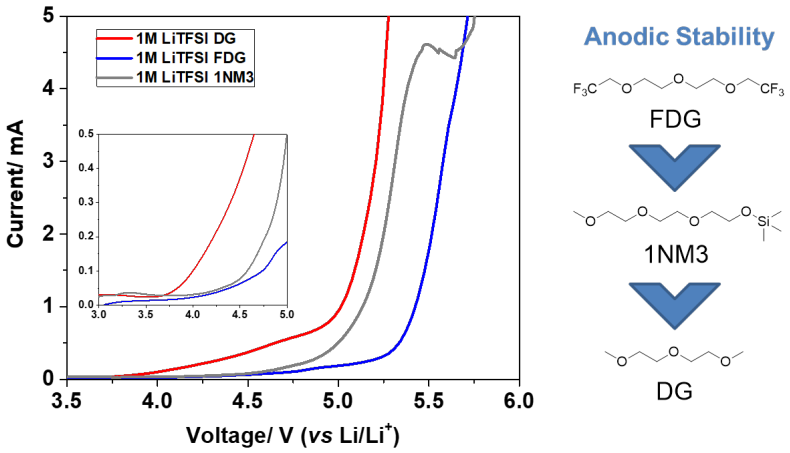

Figure 46. Linear sweep voltammograms of 1 M LiTFSI in DG, FDG, and 1NM3, individually.

The lithium stability of various glycol ether solvents was further assessed by Li||Li symmetric cell cycled at 2 mA/cm^2 current density. As illustrated in **Figure 47a**, the charge/discharge voltage stabilized at about 0.5 V for the cells using the FDG-based electrolyte. In contrast, the deposition-stripping overpotentials for DG- and 1NM3-based electrolytes were large and highly fluctuating. These results clearly showed that FDG electrolytes enabled much more stable lithium plating and stripping due to outstanding

stability towards Li metal than DG and 1NM3 electrolytes. Thus, fluorination of glycol ether not only enhances the anodic stability of the solvent but also its ability to stabilize the lithium anode. In fact, regular glycol ether DG is highly unstable towards lithium metal anode, especially when $LiPF_6$ salt was used in the electrolyte. As displayed in **Figure 48**, the voltage profile of Li||Li symmetric cell using 1.2M $LiPF_6$ in DG polarized almost instantly, partially due to the incompatibility between regular glyme and $LiPF_6$ as mentioned above. However, $LiPF_6$ is still the preferred lithium salt for lithium batteries.[32]

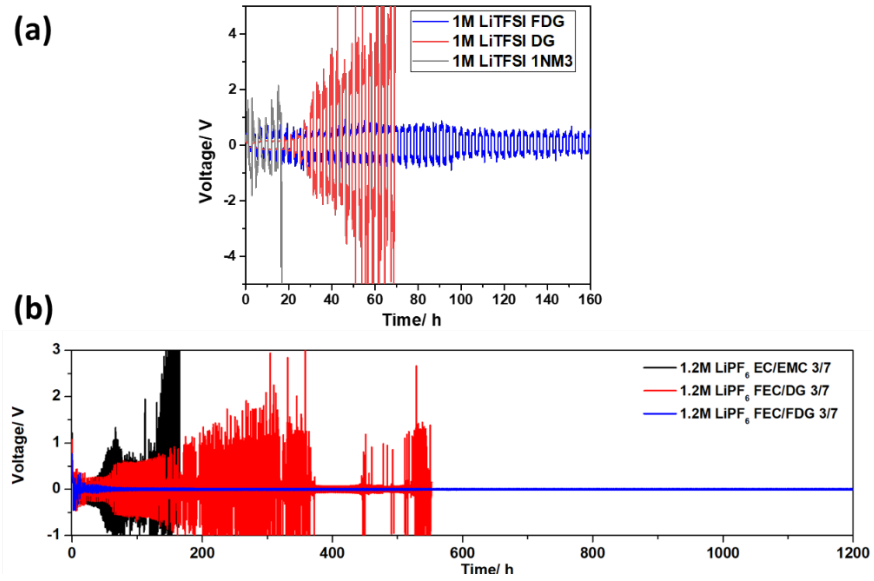

Figure 47. Li||Li symmetrical cells using electrolytes (a) 1M LiTFSI in solvents of, individually, FDG, DG, and 1NM3; and (b) 1.2M LiPF6 dissolved in EC and EMC in a 3:7 ratio, FEC to DG (3:7), and FEC to FDG (3:7).

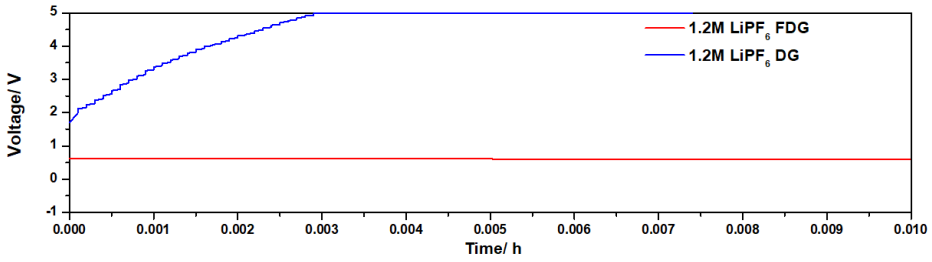

Figure 48. Li||Li symmetric cells using 1.2M LiPF6 in DG and FDG electrolytes.

It was discovered that $LiPF_6$-FGE electrolytes exhibited significantly enhanced stability towards lithium metal anode, evidenced by the Li||Li symmetric cells data shown in **Figure 49**. Unlike the cell using regular glycol ether solvents, the Li||Li symmetric cell using 1.2M $LiPF_6$ in FTeG displayed relatively stable cycling for more 30 cycles. The lithium metal compatibility was further improved for electrolyte using FGE with shorter glycol ether unit, *i.e*. FDG.

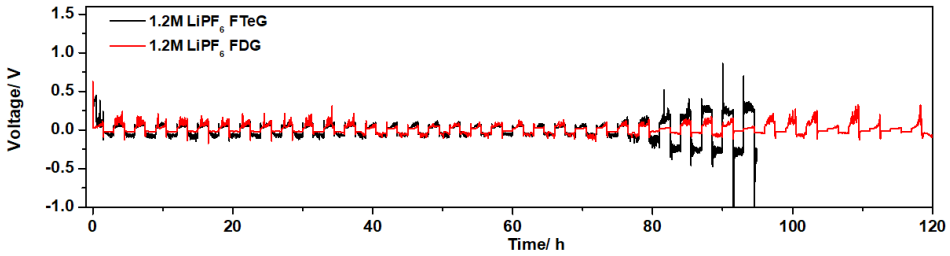

Figure 49. Li||Li symmetric cells using 1.2M LiPF6 in FTeG and FDG electrolytes.

As depicted in **Figure 50**, the Li||Li cell employing $LiPF_6$-FDG electrolyte undoubtedly demonstrated enhanced lithium plating/stripping capability compared to the cell using conventional $LiPF_6$-EC-EMC electrolyte. The lithium stability of FGE based electrolytes can be further enhanced with the use of FEC as co-solvent.

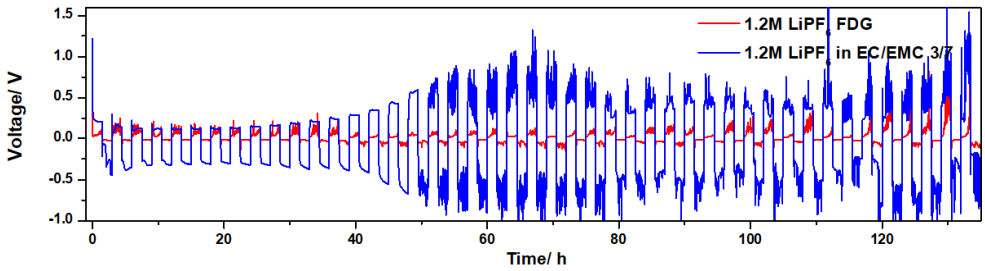

Figure 50. Li||Li symmetric cells using 1.2M LiPF6 in FDG and conventional EC-EMC electrolytes.

Figure 47b shows the result of Li||Li symmetric cells using conventional electrolyte with 1.2M $LiPF_6$ dissolved in EC and EMC in a 3:7 ratio, as well as FEC/DG and FEC/FDG binary electrolytes. The cells were cycled at a current density of 2 mA/cm^2. With the addition of the cyclic carbonate FEC, the FEC/FDG electrolyte exhibited superior stability in the lithium plating and stripping indicated by the stable and small charge/discharge voltage (20 mV). Meanwhile, the over-potential of the Li||Li cell using FEC/DG electrolyte fluctuated and was considerably larger (1 V). The worst symmetric cell result came from the conventional electrolyte, where the over-potential was as high as 5V.

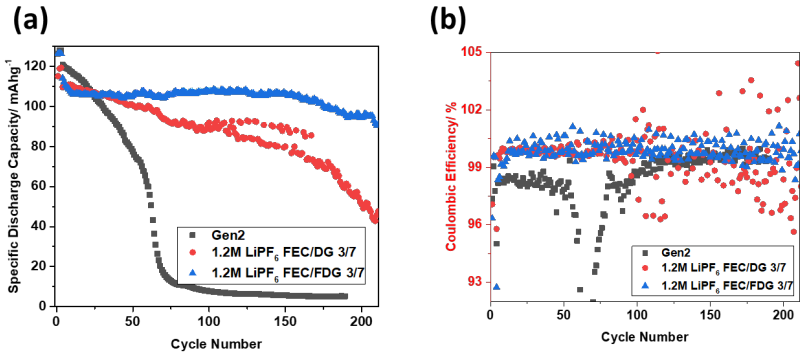

Figure 51. (a) Cycling performance and (b) Coulombic efficiency Li||LCO cells using 1.2M LiPF6 dissolved in EC and EMC in a 3:7 ratio, FEC to DG (3:7), and FEC to FDG (3:7) electrolytes.

Cycling performance of lithium metal batteries. The effectiveness of FGE solvents was further demonstrated by the cycling performance of Li||LCO cells. As illustrated in **Figure 51**, that the capacity of Li||LCO cell employing conventional $LiPF_6$-EC-EMC electrolyte decayed rapidly and lost almost all capacity within 70 cycles due to poor compatibility between electrolyte and the lithium metal anode. Meanwhile, the 100-cycle capacity retention of the Li||LCO cell employing the DG based electrolyte was 84.2% with an average 200-cycle Coulombic efficiency of 99.87%, indicating that DG based electrolyte enabled more stable cycling of the Li||LCO system. While the cycling performance of Li||LCO cell using glycol ether (1NM3) based electrolyte was worse than the cell employing DG based electrolyte, probably due to the lowered anodic stability caused by the silyl group (**Figure 52**).

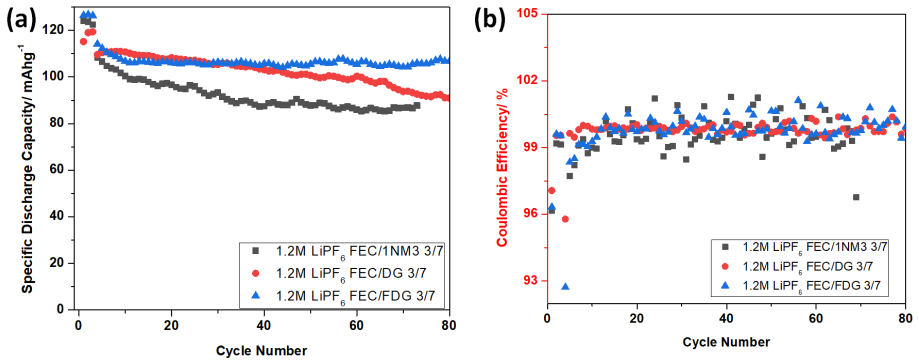

Figure 52. (a) Cycling performance and (b) Coulombic efficiency Li||LCO cells using 1.2M LiPF6 applying a 3:7 ratio of FEC to 1NM3, DG, and FDG electrolytes.

Outstanding cycling performance of the Li||LCO system was obtained from the cell using the FDG based electrolyte, showing a 95.7% 100-cycle capacity retention and an average 200-cycle Coulombic efficiency of 99.92%. Details regarding the cycling performance of Li||LCO cells using various electrolytes were summarized in **Table 10**. Together with the

symmetric cell data, our results strongly supported the fluorinated glycol ether is superior to regular glycol ether and silyl glycol ether in stabilizing the cycling of lithium metal anode and its compatibility towards layered metal oxide cathode.

To gain a deeper understanding on the structure-property relationship of various solvents, we further investigated the effect of the glycol ether length on the glycol ether and fluorinated glycol ether based electrolytes. The electrochemical performance of Li||LCO cells cycling at a rate of C/2 between 3.0 V and 4.1 V was displayed in **Figures 53a** and **53b**, which illustrate respectively the capacity retention and Coulombic efficiency (CE) of Li||LCO cells using 1.2 M $LiPF_6$ dissolved in FEC and various glycol ether co-solvents with different glycol units. The details of the cycling performance were also summarized in **Table 10**. The cell using FTrG based electrolyte displayed 92.4% 100-cycle capacity retention (CR-100) and 99.90% average 100-cycle CE (ACE-100), which were significantly higher than the cell employing TrG based electrolyte, which showed 69.4% CR-100 and 99.76% ACE-100. Clearly, for the cells using FGE based electrolytes with glycol ether units less than or equal to 3, both the capacity retention and average CE were superior to the cells employing electrolytes based on their non-fluorinated counterparts. These results are consistent with our previous finding that fluorination of glycol ether not only stabilizes lithium metal anode, but also enhances the anodic stability of the glycol ethers. However, the further increase in the length of glycol unit does not provide significant beneficial effect on the anodic stability and lithium metal stabilization capability of the terminally fluorinated glyme analogue. This is because the inductive effect of the terminal fluorinated groups faded out across the long glycol ether chain. Thus, cells

employing FTeG based electrolyte displayed 65.4% CR-100, which is even lower than the CR-100 of cells using TeG based electrolyte. Evidently, our new FDG based electrolyte actually clearly shows the superior capacity retention and Coulombic efficiency in all cases.

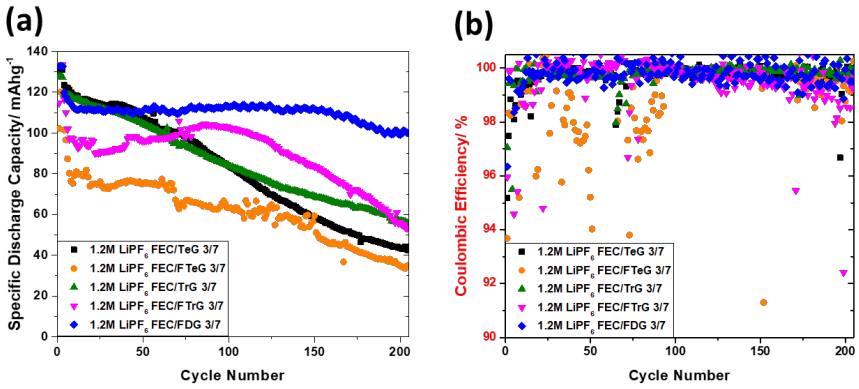

Figure 53. (a) Capacity retention and (b) Coulombic efficiency of Li||LCO cells using 1.2M LiPF6 applying a 3:7 ratio of FEC to TeG, FTeG, TrG, FTrG, and FDG electrolytes.

Conclusion: In sum, we have successfully expanded the library of solvents for lithium metal batteries by introducing a series of new fluorinated glymes. Unlike their non-fluorinated counterparts, these newly synthesized fluorinated glycol ethers are not only highly compatible with lithium hexafluorophosphate salt but also enable more stable lithium plating/stripping, as well as possess enhanced anodic stability. Lithium metal cells using electrolyte based on the fluorinated diglyme analogue FDG displayed the best cycling performance, which is unambiguously superior to the cells employing non-fluorinated glymes and silyl glycol ether. This is because FDG possesses not only the terminal fluorinated alkyl groups, which largely enhance its anodic stability but also a balanced glycol ether unit, which is short enough for the terminal fluorinated alkyl groups to exhibit a significant inductive effect on the whole molecule, while long enough to solvate

lithium cations and dissolve lithium salts.

Table 10. Data associated with Figures 5 and 6 for Li||LCO cell operated at a voltage range of 3.0-4.1 V with 1.2 M LiPF6 FEC-based electrolytes and conventional electrolyte: 1st-cycle Coulombic efficiency (1st CE), 1st cycle discharge capacity (1st DC), capacity retention after 100 and 200 cycles (CR-100 and CR-200), average capacity of 100 and 200 cycles (AC-100 and AC-200), and average 200-cycle Coulombic efficiency (ACE-200).

Electrolyte	1st CE	1st DC (mAh/g)	CR-100	AC-100 (mAh/g)	ACE-100	CR-200	AC-200 (mAh/g)	ACE-200
1.2M $LiPF_6$ EC/EMC 3/7 (Gen2)	97.4	126.4	6.1 %	61.0	96.36 %	N/A	N/A	N/A
1.2M $LiPF_6$ FEC/DG 3/7	97.07	115.1	84.2 %	99.3	99.87 %	44.3%	87.9	99.69%
1.2M $LiPF_6$ FEC/FDG 3/7	96.3	132.7	95.7 %	111.7	99.92 %	84.6%	110.0	99.90%
1.2M $LiPF_6$ FEC/TrG 3/7	97.06	128.0	69.4 %	101.4	99.76%	46.8%	84.8	99.84%
1.2M $LiPF_6$ FEC/FTrG 3/7	95.94	114.7	92.4 %	98.0	99.90%	48.4%	88.9	99.69%
1.2M $LiPF_6$ FEC/TeG 3/7	95.17	123.7	72.6 %	92.4	99.77%	27.8%	72.9	99.79%
1.2M $LiPF_6$ FEC/FTeG 3/7	93.68	102.3	65.4 %	71.9	94.74%	35.8%	60.8	87.83%

Reference

1 Park, Min Sik, Sang Bok Ma, Dong Joon Lee, Dongmin Im, Seok-Gwang Doo, and Osamu Yamamoto. "A highly reversible lithium metal anode." *Scientific reports* 4, no. 1 (2014): 1-8.

2 Horstmann, Birger, Jiayan Shi, Rachid Amine, Martin Werres, Xin He, Hao Jia, Florian Hausen et al. "Strategies towards enabling lithium metal in batteries: interphases and electrodes." *Energy & Environmental Science* 14, no. 10 (2021): 5289-5314.

3 He, Xin, Dominic Bresser, Stefano Passerini, Florian Baakes, Ulrike Krewer, Jeffrey Lopez, Christopher Thomas Mallia et al. "The passivity of lithium electrodes in liquid

electrolytes for secondary batteries." *Nature Reviews Materials* 6, no. 11 (2021): 1036-1052.

4 Xie, Miao, Yu Wu, Yue Liu, P. P. Yu, Ran Jia, William A. Goddard III, and Tao Cheng. "Pathway of in situ polymerization of 1, 3-dioxolane in LiPF6 electrolyte on Li metal anode." *Materials Today Energy* 21 (2021): 100730.

5 Liu, Tingting, Jianjun Zhang, Wu Han, Jinning Zhang, Guoliang Ding, Shanmu Dong, and Guanglei Cui. "In situ polymerization for integration and interfacial protection towards solid state lithium batteries." *Journal of The Electrochemical Society* 167, no. 7 (2020): 070527.

6 Zhang, Jian, Jiayan Shi, Xiaoyu Wen, Yifan Zhao, and Juchen Guo. "Properties of thin lithium metal electrodes in carbonate electrolytes with realistic parameters." *ACS Applied Materials & Interfaces* 12, no. 29 (2020): 32863-32870.

7 Sayed, Farheen N., Marco-Tulio F. Rodrigues, Kaushik Kalaga, Hemtej Gullapalli, and P. M. Ajayan. "Curious case of positive current collectors: Corrosion and passivation at high temperature." *ACS applied materials & interfaces* 9, no. 50 (2017): 43623-43631.

8 Shkrob, Ilya A., Krzysztof Z. Pupek, and Daniel P. Abraham. "Allotropic control: How certain fluorinated carbonate electrolytes protect aluminum current collectors by promoting the formation of insoluble coordination polymers." *The Journal of Physical Chemistry C* 120, no. 33 (2016): 18435-18444.

9 Jiao, Shuhong, Xiaodi Ren, Ruiguo Cao, Mark H. Engelhard, Yuzi Liu, Dehong Hu, Donghai Mei et al. "Stable cycling of high-voltage lithium metal batteries in ether electrolytes." *Nature Energy* 3, no. 9 (2018): 739-746.

10 Fan, Xiulin, Long Chen, Xiao Ji, Tao Deng, Singyuk Hou, Ji Chen, Jing Zheng et al. "Highly fluorinated interphases enable high-voltage Li-metal batteries." *Chem* 4, no. 1 (2018): 174-185.

11 Yamada, Yuki, and Atsuo Yamada. "Superconcentrated electrolytes for lithium batteries." *Journal of The Electrochemical Society* 162, no. 14 (2015): A2406.

12 Yamada, Yuki, Jianhui Wang, Seongjae Ko, Eriko Watanabe, and Atsuo Yamada. "Advances and issues in developing salt-concentrated battery electrolytes." *Nature Energy* 4, no. 4 (2019): 269-280.

13 Chen, Shuru, Jianming Zheng, Donghai Mei, Kee Sung Han, Mark H. Engelhard, Wengao Zhao, Wu Xu, Jun Liu, and Ji-Guang Zhang. "High-voltage lithium-metal

batteries enabled by localized high-concentration electrolytes." *Advanced materials* 30, no. 21 (2018): 1706102.

14 Reuter, Florian S., Chen-Jui Huang, Yi-Chen Hsieh, Susanne Dörfler, Gunther Brunklaus, Holger Althues, Martin Winter, Shawn D. Lin, Bing-Joe Hwang, and Stefan Kaskel. "Stabilizing Effect of Polysulfides on Lithium Metal Anodes in Sparingly Solvating Solvents." *Batteries & Supercaps* 4, no. 2 (2021): 347-358.

15 Ren, Xiaodi, Lianfeng Zou, Xia Cao, Mark H. Engelhard, Wen Liu, Sarah D. Burton, Hongkyung Lee et al. "Enabling high-voltage lithium-metal batteries under practical conditions." *Joule* 3, no. 7 (2019): 1662-1676.

16 Gao, Mengyao, ChiCheung Su, Meinan He, Tobias Glossmann, Andreas Hintennach, Zhenxing Feng, Yaqin Huang, and Zhengcheng Zhang. "A high performance lithium–sulfur battery enabled by a fish-scale porous carbon/sulfur composite and symmetric fluorinated diethoxyethane electrolyte." *Journal of Materials Chemistry A* 5, no. 14 (2017): 6725-6733.

17 Fan, Xiulin, Long Chen, Oleg Borodin, Xiao Ji, Ji Chen, Singyuk Hou, Tao Deng et al. "Non-flammable electrolyte enables Li-metal batteries with aggressive cathode chemistries." *Nature nanotechnology* 13, no. 8 (2018): 715-722.

18 Lin, Shuangshuang, and Jinbao Zhao. "Functional Electrolyte of Fluorinated Ether and Ester for Stabilizing Both 4.5 V LiCoO2 Cathode and Lithium Metal Anode." *ACS Applied Materials & Interfaces* 12, no. 7 (2020): 8316-8323.

19 Pham, Thuy Duong, Abdullah Bin Faheem, Junam Kim, Hye Min Oh, and Kyung-Koo Lee. "Practical High-Voltage Lithium Metal Batteries Enabled by Tuning the Solvation Structure in Weakly Solvating Electrolyte." *Small* (2022): 2107492.

20 Bouibes, Amine, Soumen Saha, and Masataka Nagaoka. "Theoretically predicting the feasibility of highly-fluorinated ethers as promising diluents for non-flammable concentrated electrolytes." *Scientific reports* 10, no. 1 (2020): 1-10.

21 Su Chi-Cheung, Amine Khalil, He Meinan. 2020. Electrolyte for lithium batteries. US 10,868,333 B2, filed Jan. 23, 2019, and issued Dec. 15 , 2020.

22 Zhang Zhengcheng, Su Chi-Cheung. 2018. Fluoro-substituted ethers and compositions. US 2018 / 0076485 A1, filed Sep. 14, 2016, and issued Mar. 15, 2018.

23 Zhang Zhengcheng, Su Chi-Cheung. 2019. Fluoro-substituted ethers and compositions. US 2019 / 0237807 A1, Apr. 11, 2019, and issued Aug. 1, 2019.

24 Aouissi, Ahmed, Salem S. Al-Deyab, and Hassan Al-Shahri. "The cationic ring-opening polymerization of tetrahydrofuran with 12-tungstophosphoric acid." *Molecules* 15, no. 3 (2010): 1398-1407.

25 Su, Chi-Cheung, Meinan He, Rachid Amine, Zonghai Chen, Ritu Sahore, Nancy Dietz Rago, and Khalil Amine. "Cyclic carbonate for highly stable cycling of high voltage lithium metal batteries." *Energy Storage Materials* 17 (2019): 284-292.

26 Peled, Emanuel. "The electrochemical behavior of alkali and alkaline earth metals in nonaqueous battery systems—the solid electrolyte interphase model." *Journal of The Electrochemical Society* 126, no. 12 (1979): 2047.

27 Peled, E., C. Menachem, D. Bar-Tow, and A. Melman. "Improved Graphite Anode for Lithium-Ion Batteries Chemically: Bonded Solid Electrolyte Interface and Nanochannel Formation." *Journal of The Electrochemical Society* 143, no. 1 (1996): L4.

28 Peled, E., D. Golodnitsky, and G. Ardel. "Advanced model for solid electrolyte interphase electrodes in liquid and polymer electrolytes." *Journal of the Electrochemical Society* 144, no. 8 (1997): L208.

29 Peled, E., and S. Menkin. "SEI: past, present and future." *Journal of The Electrochemical Society* 164, no. 7 (2017): A1703.

30 An, Seong Jin, Jianlin Li, Claus Daniel, Debasish Mohanty, Shrikant Nagpure, and David L. Wood III. "The state of understanding of the lithium-ion-battery graphite solid electrolyte interphase (SEI) and its relationship to formation cycling." *Carbon* 105 (2016): 52-76.

31 Su, Chi-Cheung, Meinan He, Jiayan Shi, Rachid Amine, Jian Zhang, and Khalil Amine. "Solvation Rule for Solid-Electrolyte Interphase Enabler in Lithium-Metal Batteries." *Angewandte Chemie* 132, no. 41 (2020): 18386-18390.

32 Xu, Kang. "Nonaqueous liquid electrolytes for lithium-based rechargeable batteries." *Chemical reviews* 104, no. 10 (2004): 4303-4418.

4.2 Magnesium batteries

Rechargeable magnesium (Mg) batteries have received tremendous attention as a new electrochemical energy storage technology with the theoretic advantages of lower cost, better safety, and even higher energy density. However, rechargeable

Mg batteries are encountering significant challenges on all fronts, including electrolytes, anodes, and cathodes. The research community has yet to reach the stage of evaluating the technical and commercial feasibility of rechargeable Mg batteries. Instead, current studies should continue to explore new related chemistry and emphasize fundamental understandings.

An intrinsic requirement for rechargeable Mg batteries is the use of Mg metal anode. Although one can argue that Mg alloys formed electrochemically may be used, such anodes would defeat a main purpose of Mg batteries, *i.e.*, high energy density. The first attempt at Mg electrodeposition can be traced back to the report by Gaddum and French in 1927 using Grignard reagent solutions in ethers.[1] In the next half century, Mg electrolytes and Mg electrodeposition were scarcely reported in literature. Notably, Connor and coworkers in 1957 reported Mg deposition from an ethereal solution of magnesium borohydride ($Mg(BH_4)_2$) among a number of potential electrolytes.[2] Brenner in 1971 reported Mg deposition from an ethereal solution of a Mg-boron complex derived from the reaction between magnesium chloride ($MgCl_2$) and a Li derivative of decaborane. The same electrolyte could also be obtained from the reaction between a Grignard reagent and decaborane with $MgCl_2$ as the additive in tetrahydrofuran (THF).[3] These early studies preluded the burst of Mg battery research starting in the 1990s, of which the work of Gregory and coworkers in 1990 was representative.[4] Despite the considerable citations received by this work, its significant implications may still be undervalued and deserve further discussion. The authors elucidated two types of electrolytes that enabled Mg

deposition-stripping, both of which strongly influenced later studies: (1) electrolytes composed of Grignard reagents and aluminum chloride ($AlCl_3$) and (2) Mg salts with bulky organoborate anions with alkyl and/or phenyl substituents including tetrabutylborate ($B(C_4H_9)_4^-$ or BBu_4^-), tributylphenylborate (BBu_3Ph^-), and dibutyldiphenylborate ($BBu_2Ph_2^-$). More importantly, they studied the chemical and electrochemical magnesiation of a number of materials listed in **Table 11**. The successful chemical magnesiation using dibutyl-magnesium indicated that these materials could potentially host Mg via either intercalation or conversion (the mechanisms were not clear from the paper). However, the electrochemical magnesiation of these materials failed in the Grignard-based electrolytes ($RMgCl+AlCl_3$) and the $Mg(BBu_4)_2$ electrolyte.

Table 11. Mg host materials from chemical magnesiation using dibutyl-magnesium. The table is reproduced from ref. 4.

Material	Open-circuit Potential vs. Mg^0	Capacity Moles Mg/mole host	mAh/g
Co_3O_4	2.28	0.80	222
Mn_2O_3	2.40	0.66	224
Mn_3O_4	2.40	0.66	154
MoO_3	2.28	0.50	143
PbO_2	3.10	0.25	56
Pb_3O_4	3.10	0.25	20
RuO_2	2.55	0.66	266
V_2O_5	2.66	0.66	194
WO_3	2.16	0.50	116
TiS_2	1.63	0.15	157
VS_2	1.71	0.34	154
ZrS_2	2.60	0.66	228
MoB_2	1.15	0.66	301
TiB_2	1.25	0.42	324
ZrB_2	1.20	0.66	313

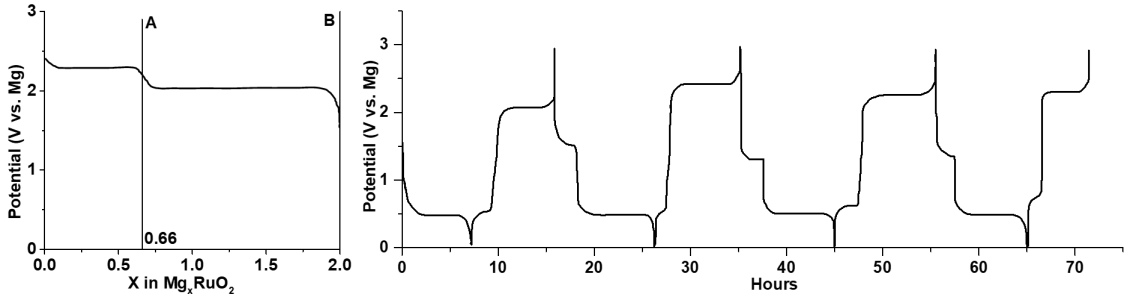

Figure 54. (a) Magnesiation potential curve of RuO2 in 1 M Mg(ClO4)2 in THF versus Mg at 1 mA cm-2. The first plateau (point A) is reversible and the full magnesiation (point B) is irreversible due to the complete reduction of Ru4+ to Ru0; (b) Cycling curve of Co_3O_4 versus Mg in 0.25 M $Mg(BBu_2Ph_2)_2$ in THF/DME at 24 mA g^{-1} with respect to Co_3O_4. The plots are reproduced from ref. 4.

The authors attributed the failure to the chemical magnesiation by the MgR_2 species, which were from the Schlenk equilibrium in the Grignard-based electrolytes and the decomposition of tetrabutylborate in $Mg(BBu_4)_2$, respectively. On the other hand, $Mg(BBu_2Ph_2)_2$ electrolyte in THF/1,2-dimethoxyethane (DME) mixture was found to be stable against decomposition. Despite the failed magnesiation in Grignard and $Mg(BBu_4)_2$ electrolytes, some of the materials in **Table 11** (evidenced by ruthenium oxide (RuO_2) shown in **Figure 54a**) were successfully electrochemically magnesiated in the magnesium perchloride ($Mg(ClO_4)_2$) electrolyte as primary cells; $Mg(ClO_4)_2$ electrolyte could only enable Mg stripping. Based on the results above, the authors demonstrated the first rechargeable Mg battery (**Figure 54b**) composed of Mg anode, cobalt oxide (Co_3O_4) cathode, and $Mg(BBu_2Ph_2)_2$ electrolyte in THF/DME. This work is regarded as the first successful demonstration of rechargeable Mg batteries. Inadvertently, it also served as the first hint at the importance and complexity of the interfaces in rechargeable Mg batteries.

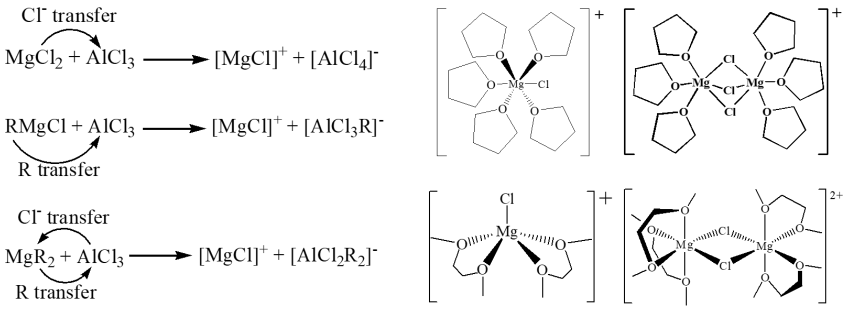

Figure 55. (a) Simplified transmetalation reactions between Lewis base and acid to produce active cations in the Mg electrolytes; (b) Representative solvation structures of [MgCl(THF)5]+ (top left),28 [MgCl(DME)2]+ (bottom left)29 monomer cations and [Mg2Cl3(THF) $[Mg_2Cl_3(THF)_6]^+$ (top right),[28] $[Mg_2Cl_2(DME)_4]^{2+}$ (bottom right)[29] dimer cations.

A great thrust of rechargeable Mg battery research came from the work by Aurbach and coworkers in 2000.[5] This work made two important contributions by (1) demonstrating Chevrel phase molybdenum sulfide (Mo_6S_8) as a new cathode material and (2) inventing a new type of electrolytes, namely dichloro-complex (DCC), composed of dialkyl Grignard (MgR_2) and aluminum Lewis acids ($AlCl_3$ or $alkylAlCl_2$). Mo_6S_8 remains as the "benchmark" Mg cathode mainly because to date it is the only cathode for which electrochemical intercalation is unambiguous and the mechanism is relatively well understood. Separately, the DCC electrolytes showed improved anodic stability but were not found to be fundamentally different from the Grignard electrolytes in Gregory's study. The active species in these electrolytes are THF-solvated $MgCl^+$ or $Mg_2Cl_3^+$ cations and the anions are chloroaluminates ($AlCl_{4-n}R_n^-$).[6-10] Aurbach and coworkers further improved the anodic stability by replacing the alkyl groups in DCC with phenyl moieties, resulting in the so-called all phenyl complex (APC) electrolytes.[10-12] However, these Grignard-based Mg electrolytes are problematic in Mg batteries containing electrophilic cathodes due to the nucleophilicity of the Grignard reagents. Therefore, researchers shifted their focus to Grignard-free electrolytes based on Mg-containing Lewis bases such as Mg alkoxides, [13,14] Mg fluorinated alkoxides,[15] and Mg amides such as hexamethyldisilazide magnesium chloride (HMDSMgCl)[16] and magnesium bis(hexamethyldisilazide) ($Mg(HMDS)_2$).[17-19] These compounds are not completely non-nucleophilic, and they still need to be combined with Lewis acids such as $AlCl_3$ to generate the active Mg-containing cations via transmetalation. The active halides

(mainly chloride) render these electrolytes corrosive and limit the anodic stability through chlorine generation. Therefore, the latest trend in Mg electrolyte research is to look to the "simple salt" electrolytes composed of solvated divalent Mg^{2+} cations ($Mg(solvent)_n^{2+}$) and weakly coordinating anions. This type of Mg electrolyte was proven feasible for Mg deposition-stripping, as Connor reported $Mg(BH_4)_2$ in 1957[2] and Gregory reported Mg organobrates in 1990.[4] To date, Mg simple salts that have been studied for Mg electrolytes, in addition to $Mg(BH_4)_2$ and Mg organobrates, include $Mg(ClO_4)_2$,[11] magnesium hexafluorophosphate ($Mg(PF_6)_2$),[20] magnesium bis(trifluoromethanesulfonyl)imide ($Mg(TFSI)_2$),[21] magnesium fluorinated alkoxyborate,[22] magnesium fluorinated alkoxyaluminate,[23-25] and magnesium carboranes.[26,27] The electrotechnical properties of simple salt electrolytes vastly vary, and are clearly affected by the solvents, cation-anion interactions, and anionic stability. In the following sections, we will discuss the interfaces in the aforementioned Mg electrolytes in the hope of shedding some light on the important issues of rechargeable Mg batteries.

Anode Interfaces (Mg deposition-stripping): Here, we focus on the interfacial phenomena during Mg deposition-stripping determined by the molecular structure and properties of the species in the electrolyte. For most of the Mg electrolytes from the combination of a Lewis base (Mg-containing species such as $MgCl_2$, RMgCl, MgR_2, ROMgCl, $Mg(OR)_2$, etc., where R is an organic ligand) and a Lewis acid (typically $AlCl_3$ or $AlCl_2R$), active cations are produced via transmetalation represented by the simplified reactions in Figure 55a. The $[MgCl]^+$ monomer cation in Scheme 1a is solvated by solvent

molecules, and the resultant solvation structures may differ depending on the solvents as in the examples shown in the left panel of Figure 55b: $[MgCl(THF)_5]^{+}$[28] versus $[MgCl(DME)_2]^{+}$ (Mg prefers four or six-coordination environment, thus this five-coordination is metastable).[29,30] Mg-Cl dimmer cations (right panel of Figure 55b) can coexist under equilibrium with the monomers, along with other species in the electrolytes such as neutral species $MgCl_2(solvent)_n$, and $AlCl_4^-$ or $RAlCl_3^-$ anions. The equilibrium is affected by the Lewis base/acid ratio and the relative stability of the solvation structure.

With the $[MgCl(THF)_5]^{+}$ cation as an example, the simplified Mg deposition process is illustrated in **Figure 56** (modified from ref. 28). The properties of the cations and their interactions with the Mg surface, including the configuration of the adsorption, the binding energy of the solvation, the cathodic stability of the solvent molecules, and the fate of the deslovated solvents and chloride, all affect the Mg deposition-stripping process. In principle, the solvents used in Mg electrolytes should be inherently resistant to electrochemical reduction and oxidization. It is widely recognized that only ether solvents are suitable for Mg electrolytes due to their good cathodic stability. On the other hand, organic carbonate solvents are considered unsuitable for Mg electrolytes due to their proneness to cathodic decomposition to form a passivation layer, although the composition of such a layer has not been studied to date. The effect of the deslovated chloride (Cl^-) at the interface on the efficiency of Mg deposition-stripping is also not clear. However, it is reasonable to speculate that free Cl^- can interact with the surface species in a number of routes. For instance, free Cl^- can combine with surface-adsorbed Mg-Cl cations to form a

$MgCl_2$ rich surface layer, which may facilitate cation transport and prevent anion decomposition. On the other hand, in the presence of a trace amount of water, which is inevitable in ethereal electrolytes, free Cl^- can attack Mg metal to reduce the deposition efficiency.

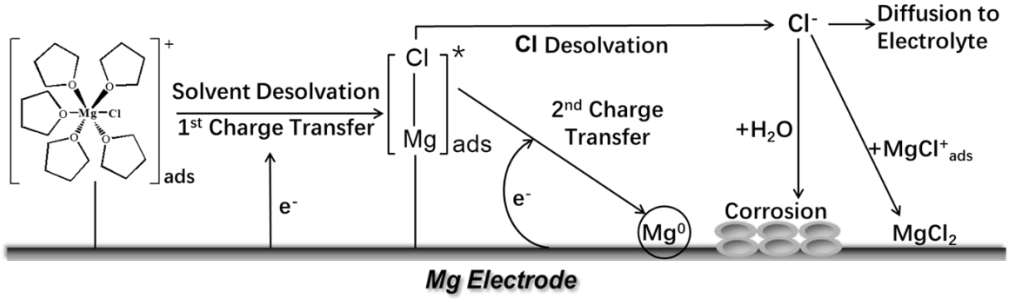

Figure 56. Illustration of the possible processes of Mg deposition from [MgCl(THF)5]+ cation. This illustration is modified from ref. 28.

The recent development of Mg electrolytes has shifted significantly to focus on the ones based on simple Mg salts with weakly coordinating anions. The composition of these electrolytes has the beauty of simplicity, containing only solvent solvated $[Mg(solvent)_n]^{2+}$ cations and the weakly coordinating anions. Thus, the mechanisms of Mg deposition-stripping and cathode reactions can be elucidated with fewer intertwined processes. The simple salt Mg electrolytes also have the potential benefits of higher Mg deposition efficiency and higher anodic stability due to the absence of active Cl^-. However, the simple salts of Mg still face steep challenges dictated by the properties of their anions. $Mg(BH_4)_2$ was the first simple salt to demonstrate reversible Mg deposition-stripping in the work of Connor and coworkers, albeit with co-deposition of boron.[2] Mohtadi and coworkers in 2012 demonstrated improved Mg deposition from $Mg(BH_4)_2$ with $Li(BH_4)_2$ as the

additive in DME.[31] However, the same study also revealed the low anodic stable window of $Mg(BH_4)_2$ at 1.5 V on platinum and 2 V on stainless steel versus Mg, which seriously limits its realistic application in batteries. Furthermore, the necessity of the addition of $LiBH_4$ indicates the relatively strong Coulombic attraction between the $[Mg(solvent)_n]^{2+}$ cation and the BH_4^- anion. It is also worthwhile to note that the deposition of Mg from the "dual ion" (Mg^{2+} + Li^+) electrolytes may take an alternative route from the direct electrochemical reduction of $[Mg(solvent)_n]^{2+}$: under high overpotential built at the interface, metallic Li can be deposited first, after which Mg will be deposited via displacement reaction. This mechanism may work in favor of Mg deposition, but its long-term effect on the interface cannot be overlooked. The displacement reaction at the Mg anode/electrolyte interface was also observed in the electrolytes containing Mg-Cl cations and chloroaluminate anions, particularly in the magnesium aluminum chloride complex (MACC) system.[32, 33] Mg was deposited first, but metallic Al was then subsequently deposited from the chloroaluminate anions by the oxidization of Mg. Such displacement at the Mg interface is clearly undesirable.

$Mg(ClO_4)_2$ is another simple salt that was studied during the early stages of Mg battery research. An interesting aspect of $Mg(ClO_4)_2$ electrolytes is that although Mg deposition is infeasible, Mg can be stripped despite an high overpotential of around 1.5 V in its ethereal solutions.[11] This suggests that the difficulty of Mg deposition originates from the properties of the $(ClO_4)^-$ anion instead of the $[Mg(solvent)_n]^{2+}$ cation. Indeed, $(ClO_4)^-$ anion can be both chemically reduced by Mg metal and

electrochemically reduced, resulting in a passivation layer on the surface of the Mg anode. Although the composition of this layer has not been investigated, one can speculate that it may contain Mg oxide. It is also believed that magnesium tetrafluoroborate ($Mg(BF_4)_2$), magnesium trifluoromethanesulfonate (($Mg(CF_3SO_3)_2$), $Mg(PF_6)_2$, and $Mg(TFSI)_2$ are all chemically and/or electrochemically unstable at the Mg surface in a similar fashion. As reported by Jay et. al, the passivation layer from $Mg(TFSI)_2$ was composed of Mg fluoride, sulfide, oxide, and sulfite/dithionite compounds from the decomposition of $TFSI^-$ anions.[34] The study by Yu et. al also suggested that the undercoordinated Mg (kinks on MgO or $Mg(OH)_2$) on the Mg surface and the water impurity in the electrolyte synergistically contributed to the chemical decomposition of the $Mg(TFSI)_2$ electrolyte in DME.[35] A number of studies have reported that adding $MgCl_2$ into the $Mg(TFSI)_2$ electrolytes can significantly reduce the overpotentials of Mg deposition-stripping and improve roundtrip efficiency.[36, 37] However, one must understand that the electrolytes containing both $Mg(TFSI)_2$ and $MgCl_2$ are not simple salt electrolytes, because the active cations are Mg-Cl monomers or dimers generated from the comproportionation simplified as the following reaction:

$$MgCl_2 + [Mg^{2+}][TFSI^-]_2 \longrightarrow 2[MgCl^+][TFSI^-]$$

What is intriguing about the $Mg(TFSI)_2$ + $MgCl_2$ electrolytes is that the electrodeposition of Mg from the Mg-Cl cations clearly alleviates the passivation from the decomposition of $TFSI^-$ anions. Although there have been no studies devoted to an explanation for this observation, certain speculations can be made: (1)

the free Cl^- released from the reduction of Mg-Cl cations in the presence of a trace amount of water may be favorable to remove the surface passivation layer such as MgO; (2) the free Cl^- may combine with the Mg-Cl cations to form a surface layer that prevents decomposition of $TFSI^-$ anion and concurrently enables the transport of Mg-containing cations to the anode surface. The second hypothesis is particularly promising and indirectly supported by observations in the literature; from 1977 to 1981, Peled and coworkers published a series of papers investigating the interphase produced on the Mg anode from the electrolyte composed of $MgCl_2$ and $FeCl_3$ or $AlCl_3$ (they are very similar to the MACC electrolytes).[38-40] They concluded that the interface was rich in $MgCl_2$ and capable of conducting cations with a transference number close to 1, meaning it is nearly a single ion conductor for Mg-containing cations. Indeed, these studies were limited by the lack of rigorous spectroscopic characterizations and may warrant re-investigation, but the concluded $MgCl_2$-rich interphase is consistent with a possible route of desolvated Cl^- at the Mg surface recombining with Mg-Cl cations to form $MgCl_2$ as shown in **Figure 56**. The latest evidence of a potential single cation conducting interphase in Mg electrolytes is from the work by Ban and coworkers, who produced an artificial interphase on Mg by mixing polyacrylonitrile and $Mg(CF_3SO_3)_2$.[41] The most intriguing property of this interphase is that it enables the use of propylene carbonate (PC) as the solvent for the $Mg(TFSI)_2$ electrolyte in the study. It apparently indicates that the PC molecules in the solvated Mg^{2+} cations, as well as the $TFSI^-$ anions, were repelled by this artificial layer. Based on these studies, a Mg-single-ion-conducting solid electrolyte

interphase (SEI) on Mg anode as illustrated in **Figure 57** can be very beneficial. In particular, its ability to enable the use of carbonate solvents, which are advantageous compared to ethers in terms of safety and anodic stability, is a great boon.

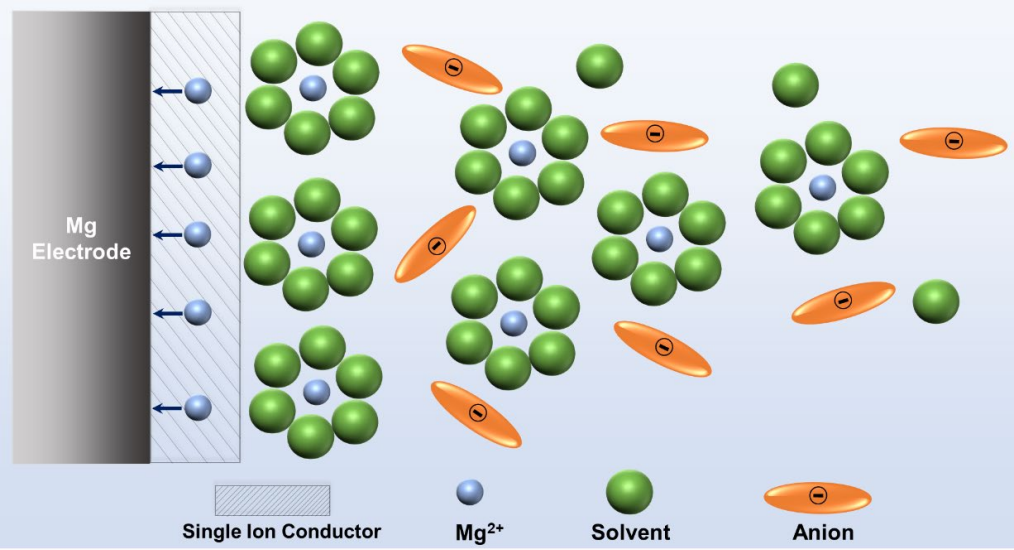

Figure 57. Illustration of an idealized single ion conducting (artificial) SEI on the Mg anode enable desolvation and screening out anions.

Recently, more simple salt Mg electrolytes using unconventional weakly coordinating anions including tetrakis(hexafluoroisopropyloxy)aluminate ($[Al(hfip)_4]^-$),[23] tetrakis(hexafluoroisopropyloxy)borate ($[B(hfip)_4]^-$),[24] icosahedral carborane ($(HCB_{11}H_{11})^-$),[26,27] and 10-vertex carborane ($(HCB_9H_9)^-$)[42] were studied. These electrolytes unambiguously demonstrated facile Mg deposition-stripping with low overpotential and high efficiency. Various cathode materials such as Mo_6S_8, TiS_2, alpha manganese dioxide (α-MnO_2), and sulfur (S) were demonstrated in these electrolytes, though with certain discrepancies and ambiguities to be discussed in a later section.

Dendrite formation and growth is the universal fear for all rechargeable batteries using metal anodes. Mg has been cited in many publications as a "dendrite-free" anode,[43] but a number of recent studies have clearly demonstrated that this is not true.[44,45] Simply, the key parameter for distinguishing dendritic and non-dendritic metal deposition is the surface current density, which determines whether the deposition is under mass transfer limitation for the Mg-containing cations. When mass transfer is not the rate-limiting step, the morphology of electrochemically deposited metal is closely related to thermodynamic and kinetic properties such as adsorption energy of ions, charge transfer activation energy, reaction rate, bond energy of the metal atoms, surface diffusion coefficient, etc. For comparison, computational modeling indicates that the deposition of Li prefers one-dimensional growth, forming wires and whiskers, while Mg is in favor of two-dimensional and three-dimensional growth as observed in most Mg deposition studies.[46] Dendritic deposition of Mg occurs under the mass transfer limitation, *i.e.*, the current is high enough to result in large concentration polarization of Mg-containing cations on the anode surface.[47] Nevertheless, studies on the morphology of Mg deposition have to consider the different governing deposition mechanisms under different current densities. Future Mg batteries required to operate under high current conditions will need to overcome the challenge raised by Mg dendrite formation.

Cathode Interface: The interfacial processes on the Mg cathode surface may be more complex than those on the anode side. However, there are few studies that have discussed the effects of cathode interfaces on the electrochemical reactions between the Mg-cathode

pairs. In fact, most of the publications on Mg cathode materials heavily emphasize the demonstration of "performance", despite the frequent failure of apparent discharge-charge and cycling performance to fully reflect the underlying mechanisms. In the electrolytes from the combination of Lewis bases and acids, one must attend to the cathode-electrolyte chemical compatibility. It is known that Grignard reagents are not compatible with certain transition metal oxides and sulfides due to their nucleophilicity, as demonstrated by Gregory and coworkers in 1990.[4] The transition metals at high oxidation state in the oxides and sulfides can be reduced by MgR_2 (where R is alkyl or phenol) species generated from the Schlenk equilibrium in the electrolytes. The same concern also applies to electrolytes using Mg-containing Lewis bases (such as ROMgCl, $Mg(OR)_2$, HMDSMgCl, and $Mg(HMDS)_2$) and Al halides Lewis acids. These electrolytes are still nucleophilic, so the chemical compatibility with the (relatively) electrophilic cathode materials must be validated. A recent study revealed the chemical reaction between vanadium pentoxide (V_2O_5) and chloroaluminate anions including $AlCl_4^-$, which is a common anion in Lewis base/acid electrolytes.[48] Iron disulfide was also reported to possibly react with chloroaluminate anions.[49] These studies have brought the chemical stability of the metal oxides and sulfides in Mg electrolytes containing $AlCl_4^-$ anions into question.

The reaction mechanisms of the cathodes, i.e., intercalation and conversion, are also affected by the structures of the Mg-containing cations. Although it is outside the focus of this paper, it is worth mentioning that there are discrepancies between reports of the intercalation-type of Mg cathodes in the literature. The diffusion of divalent Mg^{2+} in metal oxide crystal structures can be extremely difficult due to the

strong Coulombic attraction with the oxide anionic framework. Metal sulfides in principle are easier to intercalate due to the better polarizability of sulfide, but they suffer from lower intercalation potential.[50,51] Intercalation reactions are characterized by distinct changes in the crystal structures of the hosts; however, with the exception of Mo_6S_8, reports on Mg intercalation with unambiguous crystallographic evidence and mechanism elucidation are rare.[52-59] To date, Mo_6S_8 is the only Mg cathode material with a well-elucidated intercalation mechanism and high cycling stability, and it has remained as the benchmark cathode since it was first reported in 2000.[5,60] ecent studies on Mo_6S_8 as the host material for electrochemically intercalated Al further demonstrate the extraordinary ability of the Chevrel phase structure to accommodate multivalent foreign cations.[61-63] In contrast with the well-elucidated Mg^{2+} transport process inside the crystal structure of Mo_6S_8, the interface processes on the surface of Mo_6S_8 is much less clearly known. The original report of Mo_6S_8 was in the DCC electrolytes containing $[Mg_nCl_{2n-1}(solvent)_m]^+$ monomer or dimer cations. The Cl ligand in the cations played a critical role in facilitating Mg intercalation in Mo_6S_8 via a surface mechanism, revealed by Wan et. al. using a cluster model to study the properties of Mo_6S_8 (100) surface. It was found that the Mo_6S_8 (100) surface can reduce the Mg-Cl dissociation energy from ~3 eV to as low as ~0.2 eV due to the surface catalyst property granted by Mo, which could bond Cl^- anions.[64] In addition to the mechanism of Mg^{2+} intercalation via Cl desolvation, intercalation of monovalent $MgCl^+$ was also reported by Hyun et al in expanded layered TiS_2 in 0.25M APC electrolyte with 0.2M 1-butyl-1-

methylpyrrolidinium chloride additive. Both first-principles calculations and experimental results indicated favorable diffusion of $MgCl^+$ over Mg^{2+} in the expanded TiS_2 crystal structure. [65]

On the other hand, Mg cations in simple salt electrolytes, i.e., solvated divalent $[Mg(solvent)_n]^{2+}$ cations, may have distinct interfacial process from those cations containing Cl. To our best knowledge, there have been no studies devoted to comparing the interface processes between solvated simple Mg^{2+} cations and Mg-Cl complex cations. A literature survey unambiguously indicates that the discharge-charge behaviors of the benchmark Mo_6S_8 in Lewis base/acid electrolytes and simple salt electrolytes are very different. [31,66,67] In general, the magnesiation-demagnesiation curve in simple salt electrolytes has a slope or single plateau (compared to two flat plateaus in Lewis base/acid electrolytes) and lower magnesiation potential. The cycle stability in Mg simple salt electrolytes is also generally worse. This indicates that the Cl ligand helps with Mg intercalation on the Mo_6S_8 surface, which is consistent with the simulation work from Wan et. al, while the solvation of divalent Mg^{2+} cations has a negative impact on Mg intercalation. Although the interface at the Mg anode may play a role in the observed difference, understanding the potentially different desolvation processes of these two types of cations is worth pursuing.

The great advantage of simple salt Mg electrolytes is that they enable sulfur cathodes, which are not compatible with nucleophilic electrolytes. Despite the numerous reports on Mg-S batteries, the detailed reaction mechanism at the S

cathode is not well understood. The typical magnesiation curve of sulfur has two stepwise plateaus, which reassemble the lithiation curve of sulfur, although with lower potential. It is widely believed that polysulfides are produced as the intermediate products from the Mg-S reaction and that the polysulfide shuttling occurs during the charge process. This is indicated by the longer charge curve compared to the discharge curve observed in a number of studies. However, the Mg-S electrochemical reaction must be fundamentally different from that of Li-S. The work from Robba and coworkers showed differing structures between electrochemically formed MgS and chemically formed MgS, which is clear evidence for the complex nature of the reaction taking place on the sulfur cathode.[68] In addition to the effects on the cathode interface, Mg anode passivation could also shut down the reversible reaction in Mg-S batteries. Wang and coworkers demonstrated that the sluggish magnesiation of sulfur in 0.5M $MgTFSI_2$-DME electrolyte due to the Mg surface passivation could be alleviated by adding $MgCl_2$ in the electrolyte.[69,70] This observation is consistent with the speculation discussed in the Anode Interfaces Section that $MgCl_2$ can remove the Mg surface passivation layer and/or facilitate the interfacial cation transport.

To overcome the issue of polysulfides, conventional strategies succeed, to some extent, in improving cycle stability by encapsulating sulfur with porous carbon structures.[71] A systematic study by Salama and coworkers pointed out that a trace amount of polysulfide in $Mg(TFSI)_2/MgCl_2$/DME electrolyte could poison Mg anode, but reversible Mg deposition-stripping persisted until a considerable amount

of polysulfide dissolved in the electrolyte.[72] These studies imply complex interfaces in Mg-S batteries that requires thorough understanding for future development.

Interfaces in Hybrid Electrolytes: To avoid the aforementioned difficulties at the Mg cathodes, hybrid batteries composed of Mg anode and Li^+ ion cathodes have been proposed and studied. The first Mg-Li hybrid system can be traced back to 2006, when Gofer et al. studied tetrabutylamonium (TBA^+) chloride and lithium chloride (LiCl) as additives in DCC electrolytes to improve the ionic conductivity.[73] The solubilities of TBACl and LiCl were higher in DCC electrolyte than in pure THF, indicating the formation of new species with DCC. More interestingly, co-intercalation of Li^+ in Mo_6S_8 cathode was observed in the 0.25 M DCC electrolyte with a very small amount of LiCl (0.01 M). The intercalation of both Mg^{2+} and Li^+ has opened up opportunities for hybrid batteries in which Li-hosting cathodes may be feasible. The mechanism of co-intercalation was later verified by several independent studies. It was found that the feasibility of Li^+ intercalation from a Mg-Li hybrid electrolyte is closely related to the Li^+ activity in the electrolyte. Cheng et al. studied the intercalation of Mo_6S_8 in Mg electrolytes with a much higher Li^+ ion concentration (1.0 M LiCl in in 0.4 M APC) than that of Gofer's study.[74] Instead of co-intercalation of Li^+ and Mg^{2+}, the authors found that only Li^+ was intercalated into Mo_6S_8. They concluded that to ensure exclusive intercalation of Li, the amount of Li^+ in the electrolyte must be much greater than the amount required to fully lithiate Mo_6S_8. Cho and coworkers reached a similar conclusion by calculating the ion activity using methods based on density functional theory. [75] Based on their calculation, a threshold of Li^+ activity must be achieved for Mo_6S_8 to prefer lithiation instead of magnesiation. Furthermore, the Li^+ ion activity

should be maintained as high as 1 during the cycling to fully suppress magnesiation. In addition to Mo_6S_8, TiS_2 has also been studied as the cathode in hybrid systems. Yao and coworkers observed sole intercalation of Li in TiS_2 in 0.25M APC electrolyte with 0.5M LiCl as the additive.[76] Similar results were also obtained by Wang and coworkers using 0.4M APC electrolyte with 0.4M LiCl.[77] Conventional Li transition metal oxide cathodes would be ideal for Mg-Li hybrid systems in terms of energy density, but the intrinsically low anodic stability of Mg electrolyte (due to the ethereal solvents) prohibits the use of high potential cathodes such as $LiCoO_2$ and $LiNi_xMn_yCo_{(1-x-y)}O_2$. Yagi et al. demonstrated a Mg-Li hybrid cell using $LiFePO_4$ cathode in a dual-salt THF electrolyte containing 1.0 M PhMgCl, 0.20 M $AlCl_3$, and 0.20 M $LiBF_4$. However, due to the incompatibility between PhMgCl and $LiBF_4$, the full cell performance suffered from low coulombic efficiency.[78] The idea of a hybrid Mg-Li system was also studied using conversion-type sulfur cathodes. Gao et al. demonstrated improvement of the electrochemical reduction kinetics of sulfur cathodes by adding LiTFSI into the $Mg(HMDS)_2$-based Mg electrolyte.[79]

Based on the research discussed above, a Mg-Li hybrid battery is theoretically feasible through the use of Mg anode and Li cathodes. However, the disadvantage and challenges of hybrid cells should be taken into consideration. The complex nature of the hybrid electrolytes makes the mechanism of reactions and interfacial behaviors even more complicated.

Conclusions: Ultimately, there are no benchmark electrolytes for rechargeable Mg batteries to date. Interfacial processes vary significantly in different electrolytes and are still in need of more thorough understanding. The electrolytes containing both Mg-Cl

complex cations and chloroaluminate anions are clearly problematic. This is mainly due to the chloroaluminate anions, which are chemically corrosive in the presence of water impurity. Moreover, their corrosiveness can be anodically enhanced, thus limiting the electrochemical window of these electrolytes and undermining battery performance. In comparison, electrolytes containing Mg-Cl complex cations and weakly coordinating anions such as the $Mg(TFSI)_2/MgCl_2$ system can be advantageous due to the absence of anions prone to oxidation and the improved Mg anode interface alleviating $TFSI^-$ anion reduction. The electrolytes based on simple Mg salts are conceptually superior, but the (electro)chemical instability of their anions under reducing conditions is a challenge. The stable weakly coordinating anions are often associated with sophisticated synthetic processes. In addition, the effects of the solvated divalent Mg^{2+} cations at the interface of cathodes, particularly intercalation-type materials represented by Mo_6S_8, may be disadvantageous in comparison to those of Mg-Cl complex cations. Simple salt Mg electrolytes with weakly coordinating anions are also feasible for Mg-S batteries in theory, but the electrochemical characterizations in the literature suggest a current lack of fundamental understanding.

References

1 Gaddum, L.W. and French, H.E., 1927. The electrolysis of grignard solutions1. Journal of the American Chemical Society, 49(5), pp.1295-1299.

2 Connor, J.H., Reid, W.E. and Wood, G.B., 1957. Electrodeposition of metals from organic solutions: V. electrodeposition of magnesium and magnesium alloys. Journal of The Electrochemical Society, 104(1), p.38.

3 Brenner, A., 1971. Note on the Electrodeposition of Magnesium from an Organic Solution of a Magnesium-Boron Complex. *Journal of The Electrochemical Society*, *118*(1), p.99.

4 Gregory, T.D., Hoffman, R.J. and Winterton, R.C., 1990. Nonaqueous electrochemistry of magnesium: applications to energy storage. *Journal of the Electrochemical Society*, *137*(3), p.775.

5 Aurbach, D., Lu, Z., Schechter, A., Gofer, Y., Gizbar, H., Turgeman, R., Cohen, Y., Moshkovich, M. and Levi, E., 2000. Prototype systems for rechargeable magnesium batteries. *Nature*, *407*(6805), pp.724-727.

6 Aurbach, D., Gizbar, H., Schechter, A., Chusid, O., Gottlieb, H.E., Gofer, Y. and Goldberg, I., 2001. Electrolyte solutions for rechargeable magnesium batteries based on organomagnesium chloroaluminate complexes. *Journal of the Electrochemical Society*, *149*(2), p.A115.

7 Wan, L.F. and Prendergast, D., 2014. The solvation structure of Mg ions in dichloro complex solutions from first-principles molecular dynamics and simulated X-ray absorption spectra. *Journal of the American Chemical Society*, *136*(41), pp.14456-14464.

8 Gizbar, H., Vestfrid, Y., Chusid, O., Gofer, Y., Gottlieb, H.E., Marks, V. and Aurbach, D., 2004. Alkyl group transmetalation reactions in electrolytic solutions studied by multinuclear NMR. *Organometallics*, *23*(16), pp.3826-3831.

9 Vestfried, Y., Chusid, O., Goffer, Y., Aped, P. and Aurbach, D., 2007. Structural analysis of electrolyte solutions comprising magnesium− aluminate chloro− organic complexes by Raman spectroscopy. *Organometallics*, *26*(13), pp.3130-3137.

10 Pour, N., Gofer, Y., Major, D.T. and Aurbach, D., 2011. Structural analysis of electrolyte solutions for rechargeable Mg batteries by stereoscopic means and DFT calculations. *Journal of the American Chemical Society*, *133*(16), pp.6270-6278.

11 Lu, Z., Schechter, A., Moshkovich, M. and Aurbach, D., 1999. On the electrochemical behavior of magnesium electrodes in polar aprotic electrolyte solutions. *Journal of Electroanalytical Chemistry*, *466*(2), pp.203-217.

12 Gofer, Y., Chusid, O., Gizbar, H., Viestfrid, Y., Gottlieb, H.E., Marks, V. and Aurbach, D., 2006. Improved electrolyte solutions for rechargeable magnesium batteries. *Electrochemical and Solid-State Letters*, *9*(5), p.A257.

13 Wang, F.F., Guo, Y.S., Yang, J., Nuli, Y. and Hirano, S.I., 2012. A novel electrolyte system without a Grignard reagent for rechargeable magnesium batteries. *Chemical Communications*, *48*(87), pp.10763-10765.

14 Nelson, E.G., Kampf, J.W. and Bartlett, B.M., 2014. Enhanced oxidative stability of non-Grignard magnesium electrolytes through ligand modification. *Chemical Communications*, *50*(40), pp.5193-5195.

15 Crowe, A.J., Stringham, K.K. and Bartlett, B.M., 2016. Fluorinated alkoxide-based magnesium-ion battery electrolytes that demonstrate Li-ion-battery-like high anodic stability and solution conductivity. *ACS Applied Materials & Interfaces*, *8*(35), pp.23060-23065.

16 Liao, C., Sa, N., Key, B., Burrell, A.K., Cheng, L., Curtiss, L.A., Vaughey, J.T., Woo, J.J., Hu, L., Pan, B. and Zhang, Z., 2015. The unexpected discovery of the Mg (HMDS) 2/MgCl 2 complex as a magnesium electrolyte for rechargeable magnesium batteries. *Journal of Materials Chemistry A*, *3*(11), pp.6082-6087.

17 Kim, H.S., Arthur, T.S., Allred, G.D., Zajicek, J., Newman, J.G., Rodnyansky, A.E., Oliver, A.G., Boggess, W.C. and Muldoon, J., 2011. Structure and compatibility of a magnesium electrolyte with a sulphur cathode. *Nature communications*, *2*(1), pp.1-6.

18 Zhao, X., Zhao, Z. and Miao, Y., 2018. Chloride ion-doped polypyrrole nanocomposite as cathode material for rechargeable magnesium battery. *Materials Research Bulletin*, *101*, pp.1-5.

19 Merrill, L.C., Ford, H.O. and Schaefer, J.L., 2019. Application of single-ion conducting gel polymer electrolytes in magnesium batteries. *ACS Applied Energy Materials*, *2*(9), pp.6355-6363.

20 Keyzer, E.N., Glass, H.F., Liu, Z., Bayley, P.M., Dutton, S.E., Grey, C.P. and Wright, D.S., 2016. Mg (PF6) 2-based electrolyte systems: understanding electrolyte–electrode interactions for the development of mg-ion batteries. *Journal of the American Chemical Society*, *138*(28), pp.8682-8685.

21 Tran, T.T., Lamanna, W.M. and Obrovac, M.N., 2012. Evaluation of Mg [N (SO2CF3) 2] 2/acetonitrile electrolyte for use in Mg-ion cells. *Journal of the Electrochemical Society*, *159*(12), p.A2005.

22 Zhao-Karger, Z., Bardaji, M.E.G., Fuhr, O. and Fichtner, M., 2017. A new class of non-corrosive, highly efficient electrolytes for rechargeable magnesium batteries. *Journal of Materials Chemistry A*, *5*(22), pp.10815-10820.

23 Herb, J.T., Nist-Lund, C.A. and Arnold, C.B., 2016. A fluorinated alkoxyaluminate electrolyte for magnesium-ion batteries. *ACS Energy Letters*, *1*(6), pp.1227-1232.

24 Herb, J.T., Nist-Lund, C.A. and Arnold, C.B., 2017. A fluorinated dialkoxide-based magnesium-ion electrolyte. *Journal of Materials Chemistry A*, *5*(17), pp.7801-7805.

25 Keyzer, E.N., Lee, J., Liu, Z., Bond, A.D., Wright, D.S. and Grey, C.P., 2019. A general synthetic methodology to access magnesium aluminate electrolyte systems for Mg batteries. *Journal of Materials Chemistry A*, *7*(6), pp.2677-2685.

26 Tutusaus, O., Mohtadi, R., Arthur, T.S., Mizuno, F., Nelson, E.G. and Sevryugina, Y.V., 2015. An efficient halogen-free electrolyte for use in rechargeable magnesium batteries. *Angewandte Chemie*, *127*(27), pp.8011-8015.

27 McArthur, S.G., Geng, L., Guo, J. and Lavallo, V., 2015. Cation reduction and comproportionation as novel strategies to produce high voltage, halide free, carborane based electrolytes for rechargeable Mg batteries. *Inorganic Chemistry Frontiers*, *2*(12), pp.1101-1104.

28 Yoo, H.D., Shterenberg, I., Gofer, Y., Gershinsky, G., Pour, N. and Aurbach, D., 2013. Mg rechargeable batteries: an on-going challenge. *Energy & Environmental Science*, *6*(8), pp.2265-2279.

29 Cheng, Y., Stolley, R.M., Han, K.S., Shao, Y., Arey, B.W., Washton, N.M., Mueller, K.T., Helm, M.L., Sprenkle, V.L., Liu, J. and Li, G., 2015. Highly active electrolytes for rechargeable Mg batteries based on a [Mg 2 (μ-Cl) 2] 2+ cation complex in dimethoxyethane. *Physical Chemistry Chemical Physics*, *17*(20), pp.13307-13314.

30 Nakayama, Y., Kudo, Y., Oki, H., Yamamoto, K., Kitajima, Y. and Noda, K., 2008. Complex structures and electrochemical properties of magnesium electrolytes. *Journal of the Electrochemical Society*, *155*(10), p.A754.

31 Mohtadi, R., Matsui, M., Arthur, T.S. and Hwang, S.J., 2012. Magnesium borohydride: from hydrogen storage to magnesium battery. *Angewandte Chemie*, *124*(39), pp.9918-9921.

32 Doe, R.E., Han, R., Hwang, J., Gmitter, A.J., Shterenberg, I., Yoo, H.D., Pour, N. and Aurbach, D., 2014. Novel, electrolyte solutions comprising fully inorganic salts with high anodic stability for rechargeable magnesium batteries. *Chemical Communications*, *50*(2), pp.243-245.

33 Liu, T., Shao, Y., Li, G., Gu, M., Hu, J., Xu, S., Nie, Z., Chen, X., Wang, C. and Liu, J., 2014. A facile approach using MgCl 2 to formulate high performance Mg 2+ electrolytes for rechargeable Mg batteries. *Journal of Materials Chemistry A*, *2*(10), pp.3430-3438.

34 Jay, R., Tomich, A.W., Zhang, J., Zhao, Y., De Gorostiza, A., Lavallo, V. and Guo, J., 2019. Comparative study of Mg (CB11H12) 2 and Mg (TFSI) 2 at the magnesium/electrolyte interface. *ACS Applied Materials & Interfaces*, *11*(12), pp.11414-11420.

35 Yu, Y., Baskin, A., Valero-Vidal, C., Hahn, N.T., Liu, Q., Zavadil, K.R., Eichhorn, B.W., Prendergast, D. and Crumlin, E.J., 2017. Instability at the electrode/electrolyte interface induced by hard cation chelation and nucleophilic attack. *Chemistry of Materials*, *29*(19), pp.8504-8512.

36 Tran, T.T., Lamanna, W.M. and Obrovac, M.N., 2012. Evaluation of Mg [N (SO2CF3) 2] 2/acetonitrile electrolyte for use in Mg-ion cells. *Journal of the Electrochemical Society*, *159*(12), p.A2005.

37 Sa, N., Pan, B., Saha-Shah, A., Hubaud, A.A., Vaughey, J.T., Baker, L.A., Liao, C. and Burrell, A.K., 2016. Role of chloride for a simple, non-grignard Mg electrolyte in ether-based solvents. *ACS Applied Materials & Interfaces*, *8*(25), pp.16002-16008.

38 Peled, E. and Straze, H., 1977. The kinetics of the magnesium electrode in thionyl chloride solutions. *Journal of The Electrochemical Society*, *124*(7), p.1030.

39 Peled, E., 1979. The electrochemical behavior of alkali and alkaline earth metals in nonaqueous battery systems—the solid electrolyte interphase model. *Journal of The Electrochemical Society*, *126*(12), p.2047.

40 Meitav, A. and Peled, E., 1981. Solid Electrolyte Interphase (SEI) Electrode: II. The Formation and Properties of the SEI on Magnesium in Solutions. *Journal of The Electrochemical Society*, *128*(4), p.825.

41 Son, S.B., Gao, T., Harvey, S.P., Steirer, K.X., Stokes, A., Norman, A., Wang, C., Cresce, A., Xu, K. and Ban, C., 2018. An artificial interphase enables

reversible magnesium chemistry in carbonate electrolytes. *Nature Chemistry*, *10*(5), pp.532-539.

42 McArthur, S.G., Jay, R., Geng, L., Guo, J. and Lavallo, V., 2017. Below the 12-vertex: 10-vertex carborane anions as non-corrosive, halide free, electrolytes for rechargeable Mg batteries. *Chemical Communications*, *53*(32), pp.4453-4456.

43 Matsui, M., 2011. Study on electrochemically deposited Mg metal. *Journal of Power Sources*, *196*(16), pp.7048-7055.

44 Ding, M.S., Diemant, T., Behm, R.J., Passerini, S. and Giffin, G.A., 2018. Dendrite growth in Mg metal cells containing Mg (TFSI) 2/glyme electrolytes. *Journal of The Electrochemical Society*, *165*(10), p.A1983.

45 Davidson, R., Verma, A., Santos, D., Hao, F., Fincher, C.D., Zhao, D., Attari, V., Schofield, P., Van Buskirk, J., Fraticelli-Cartagena, A. and Alivio, T.E., 2020. Mapping mechanisms and growth regimes of magnesium electrodeposition at high current densities. *Materials Horizons*, *7*(3), pp.843-854.

46 Aryanfar, A., Brooks, D.J., Colussi, A.J., Merinov, B.V., Goddard III, W.A. and Hoffmann, M.R., 2015. Thermal relaxation of lithium dendrites. *Physical Chemistry Chemical Physics*, *17*(12), pp.8000-8005.

47 Brissot, C., Rosso, M., Chazalviel, J.N. and Lascaud, S., 1999. Dendritic growth mechanisms in lithium/polymer cells. *Journal of power sources*, *81*, pp.925-929.

48 Shi, J., Zhang, J., Guo, J. and Lu, J., 2020. Interfaces in rechargeable magnesium batteries. *Nanoscale Horizons*, *5*(11), pp.1467-1475.

49 Mori, T., Orikasa, Y., Nakanishi, K., Kezheng, C., Hattori, M., Ohta, T. and Uchimoto, Y., 2016. Discharge/charge reaction mechanisms of FeS2 cathode material for aluminum rechargeable batteries at 55° C. *Journal of Power Sources*, *313*, pp.9-14.

50 Levi, E., Levi, M.D., Chasid, O. and Aurbach, D., 2009. A review on the problems of the solid state ions diffusion in cathodes for rechargeable Mg batteries. *Journal of Electroceramics*, *22*(1), pp.13-19.

51 Heath, J., Chen, H. and Islam, M.S., 2017. MgFeSiO 4 as a potential cathode material for magnesium batteries: ion diffusion rates and voltage trends. *Journal of Materials Chemistry A*, *5*(25), pp.13161-13167.

52 E. Levi, E. Lancry, A. Mitelman, D. Aurbach, G. Ceder, D. Morgan and O. Isnard, *Chem. Mater.*, 2006, **18**, 5492-5503.

53 E. Levi, E. Lancry, A. Mitelman, D. Aurbach, O. Isnard and D. Djurado, *Chem. Mater.*, 2006, **18**, 3705-3714.

54 Levi, E., Mitelman, A., Aurbach, D. and Brunelli, M., 2007. Structural mechanism of the phase transitions in the Mg− Cu− Mo6S8 system probed by ex Situ synchrotron X-ray diffraction. *Chemistry of Materials*, *19*(21), pp.5131-5142.

55 Levi, E., Mitelman, A., Isnard, O., Brunelli, M. and Aurbach, D., 2008. Phase Diagram of Mg Insertion into Chevrel Phases, Mg x Mo6T8 (T= S, Se). 3. The Crystal Structure of Triclinic Mg2Mo6Se8. *Inorganic chemistry*, *47*(6), pp.1975-1983.

56 Bonnick, P., Blanc, L., Vajargah, S.H., Lee, C.W., Sun, X., Balasubramanian, M. and Nazar, L.F., 2018. Insights into Mg2+ intercalation in a zero-strain material: thiospinel Mg x Zr2S4. *Chemistry of Materials*, *30*(14), pp.4683-4693.

57 Bonnick, P., Blanc, L., Vajargah, S.H., Lee, C.W., Sun, X., Balasubramanian, M. and Nazar, L.F., 2018. Insights into Mg2+ intercalation in a zero-strain material: thiospinel Mg x Zr2S4. Chemistry of Materials, 30(14), pp.4683-4693.

58 Sa, N., Mukherjee, A., Han, B., Ren, Y., Klie, R.F., Key, B. and Vaughey, J.T., 2019. Direct observation of MgO formation at cathode electrolyte interface of a spinel MgCo2O4 cathode upon electrochemical Mg removal and insertion. *Journal of Power Sources*, *424*, pp.68-75.

59 Andrews, J.L., Mukherjee, A., Yoo, H.D., Parija, A., Marley, P.M., Fakra, S., Prendergast, D., Cabana, J., Klie, R.F. and Banerjee, S., 2018. Reversible Mg-ion insertion in a metastable one-dimensional polymorph of V2O5. *Chem*, *4*(3), pp.564-585.

60 Ling, C. and Suto, K., 2017. Thermodynamic origin of irreversible magnesium trapping in chevrel phase Mo6S8: importance of magnesium and vacancy ordering. *Chemistry of Materials*, *29*(8), pp.3731-3739.

61 Walter, M., Kovalenko, M.V. and Kravchyk, K.V., 2020. Challenges and benefits of post-lithium-ion batteries. *New Journal of Chemistry*, *44*(5), pp.1677-1683.

62 Gao, K., Lin, X., Yu, W., Cheng, X., Zhang, S., Li, S. and Zhang, Z., 2022. Few-Layered ReS2@ CNTs as a High-Performance Cathode for Aluminum-Ion Batteries. *Advanced Materials Interfaces*, p.2200635.

63 Lee, B., Lee, H.R., Yim, T., Kim, J.H., Lee, J.G., Chung, K.Y., Cho, B.W. and Oh, S.H., 2016. Investigation on the structural evolutions during the insertion of aluminum ions into Mo6S8 Chevrel phase. *Journal of The Electrochemical Society*, *163*(6), p.A1070.

64 Heath, J., Chen, H. and Islam, M.S., 2017. MgFeSiO 4 as a potential cathode material for magnesium batteries: ion diffusion rates and voltage trends. *Journal of Materials Chemistry A*, *5*(25), pp.13161-13167.

65 Wang, Y., Wang, C., Yi, X., Hu, Y., Wang, L., Ma, L., Zhu, G., Chen, T. and Jin, Z., 2019. Hybrid Mg/Li-ion batteries enabled by Mg2+/Li+ co-intercalation in VS4 nanodendrites. *Energy Storage Materials*, *23*, pp.741-748.

66 You, C., Wu, X., Yuan, X., Chen, Y., Liu, L., Zhu, Y., Fu, L., Wu, Y., Guo, Y.G. and van Ree, T., 2020. Advances in rechargeable Mg batteries. *Journal of Materials Chemistry A*, *8*(48), pp.25601-25625.

67 Tuerxun, F., Abulizi, Y., NuLi, Y., Su, S., Yang, J. and Wang, J., 2015. High concentration magnesium borohydride/tetraglyme electrolyte for rechargeable magnesium batteries. *Journal of Power Sources*, *276*, pp.255-261.

68 Robba, A., Mežnar, M., Vizintin, A., Bitenc, J., Bobnar, J., Arčon, I., Randon-Vitanova, A. and Dominko, R., 2020. Role of Cu current collector on electrochemical mechanism of Mg–S battery. *Journal of power sources*, *450*, p.227672.

69 Hu, X.C., Shi, Y., Lang, S.Y., Zhang, X., Gu, L., Guo, Y.G., Wen, R. and Wan, L.J., 2018. Direct insights into the electrochemical processes at anode/electrolyte interfaces in magnesium-sulfur batteries. *Nano Energy*, *49*, pp.453-459.

70 Gao, T., Hou, S., Wang, F., Ma, Z., Li, X., Xu, K. and Wang, C., 2017. Reversible S0/MgSx redox chemistry in a MgTFSI2/MgCl2/DME electrolyte for rechargeable Mg/S batteries. *Angewandte Chemie*, *129*(43), pp.13711-13715.

71 Yu, X. and Manthiram, A., 2016. Performance enhancement and mechanistic studies of magnesium–sulfur cells with an advanced cathode structure. *ACS Energy Letters*, *1*(2), pp.431-437.

72 Salama, M., Attias, R., Hirsch, B., Yemini, R., Gofer, Y., Noked, M. and Aurbach, D., 2018. On the feasibility of practical Mg–S batteries: practical limitations associated with metallic magnesium anodes. *ACS applied materials & interfaces*, *10*(43), pp.36910-36917.

73 Gofer, Y., Chusid, O., Gizbar, H., Viestfrid, Y., Gottlieb, H.E., Marks, V. and Aurbach, D., 2006. Improved electrolyte solutions for rechargeable magnesium batteries. *Electrochemical and Solid-State Letters*, *9*(5), p.A257.

74 Cheng, Y., Shao, Y., Zhang, J.G., Sprenkle, V.L., Liu, J. and Li, G., 2014. High performance batteries based on hybrid magnesium and lithium chemistry. *Chemical communications*, *50*(68), pp.9644-9646.

75 Cho, J.H., Aykol, M., Kim, S., Ha, J.H., Wolverton, C., Chung, K.Y., Kim, K.B. and Cho, B.W., 2014. Controlling the intercalation chemistry to design high-performance dual-salt hybrid rechargeable batteries. *Journal of the American Chemical Society*, *136*(46), pp.16116-16119.

76 Yoo, H.D., Liang, Y., Li, Y. and Yao, Y., 2015. High areal capacity hybrid magnesium–lithium-ion battery with 99.9% coulombic efficiency for large-scale energy storage. *ACS Applied Materials & Interfaces*, *7*(12), pp.7001-7007.

77 Gao, T., Han, F., Zhu, Y., Suo, L., Luo, C., Xu, K. and Wang, C., 2015. Hybrid Mg2+/Li+ battery with long cycle life and high rate capability. *Advanced Energy Materials*, *5*(5), p.1401507.

78 Yagi, S., Ichitsubo, T., Shirai, Y., Yanai, S., Doi, T., Murase, K. and Matsubara, E., 2014. A concept of dual-salt polyvalent-metal storage battery. *Journal of Materials Chemistry A*, *2*(4), pp.1144-1149.

79 Gao, T., Noked, M., Pearse, A.J., Gillette, E., Fan, X., Zhu, Y., Luo, C., Suo, L., Schroeder, M.A., Xu, K. and Lee, S.B., 2015. Enhancing the reversibility of Mg/S battery chemistry through Li+ mediation. *Journal of the American Chemical Society*, *137*(38), pp.12388-12393.

4.3 Aluminum batteries

Rechargeable aluminum (Al) batteries have become an attractive topic in recent years driven by the quest for battery technologies beyond lithium. Al has excellent theoretical specific capacity (2980 mAh g^{-1}) and volumetric capacity (8040 mAh cm^{-3}) as a battery

anode, although high-voltage Al batteries can be difficult to achieve due to its relatively high anodic potential. A typical rechargeable Al battery is composed of an Al metal anode, a deep eutectic solvent electrolyte, and a cathode capable of reversible electrochemical reaction with the Al-containing species in the electrolyte. Al metal is likely the only viable choice as the anode. Therefore, the electrochemical reaction at the anode is reversible Al deposition-stripping. To date, the only (without ambiguity) electrolytes that can facilely enable Al deposition-stripping at room temperature are deep eutectic solvents composed of aluminum halides (aluminum chloride $AlCl_3$ or aluminum bromide $AlBr_3$) and the corresponding halides with organic cations such as imidazolium, pyridinium and ammonium.[1] The discovery of this type of electrolyte is attributed to the electrodeposition community in the pursuit of the electrochemical plating of Al.[2, 3] It is well known that only a Lewis acidic electrolyte, in which the molar ratio between $AlCl_3$ (or $AlBr_3$) and organic halide is higher than 1, can reversibly deposit and strip Al. The active species responsible for Al deposition is the Lewis acidic chloroaluminate anion $Al_2Cl_7^-$.[3] The other major chloroaluminate anion existing in the electrolyte is $AlCl_4^-$, which is not active in Al deposition. On the other hand, it is known to be prone to electrochemical oxidation to evolve chlorine (Cl_2).[3] $AlCl_4^-$ also is reported to be capable of intercalating into the layers of graphitic carbons,[4, 5] which have attracted significant attention as the cathode material in rechargeable Al batteries.

Although there have been a few studies reporting new Al electrolyte systems,[6-9] due to the readiness of (or a lack of alternatives to) the deep eutectic electrolytes, current Al battery investigations are mainly focused on cathode materials. The performance of some

representative cathode materials for rechargeable Al batteries is compared in the Supporting Information. The deep eutectic chloroaluminate electrolytes play an essential role in cathode material investigations, but it is also extremely important to understand the interference and even misleading results caused by their use. The problems of the chloroaluminate electrolytes originate from their intrinsic properties: low anodic stability, *i.e.*, generation of chlorine or other active side products during charge, and electrochemically-enhanced corrosivity. Investigators must carefully design and execute the experiments as well as rigorously interpret the data to obtain the true results. In the following sections, we discuss some pitfalls that may be overlooked in rechargeable Al battery research as illustrated in **Figure 58**.

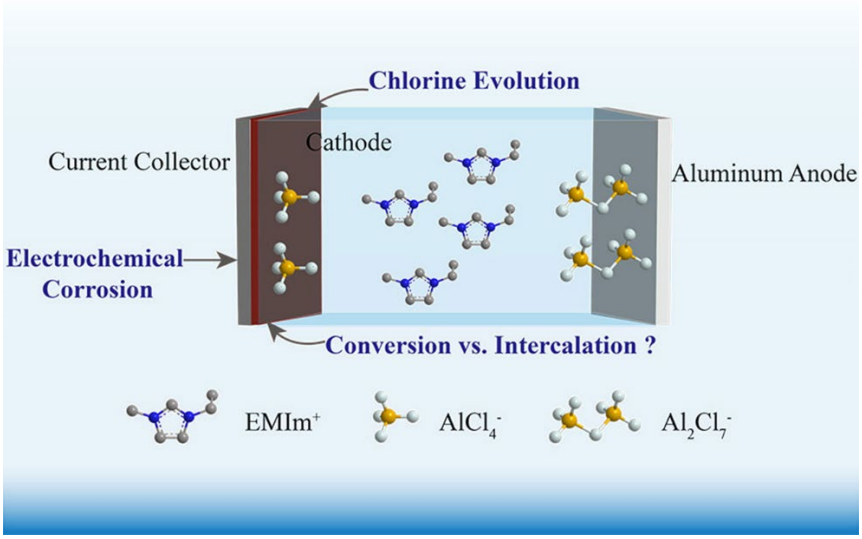

Figure 58. Illustration of the potential issues overlooked in rechargeable aluminum battery research.

Material Preparation. 1-Ethyl-3-methylimidazolium chloride ([EMIm]Cl, 98%, TCI AMERICA) was dried under vacuum at 60 °C for at least 24 hours in an argon-fill

glovebox. Aluminum chloride ($AlCl_3$, 99.99%, Sigma-Aldrich) was received sealed in an ampule, and it was used as purchased. The Lewis acidic electrolyte ($AlCl_3$:[EMIm]Cl in a molar ratio of 1.3:1) was prepared by slowly mixing the solid [EMIm]Cl with anhydrous $AlCl_3$. Glassy carbon rods (6 mm in diameter and 50 mm in length) were purchased from Tokai Carbon USA, Inc. as the electrodes in the Swagelok-type cells. Aluminum foil (0.2 mm thick, 99.997%, Alfa Aesar), titanium foil (0.025mm thick, 99.6%, STREM CHEMICALS, INC.), molybdenum foil (0.025mm thick, 99.95%, Alfa Aesar), nickel foil (0.025mm thick, 99.99%, Alfa Aesar), tungsten foil (0.05mm thick, 99.95%, Alfa Aesar), and platinum foil (0.025mm thick, 99.9%, Sigma-Aldrich) were first polished with 2500 grit SiC sandpaper, then rinsed with tetrahydrofuran in an argon-filled glovebox, and finally dried at 130 °C before use. Glassy carbon rods were first polished with a polishing cloth soaked with 0.05 μm Al_2O_3 particles in suspension, then rinsed with DI water and anhydrous acetone, then dried at 100 °C in the argon-filled glovebox. All Swagelok-type cell parts were washed with acetone and stored under vacuum at 50 °C before use. Cotton wool, synthetic graphite carbon paper (0.127mm thick, Spectracarb 2050A-0550, purchased from FuelCellStore), polystyrene (Mw ~ 350,000, Sigma-Aldrich), and natural graphite (Sigma-Aldrich) were all dried at 80 °C under vacuum before use. Ketjen black EC-600JD (Carbon Black, purchased from AkzoNobel) was treated via hydrogen reduction under a hydrogen/argon (5 vol.%/95 vol.%) environment at 1000 °C for 3 hours to remove oxygen-containing groups.

Electrochemical Measurements. All electrochemical measurements were carried out in lab-designed Swagelok-type cells as shown in **Figure 59**. Galvanostatic measurements

were carried out at an Arbin battery test station. Cyclic voltammetry (CV) was carried out with a Gamry potentiostat (Reference 1000). To prepare the natural graphite electrodes, natural graphite was mixed with polystrene with a weight ratio of 9:1 in N-methyl-2-pyrrolidone. The obtained slurry was uniformly pasted onto molybdenum foil, which was first dried in ambient environment and then further dried at 135 °C under vacuum in the argon-filled glovebox for at least 12 hours. Carbon paper was directly used as the synthetic graphite carbon electrode. The carbon black electrode was prepared with the same procedure as the natural graphite was, with a 1:1 weight ratio of carbon black to polystyrene. In all of the electrochemical experiments, 10 mg of dried cotton wool was used as the separator soaked in 150 μL electrolyte. The average area loading of active material on the carbon electrodes was 3.5 mg cm^{-2} for natural graphite, 7.0 mg cm^{-2} for synthetic graphite, and 1.8 mg cm^{-2} for carbon black.

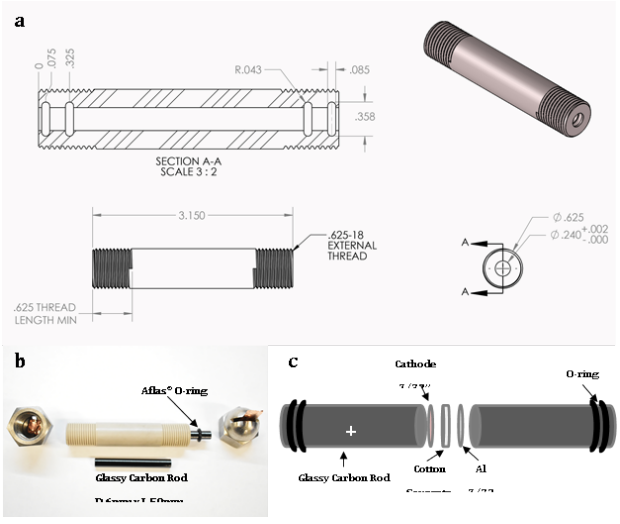

Figure 59. (a) Drawing of Swagelok-type cell used in this study; (b) Digital picture of a Swagelok-type cell with its parts; (c) Schematic illustration of assembly of a Swagelok-type cell.

Selection of Current Collectors: Selecting suitable cathode current collectors is of fundamental importance because most of the studied metals can be (electrochemically) corroded in deep eutectic chloroaluminate electrolytes, and the corrosive current can be mistaken as the current from battery reactions, as demonstrated by Reed and Menke in the case of stainless steel.[10] To demonstrate the importance of a suitable current collector, the electrochemical properties of a number of conductive substrates were analyzed in a representative deep eutectic electrolyte composed of $AlCl_3$ and 1-ethyl-3-methylimidazolium chloride ([EMIm]Cl) with a molar ratio of 1.3:1. The electrolyte was prepared by mixing ultrapure anhydrous $AlCl_3$ with [EMIm]Cl, both of which were first dried at elevated temperature under vacuum for 24 hours in argon-filled glovebox. A thoroughly polished Al foil was used as the anode, a piece of dried cotton wool soaked with the electrolyte was used as the separator, and the cathode was the bare current collector being tested. To eliminate potential interference, customized Swagelok-type cells with polyether ether ketone (PEEK) bodies and glassy carbon (GC) rods electrodes were used. Polytetrafluoroethylene (PTFE) was not selected for the cell body due to our previous finding that fluorinated polymers may not be electrochemically inert in the deep eutectic chloroaluminate electrolyte.[11] The entire Swagelok cell contained no metal parts in contact with the electrolyte. The drawing and the digital image of the Swagelok-type cell and the experimental details can be found in the Supporting Information.

Figure 60 shows the galvanostatic reduction and oxidation of the current collectors, denoted as discharge and charge respectively, to be consistent with battery study. The corresponding cyclic voltammetry (CV) analyses are shown in the Supporting Information.

The galvanostatic experiments started with a discharge current of 1.78×10^{-2} mA cm^{-2}. All current collectors except GC and molybdenum (Mo) show a short discharge potential curve for approximately two hours before reaching the cutoff potential at 0.3 V versus Al. If we assume the areal loading of the material of interest was 1 mg cm^{-2}, the artificial "capacity" from the first discharge would be around 35 mAh g^{-1} even the material is completely inert. This false capacity may be related to the native oxide layer on the surface of the metal substrates and the cathodic decomposition of the electrolyte. It is also worth noting that this artificial discharge capacity is very sensitive to the moisture content of the electrolyte. As shown in the Supporting Information, the discharge curve is much longer on the GC surface in an $AlCl_3$-[EMIm]Cl electrolyte not dried under vacuum. The side reaction could be the electrochemical reduction of water to produce hydrogen and hydroxyl anions. The cathodic decomposition of the deep eutectic chloroaluminate electrolytes is worth thorough investigation.

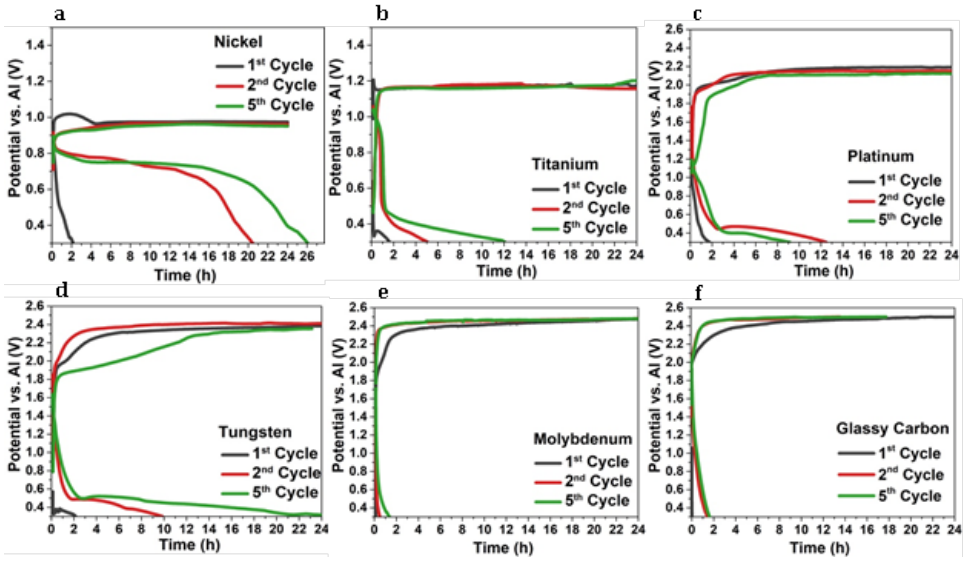

Figure 60. The galvanostatic discharge-charge (reduction-oxidation) curves of various conductive substrates including (a) nickel, (b) titanium, (c) platinum, (d) tungsten, (e) molybdenum, and (f) glassy carbon versus aluminum under a current of 1.78□10-2 mA cm-2 at room temperature.

Even more significant than the false discharge potential curve, the first charge resulted in a very pronounced potential plateau on all substrates with different onset points. The lowest plateau occurred with the nickel (Ni) substrate at approximately 1.0 V versus Al, which is clearly due to the electrochemical oxidation (corrosion) of Ni since it is much lower than the potential of chloride oxidation (chlorine generation). Furthermore, the electrochemical oxidation of Ni resulted in a distinct discharge plateau at 0.8 V versus Al in the subsequent discharge with a high apparent capacity and repeatability. Although Ni demonstrates some interesting electrochemical behavior, which may be worth further investigation, it is clear that Ni and Ni-containing alloys cannot be used as current collectors to study any active cathode materials. This statement is also true for Titanium (Ti), Platinum (Pt) and Tungsten (W), although these metals appear to have better resistance to electrochemical oxidation with higher charge plateaus. Nevertheless, the electrochemical oxidation of unstable substrates can lead to significant false discharge capacities from ~150 to ~400 mAh g^{-1} with a current of 1.78×10^{-2} mA cm^{-2} (under the assumption of 1 mg cm^{-2} loading of material of interest).

The most stable substrates among those tested are Mo and GC, which displayed plateaus above 2.4 V versus Al with onset potentials at 1.8 and 2.0 V, respectively. The 2.4 V plateau is due to the chlorine generation of **Reaction 1**, and it is the upper limit of the stable window of the deep eutectic chloroaluminate electrolytes.

$$4AlCl_4^- - 2e^- \rightarrow 2Al_2Cl_7^- + Cl_2 \quad (1)$$

It is also worth noting that the chlorine generation reaction does not induce any noticeable artificial discharge reactions on either Mo or GC surfaces. This indicates that Mo and GC can be cathodically stable even in the presence of chlorine. Therefore, one can conclude that Mo and GC are suitable current collectors to study cathode materials. Moreover, to avoid any potential interference, the best practice would be to keep the upper cutoff potential well below the 2.4 V limit versus Al. As the next section demonstrates, high surface area of the cathode structure may promote side reactions even at potentials lower than 2.4 V versus Al. In addition to Mo and GC, titanium nitride and chromium nitride were also reported to be stable in deep eutectic chloroaluminate electrolytes.[12] In that same study, the authors also reported W to be more anodically stable than Mo and GC, a result inconsistent with that of our study. This finding indicates that the stability of the current collector is quite sensitive to experimental conditions, although Mo, GC, or W current collectors appear to be the better choices regardless. We suggest investigators to always test "blank" electrodes (bare current collectors) as a reference, while avoiding contact between the electrolyte and the usual suspects such as stainless steel, Ni, Ti, Pt, etc.

Ambiguities Concerning the Carbon Cathode Materials: The most promising cathodes for rechargeable Al batteries are graphite or graphene-based materials, which have been under intensive investigations motivated by Lin et al.'s work reporting $AlCl_4^-$ reversibly intercalating into the interlayers of graphitic carbons with high voltage, good capacity, excellent C rate and cycle stability.[4] However, it is our intention to raise the awareness of certain potential points of contention regarding carbon cathode materials. As demonstrated

in the current collector study, chlorine generation occurs at approximately 2.4 V versus Al. Since the current used to determine the chlorine generation was fairly low at 1.78×10^{-2} mA cm^{-2}, no considerable concentration polarization would be generated. Therefore, 2.4 V versus Al should be close to the thermodynamic potential (with activation overpotential) of chlorine generation in the deep eutectic chloroaluminate electrolytes. On the other hand, the charge-cutoff-potential in most of the publications on carbon cathode materials is higher than or very close to 2.4 V versus Al. Thus, the possible generation of chlorine during the charging process on carbon cathodes is a legitimate concern.

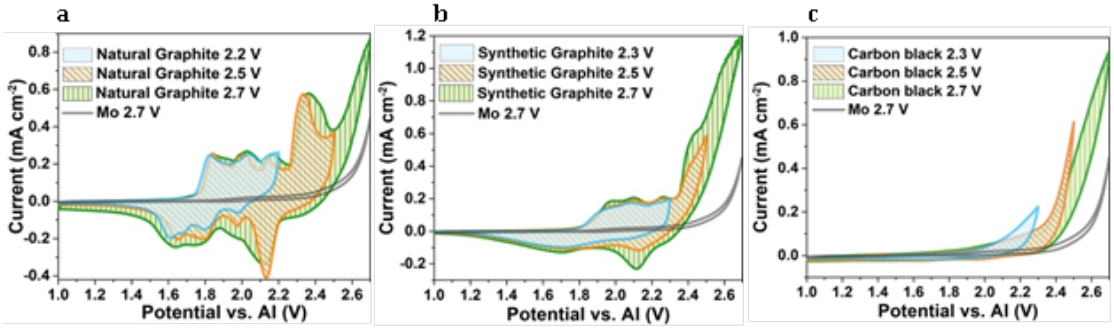

Figure 61. CV scans of various carbon materials including (a) natural graphite, (b) synthetic graphite (carbon paper) and (c) high surface area amorphous carbon nanoparticles versus Al under scan rate of 0.2 mV s-1 at room temperature.

Figure 61a displays the CV scan of natural graphite (3.5 mg cm^{-2} loading) versus Al. Three different anodic potential limits including 2.2, 2.5, and 2.7 V versus Al were selected to illustrate the evolution of the redox reactions of natural graphite. The graphite was coated on a Mo current collector, so the CV scan of the bare Mo current collector is also shown in the plot for reference. Three pairs of reversible redox peaks appear within the CV window between 1.0 and 2.2 V versus Al, and one more pair of reversible peaks with high peak

current appears when the window is extended to 2.5 V. These peaks were assigned to different stages of $AlCl_4^-$ intercalation into graphite in the literature. However, disagreement exists concerning the specific stage numbers obtained from X-ray diffraction and Raman spectroscopic characterizations.[13-16] When the anodic scan is extended to 2.7 V versus Al, a high current oxidation peak appears but without a reversible reduction peak. This peak clearly coincides with the chlorine generation peak indicated by the scan curve on the bare Mo current collector. The CV scans on synthetic graphite with 7.0 mg cm^{-2} loading (**Figure 61b**) demonstrate the same behavior but with less defined peaks. It is worth noting that the synthetic carbon we used was carbon paper, which is a common current collector used in studies of Al cathode materials. **Figure 61c** shows the CV scans on amorphous carbon (carbon black) (1.8 mg cm^{-2} loading) with a high surface area of 1100 m^2 g^{-1}. It is interesting to see that amorphous carbon, lacking periodic graphitic structure, hardly shows reversible redox peaks. However, it indeed shows pronounced and irreversible oxidation peaks. This observation has two indications: that it is possible that some portion of the apparently reversible anodic peaks (charging process) in natural graphite and synthetic graphite is irreversible, and that high surface area may promote this irreversible oxidation mechanism(s), which may be universally true for all high surface area materials.

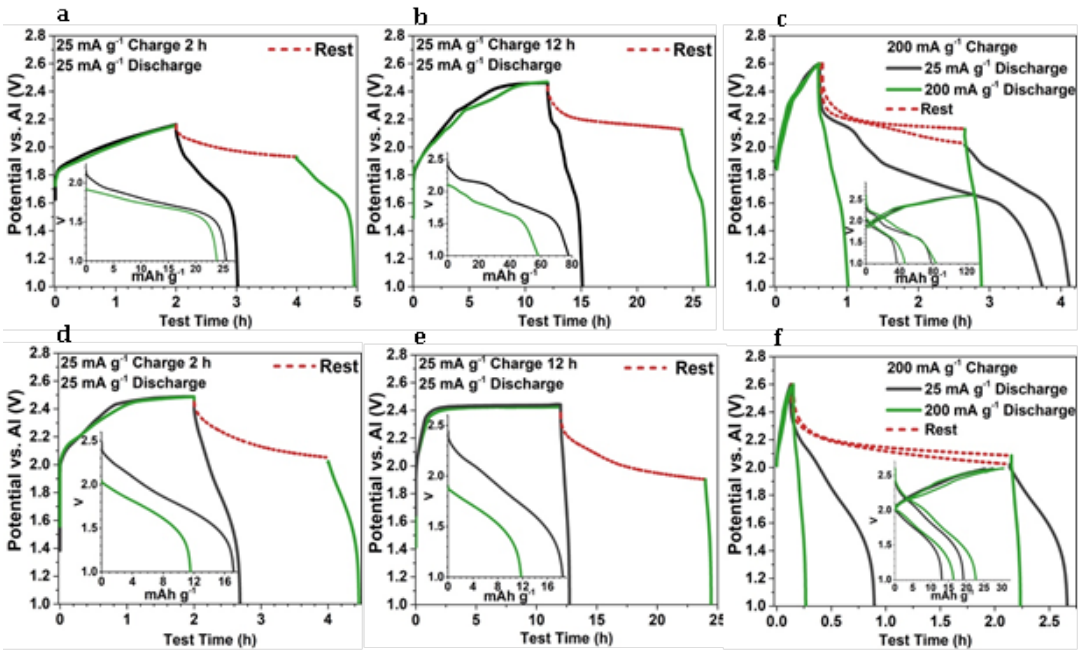

Figure 62. Different galvanostatic charge and discharge profiles (first cycle) of natural graphite (a, b, c) and synthetic graphite (d, e, f) at room temperature. The insets display the discharge capacities.

The complexity of the electrochemical processes on carbon is further illustrated in the galvanostatic charge-discharge experiments. **Figure 62a** shows the first charge-discharge cycle of natural graphite. It is worth mentioning that one of the proclaimed merits of carbon cathodes is their capability of extremely fast charging and discharging with very high specific current. However, it is necessary to utilize a low current to study intrinsic electrochemical properties to avoid the concentration polarization imposed by high currents. Furthermore, utilizing low currents does not alter the reaction mechanisms. For these reasons, a relatively low (compared to the values reported in the literature) specific current of 25 mA g^{-1} was used. As shown in Figure 4a, the natural graphite cathode was charged for 2 hours to reach a charge capacity of 50 mAh g^{-1}, which is consistent with the

typical discharge capacity reported for natural graphite cathodes. The potential of the cathode was noted to have nearly reached 2.2 V versus Al after 2-hour charging. However, the immediate discharge with the same specific current demonstrated a discharge capacity of only 25 mAh g^{-1}, a nearly 50% irreversibility. In another experiment, the cathode was allowed to rest for two hours after the same charging process, and the following discharge demonstrated a capacity of 24 mAh g^{-1}. This is clear evidence supporting the CV data in Figure 3: some reaction(s) in the charging process is irreversible, even at a potential well below that of chlorine generation. As shown in **Figure 62b**, we charged the natural graphite for 12 hours under 25 mA g^{-1}, and it reached the chlorine generation potential plateau at 2.45 V versus Al. The immediate discharge under 25 mA g^{-1} demonstrated a capacity of 78 mAh g^{-1}, significantly lower than the charge capacity. In a separate experiment, the same charging process was followed by a 12-hour rest before discharge, upon which the discharge capacity decreased to 58 mAh g^{-1} along with the disappearance of the higher discharge plateau (inset of **Figure 62b**). This observation raises another key problem of the carbon cathode, which is severe self-discharge. To date there has been only one study to our best knowledge showing self-discharge behavior of Al batteries with graphite electrodes, but without mechanism investigation.[17] In fact, the plateau of chlorine generation can be overcome (or more accurately, masked) by use of a higher specific charge current due to concentration polarization. As shown in **Figure 62c**, the natural graphite cathode charged under 200 mA g^{-1} could reach 2.6 V versus Al (the set upper cutoff potential) without showing the plateau. The charge capacity is approximately 130 mAh g^{-1} (inset of **Figure 62c**). However, the discharge, under either 25 mA g^{-1} or 200 mA

g^{-1} , still only delivers a capacity of 80 mAh g^{-1}, a nearly 40% irreversibility. After a 2-hour rest, the discharge capacity decreased to approximately 40 mAh g^{-1}, confirming the severe self-discharge behavior. The synthetic graphite cathode in **Figures 62d-f** basically demonstrated identical behaviors. An additional abnormal observation is that fast discharge demonstrates higher capacity than slower discharge does, which can also be seen in the literature.[4] One possible explanation (and perhaps the only rational explanation) is the kinetic competition between the chemical self-discharge reaction(s) and the electrochemical discharge reaction: if the electrochemical discharge is not under mass transfer limitation and intrinsically fast, enforcing a high discharge current can indeed "win" over a kinetically slower chemical self-discharge. This could be the reason that the irreversibility of carbon cathodes has not been widely noted in the literature, since many reports emphasize a high charge-discharge rate.

Hopefully, we have made a clear case that what really happens at carbon material cathodes is more complicated than the simple interaction with $AlCl_4^-$. We speculate that the charging of graphitic carbon cathodes in the deep eutectic chloroaluminate electrolytes is a process consisting of a number of simultaneous and intertwined mechanisms. The electrochemical processes on carbon cathodes must be thoroughly scrutinized to prove the feasibility of this Al-carbon rechargeable battery technology. It is difficult to expect a practical battery while risking chlorine evolution during operation. There is little doubt that graphitic carbons indeed host intercalated species as demonstrated by X-ray diffraction and Raman characterizations, but whether the intercalated species is only $AlCl_4^-$ needs to be examined. An interesting question which has not been answered is why an intercalation chemistry

with a fairly large intercalating species ($AlCl_4^-$), whose rate capability is typically limited by the solid-state diffusion of the intercalating species in the host structure, allows extremely fast charge and discharge. Actually, in the early studies of using graphite as the cathode material for recharge Al batteries (represented by the study by Gifford and Palmisano[18]), chlorine was proposed to be the intercalated species in graphite. Chlorine intercalation into graphite from chloride-containing electrolytes was also recently reported by Yang et al.[19] Considering the chlorine generation potential in close proximity of the charging potential, the irreversible charge capacity, and the severe self-discharge behavior, it is a reasonable hypothesis that chlorine is involved in the intercalation and may not be stably hosted.

Other Issues in Al Battery Research: In addition to the above concerns about carbon cathode materials, there are also issues with other types of cathode materials, specifically transition metal oxides and sulfides. The rationale for the selection of metal oxide and sulfide cathode materials in current literature is mainly based on the understanding of how these materials behave as cathodes for Li-ion batteries. However, one must recognize that Al-ion electrochemistry is drastically different from Li-ion electrochemistry. The Coulombic interaction of Al-ion is tremendously stronger than that of Li-ion due to its trivalency, which can make the intercalation of Al-ions in metal oxides and sulfides extremely difficult if not impossible.[20] To date, the only material to have been unambiguously proven as a host structure for reversible Al-ion intercalation is Chevrel phase molybdenum sulfide (Mo_6S_8).[21-23] However, the Al-ion intercalation in Mo_6S_8 is attributed to the very unique crystal structure of the Chevrel phase molybdenum

chalcogenides, which could be a singular case for Al-ion intercalation. To demonstrate Al-ion intercalation, unambiguous crystallographic data would be the most convincing, but they are generally absent in current literature. Spectroscopic techniques identifying change of oxidation state of the transition metals in the cathode materials cannot be used as the sole means to claim intercalation chemistry. For instance, X-ray photoelectron spectroscopy (XPS) is one of the widely used methods to characterize the metal oxides and sulfide cathodes before and after electrochemical reaction with Al-ion. However, XPS is essentially a surface chemical analysis method for the identification of the oxidation states of the surface elements only. Even if change of oxidation state was detected, XPS data could not distinguish the origin between intercalation and simple redox. Furthermore, the surface chemistry may not represent the bulk properties. In fact, if electrochemical reactions indeed occurred in the metal oxides or sulfides (more likely in sulfides due to the more polarizable sulfide anion) in Al batteries, the mechanism would more likely be simple redox reactions of the transition metals. Another problem with transition metal oxide and sulfide cathodes is their chemical compatibility with the deep eutectic chloroaluminate electrolytes, a problem that has been completely overlooked in current literature. One of our recent studies (currently under review) clearly indicates that vanadium pentoxide (V_2O_5), a widely investigated potential cathode material for rechargeable Al batteries, dissolves in and reacts with deep eutectic chloroaluminate electrolytes at different Lewis acidities to generate new vanadium compounds. Iron sulfide (FeS_2) was also reported to be soluble in the chloroaluminate electrolytes,[24] but unfortunately the species resulting from the dissolution were not identified. It is reasonable to speculate that V_2O_5 and FeS_2 may

not be the only two metal oxides/sulfides that can dissolve in deep eutectic electrolytes. Therefore, testing the compatibility between potential cathode materials and electrolytes should be mandated practice in these investigations.

Summary and Outlook: Rechargeable Al batteries are both scientifically intriguing and challenging. At the research's current infancy stage, the fundamental mechanisms of Al electrochemistry, not performance, should be the emphasis of the research community. For experimental investigations, rigorous experimental setup, execution, and data interpretation without prejudgments are very important. False positive results can be generated from unsuitable current collectors or impure electrolytes, as demonstrated in this work. The electrochemical properties of cathode materials such as graphitic carbons, transition metal oxides, and sulfides are yet another area demanding thorough and unbiased scrutiny.

It is also clear that most of the problems and discrepancies in current Al battery research originate from the use of complex deep eutectic chloroaluminate electrolytes. They are fundamentally different from the known Li and Mg electrolytes with either salts with weakly coordinating anions or organomagnesium complex. Their chemical and electrochemical properties must be thoroughly investigated. The chloroaluminate electrolytes are also expensive and having the risk of chlorine generation, thus it could be challenging to use these electrolytes in real devices. Therefore, new Al electrolytes, which are inexpensive, chemically and electrochemically stable, and active-chloride-free, should be the priority of the future rechargeable Al battery research. As the only rational choice

for anode, Al should be investigated with the focus on the deposition-stripping efficiency and the Al/electrolyte interface phenomenon. On the cathode side, transition metal oxides and sulfides may be scientifically interesting (to investigate the reaction feasibility and mechanisms), but suffering from the combination of low capacity and low reaction potential. Cathode materials could have real application impact are conversion-type materials such as sulfur. From the practical point of view, rechargeable Al batteries cannot and should not compete with Li-ion batteries for the high-end markets such as passenger electric vehicles and personal electronics. Therefore, investigation on cell design and operation conditions for specific novel applications could be a new direction for rechargeable Al batteries.

References

1 Elia, G. A.; Marquardt, K.; Hoeppner, K.; Fantini, S.; Lin, R. Y.; Knipping, E.; Peters, W.; Drillet, J. F.; Passerini, S.; Hahn, R., An Overview and Future Perspectives of Aluminum Batteries. *Adv. Mater.* **2016,** *28* (35), 7564-7579.

2 Wilkes, J. S.; Levisky, J. A.; Wilson, R. A.; Hussey, C. L., Dialkylimidazolium Chloroaluminate Melts - a New Class of Room-Temperature Ionic Liquids for Electrochemistry, Spectroscopy, and Synthesis. *Inorg. Chem.* **1982,** *21* (3), 1263-1264.

3 Lai, P. K.; Skyllas-Kazacos, M., Electrodeposition of Aluminum in Aluminum Chloride/1-Methyl-3-Ethylimidazolium Chloride. *J. Electroanal Chem.* **1988,** *248* (2), 431-440.

4 Lin, M. C.; Gong, M.; Lu, B. G.; Wu, Y. P.; Wang, D. Y.; Guan, M. Y.; Angell, M.; Chen, C. X.; Yang, J.; Hwang, B. J.; Dai, H. J., An ultrafast rechargeable aluminium-ion battery. *Nature* **2015,** *520* (7547), 325.

5 Sun, H. B.; Wang, W.; Yu, Z. J.; Yuan, Y.; Wang, S.; Jiao, S. Q., A new aluminium-ion battery with high voltage, high safety and low cost. *Chem. Commun.* **2015,** *51* (59), 11892-11895.

6 Reed, L. D.; Arteaga, A.; Menke, E. J., A Combined Experimental and

Computational Study of an Aluminum Triflate/Diglyme Electrolyte. *J. Phys. Chem. B* **2015,** *119* (39), 12677-12681.

7 Nakayama, Y.; Senda, Y.; Kawasaki, H.; Koshitani, N.; Hosoi, S.; Kudo, Y.; Morioka, H.; Nagamine, M., Sulfone-based electrolytes for aluminium rechargeable batteries. *Phys. Chem. Chem. Phys.* **2015,** *17* (8), 5758-5766.

8 Mandai, T.; Johansson, P., Haloaluminate-Free Cationic Aluminum Complexes: Structural Characterization and Physicochemical Properties. *J. Phys. Chem. C* **2016,** *120* (38), 21285-21292.

9 Chiku, M.; Matsumura, S.; Takeda, H.; Higuchi, E.; Inoue, H., Aluminum Bis(trifluoromethanesulfonyl)imide as a Chloride-Free Electrolyte for Rechargeable Aluminum Batteries. *J. Electrochem. Soc.* **2017,** *164* (9), A1841-A1844.

10 Reed, L. D.; Menke, E., The Roles of V2O5 and Stainless Steel in Rechargeable Al-Ion Batteries. *J. Electrochem. Soc.* **2013,** *160* (6), A915-A917.

11 Geng, L. X.; Scheifers, J. P.; Fu, C. Y.; Zhang, J.; Fokwa, B. P. T.; Guo, J. C., Titanium Sulfides as Intercalation-Type Cathode Materials for Rechargeable Aluminum Batteries. *Acs Appl. Mater. Inter.* **2017,** *9* (25), 21251-21257.

12 Wang, S. T.; Kravchyk, K. V.; Filippin, A. N.; Muller, U.; Tiwari, A. N.; Buecheler, S.; Bodnarchuk, M. I.; Kovalenko, M. V., Aluminum Chloride-Graphite Batteries with Flexible Current Collectors Prepared from Earth-Abundant Elements. *Adv. Sci.* **2018,** *5*, 1700712. DOI: 10.1002/advs.201700712.

13 Childress, A. S.; Parajuli, P.; Zhu, J. Y.; Podila, R.; Rao, A. M., A Raman spectroscopic study of graphene cathodes in high-performance aluminum ion batteries. *Nano Energy* **2017,** *39*, 69-76.

14 Wang, D. Y.; Wei, C. Y.; Lin, M. C.; Pan, C. J.; Chou, H. L.; Chen, H. A.; Gong, M.; Wu, Y. P.; Yuan, C. Z.; Angell, M.; Hsieh, Y. J.; Chen, Y. H.; Wen, C. Y.; Chen, C. W.; Hwang, B. J.; Chen, C. C.; Dai, H. J., Advanced rechargeable aluminium ion battery with a high-quality natural graphite cathode. *Nature Communication* **2017,** *8*:14283 DOI: 10.1038/ncomms14283.

15 Zhang, L. Y.; Chen, L.; Luo, H.; Zhou, X. F.; Liu, Z. P., Large-Sized Few-Layer Graphene Enables an Ultrafast and Long-Life Aluminum-Ion Battery. *Adv. Energy Mater.* **2017,** *7*, 1700034. DOI: 10.1002/aenm.201700034.

16 Pan, C. J.; Yuan, C. Z.; Zhu, G. Z.; Zhang, Q.; Huang, C. J.; Lin, M. C.; Angell, M.; Hwang, B. J.; Kaghazchi, P.; Dai, H. J., An operando X-ray diffraction study

of chloroaluminate anion-graphite intercalation in aluminum batteries. *P. Natl. Acad. Sci. USA* **2018,** *115* (22), 5670-5675.

17 Li, Z. Y.; Liu, J.; Niu, B. B.; Li, J. L.; Kang, F. Y., A Novel Graphite-Graphite Dual Ion Battery Using an AlCl3-[EMIm]Cl Liquid Electrolyte. *Small* **2018,** 1, 1800745. DOI: 10.1002/smll.201800745.

18 Gifford, P. R.; Palmisano, J. B., An Aluminum Chlorine Rechargeable Cell Employing a Room-Temperature Molten-Salt Electrolyte. *J. Electrochem. Soc.* **1988,** *135* (3), 650-654.

19 Yang, C. Y.; Chen, J.; Ji, X.; Pollard, T. P.; Lu, X. J.; Sun, C. J.; Hou, S.; Liu, Q.; Liu, C. M.; Qing, T. T.; Wang, Y. Q.; Borodin, O.; Ren, Y.; Xu, K.; Wang, C. S., Aqueous Li-ion battery enabled by halogen conversion-intercalation chemistry in graphite. *Nature* **2019,** *569* (7755), 245.

20 Rong, Z. Q.; Malik, R.; Canepa, P.; Gautam, G. S.; Liu, M.; Jain, A.; Persson, K.; Ceder, G., Materials Design Rules for Multivalent Ion Mobility in Intercalation Structures. *Chem. Mater.* **2015,** *27* (17), 6016-6021.

21 Geng, L. X.; Lv, G. C.; Xing, X. B.; Guo, J. C., Reversible Electrochemical Intercalation of Aluminum in Mo6S8. *Chem. Mater.* **2015,** *27* (14), 4926-4929.

22 Lee, B.; Lee, H. R.; Yim, T.; Kim, J. H.; Lee, J. G.; Chung, K. Y.; Cho, B. W.; Oh, S. H., Investigation on the Structural Evolutions during the Insertion of Aluminum Ions into Mo6S8 Chevrel Phase. *J. Electrochem. Soc.* **2016,** *163* (6), A1070-A1076.

23 Geng, L. X.; Scheifers, J. P.; Zhang, J.; Bozhilov, K. N.; Fokwa, B. P. T.; Guo, J. C., Crystal Structure Transformation in Chevrel Phase Mo6S8 Induced by Aluminum Intercalation. *Chem. Mater.* **2018,** *30* (23), 8420-8425.

24 Mori, T.; Orikasa, Y.; Nakanishi, K.; Chen, K. Z.; Hattori, M.; Ohta, T.; Uchimoto, Y., Discharge/charge reaction mechanisms of FeS2 cathode material for aluminum rechargeable batteries at 55 degrees C. *J. Power Sources* **2016,** *313*, 9-14.

4.4 Connection and Difference between Li Metal and Multivalent Metal Batteries

Beyond lithium-ion batteries, rechargeable metal battery systems have received increasing attention as energy storage technologies1,2. Although battery systems with different metal

anodes are at different stages of development and face different challenges, the comparison to lithium metal anodes, especially regarding morphological instabilities, could cast light on the determining parameters of dendrite formation or mossy structures.

Thermodynamically, electrochemical deposition is closely related to the adsorption/desorption energies of ions at surfaces[3]. Surfaces with larger areal packing densities tend to exhibit lower surface energies[3]. Magnesium metal batteries are often considered dendrite-free or less prone to dendritic growth[4]. According to DFT studies, the free energy difference between high dimensional and low dimensional phases are higher for Mg than for Li resulting in preferably 2D and 3D growth of Mg compared to one-dimensional growth of Li[5,6]. However, research has proven Mg dendrite growth in various electrolytes[7,8]. As mentioned above, in transport limited scenarios, dendrite formation is anticipated independent of the electrodeposited metal. Thus, it is important to report the applied current densities and to estimate whether the system is transport limited when reporting dendritic growth. Nevertheless, the surface properties of Mg crystals can have a huge impact in mitigating needle-like structures when the system is not transport limited.

One-dimensional whiskers are known to occur for electroplated tin, cadmium, and zinc[9–10]. These whiskers are single crystals and grow from the base[11]. However, the situation there is different than for electroplated lithium. High aspect ratio whiskers are reported to grow to considerable lengths when storing substrates with the electroplated metal for long periods.

Whiskers are also seen in the electrodeposition of copper at room temperature, which has a very high melting point. There, the whisker growth is explained by suspended particles which are deposited on the copper[12]. The particles lead to points where the exchange current density is much higher than on the passivated copper, leading to tip-growing whiskers. The one-dimensional structure is maintained as the lateral surface of the whisker gets passivated. No whiskers were formed if the electrolyte was filtered through an ultrafine filter. Lithium whiskers, however, are observed to be root-growing.

Sodium metal anodes are comparable to lithium metal anodes, as they also report needle-like and mossy growth for non-transport limited current regimes[13–15]. Like lithium, mossy sodium appears to grow from the root[16]. As research of lithium metal anodes is ahead of sodium metal anodes, there are no direct new insights from sodium metal anode research. Nevertheless, relating the similarities and differences of lithium and sodium to the observed morphologies can help to infer important properties of mossy growth. Sodium has an even lower melting point than lithium and is mechanically softer. Like lithium, sodium metal anodes are covered by an SEI, which in the case of sodium is even more unstable. In the case of sodium, the morphological instabilities are even more severe, and the fragile structures can easily detach from the anode creating dead sodium. Similar to lithium, mossy sodium is reported to start with needle-like structures. But different to lithium, the needle-like structures seem to form no or fewer kinks[16]. Lithium metal anodes not only benefit from the comparison of other metal anodes but also from their interfaces with the electrolyte. It could always be a good trial to adopt other metal anode technologies to Li metal.

References

1 Liang, Y., Dong, H., Aurbach, D. & Yao, Y. Current status and future directions of multivalent metal-ion batteries. *Nat. Energy* **5**, 646–656 (2020) doi:10.1038/s41560-020-0655-0.

2 Delmas, C. Sodium and Sodium-Ion Batteries: 50 Years of Research. *Adv. Energy Mater.* **8**, (2018) doi:10.1002/aenm.201703137.

3 Nagy, K. S., Kazemiabnavi, S., Thornton, K. & Siegel, D. J. Thermodynamic Overpotentials and Nucleation Rates for Electrodeposition on Metal Anodes. *ACS Appl. Mater. Interfaces* **11**, 7954–7964 (2019) doi:10.1021/acsami.8b19787.

4 Muldoon, J. *et al.* Electrolyte roadblocks to a magnesium rechargeable battery. *Energy Environ. Sci.* **5**, 5941 (2012) doi:10.1039/c2ee03029b.

5 Ling, C., Banerjee, D. & Matsui, M. Study of the electrochemical deposition of Mg in the atomic level: Why it prefers the non-dendritic morphology. *Electrochim. Acta* **76**, 270–274 (2012) doi:10.1016/j.electacta.2012.05.001.

6 Jäckle, M. & Groß, A. Microscopic properties of lithium, sodium, and magnesium battery anode materials related to possible dendrite growth. *J. Chem. Phys.* **141**, 174710 (2014) doi:10.1063/1.4901055.

7 Ding, M. S., Diemant, T., Behm, R. J., Passerini, S. & Giffin, G. A. Dendrite Growth in Mg Metal Cells Containing Mg(TFSI) 2 /Glyme Electrolytes . *J. Electrochem. Soc.* **165**, A1983–A1990 (2018) doi:10.1149/2.1471809jes.

8 Davidson, R. *et al.* Formation of Magnesium Dendrites during Electrodeposition. *ACS Energy Lett.* **4**, 375–376 (2019) doi:10.1021/acsenergylett.8b02470.

9 Ashworth, M. A. *et al.* The effect of electroplating parameters and substrate material on tin whisker formation. *Microelectron. Reliab.* **55**, 180–191 (2015) doi:10.1016/j.microrel.2014.10.005.

10 Lindborg, U. Observations on the growth of whisker crystals from zinc electroplate. *Metall. Trans. A* **6**, 1581–1586 (1975) doi:10.1007/BF02641971.

11 Majumdar, B. S., Dutta, I., Bhassyvasantha, S. & Das Mahapatra, S. Recent Advances in Mitigation of Whiskers from Electroplated Tin. *Jom* **72**, 906–917 (2020) doi:10.1007/s11837-019-03933-7.

12 Kittaka, S. & Kishi, K. Growth of Copper Whiskers from Cupric Oxide. *Jpn. J. Appl. Phys.* **4**, 661–666 (1965) doi:10.1143/jjap.4.661.

13 Rodriguez, R. *et al.* In Situ Optical Imaging of Sodium Electrodeposition: Effects of Fluoroethylene Carbonate. *ACS Energy Lett.* **2**, 2051–2057 (2017) doi:10.1021/acsenergylett.7b00500.

14 Wei, S. *et al.* Highly Stable Sodium Batteries Enabled by Functional Ionic Polymer Membranes. *Adv. Mater.* **29**, 1605512 (2017) doi:10.1002/adma.201605512.

15 Yui, Y., Hayashi, M. & Nakamura, J. In situ Microscopic Observation of Sodium Deposition/Dissolution on Sodium Electrode. *Sci. Rep.* **6**, 22406 (2016) doi:10.1038/srep22406.

16 Schmitt, T., Arlt, T., Manke, I., Latz, A. & Horstmann, B. Zinc electrode shape-change in secondary air batteries: A 2D modeling approach. *J. Power Sources* **432**, 119–132 (2019) doi:10.1016/j.jpowsour.2019.126649.

Chapter 5: Summary and Future Directions

Just as the reason why Li-ion batteries received the Nobel Prize in Chemistry in 2019, the successful commercialization of lithium-ion batteries depends very much on their safety during operation under normal and abusive conditions. At the cell level, high-voltage cathode materials that are initially in a discharged state based on intercalation chemistry and material physics are developed. Carbonaceous anodes that can store Li^+, instead of metallic lithium metal, were used for the battery. At the same time, coordination chemistry, electrolyte, and interface chemistry were developed to help find a non-aqueous electrolyte that has a wide operation window for both high-voltage cathode and forming stable SEI on the anode.

To meet the application of long cycle, high energy density, and/or extreme conditions, new cell components, and a stabler interface must be developed. Apart from fundamental studies mentioned in the capacity fade part, the library of current electrode materials, solvents, salts, and additives is very limited. The further improvement of Li batteries requires a fundamental understanding of electrochemical processes of different/new cell chemistries, working/failure mechanisms of active materials (electrolyte and electrode), and interface and interphase of electrode/electrolyte. By combining the development of mathematical electrochemical models (kinetics, thermodynamics, and mass transfer) and characterization technologies (electrochemical and beyond), hopefully, we can summarize the designing rules for each cell component, for their combinations, and for each specific application not only limited to pre-lithiation.